

DEGRADATION OF EMERGING CONTAMINANTS BY Fe- and Mn- BASED OXIDATION
METHODS IN AQUEOUS SOLUTION

A Dissertation

Presented to the Faculty of the Graduate School
of Cornell University

In Partial Fulfillment of the Requirements for the Degree of
Doctor of Philosophy

by

Xiao Xiao

August 2012

© 2012 Xiao Xiao

DEGRADATION OF EMERGING CONTAMINANTS BY Fe- and Mn- BASED OXIDATION METHODS IN AQUEOUS SOLUTION

Xiao Xiao, Ph. D.

Cornell University 2012

Presence of pharmaceuticals and endocrine disrupting compounds (EDCs) in the environment is of growing concern due to their potential ecological impacts and constant release. Conventional treatment plants are inefficient in removing such compounds, driving the need for innovative treatment methods. Oxidation processes are attractive options because structure alterations by oxidation can lead to reduced biological activity, increased biodegradability and mineralization.

Three oxidation treatment methods, Anodic Fenton treatment (AFT), cryptomelane-type manganese oxides and biogenic manganese oxides were evaluated using pharmaceutical and EDCs probes. Ciprofloxacin (CIP), a widely used fluoroquinolone, was degraded in the AFT system. Fast removal was observed in minutes. The degradation kinetics were found to deviate from the classical AFT model. This change in kinetic pattern is because speciation distribution changes as the solution pH self-optimizes to acidic conditions, and reaction affinity of the CIP species toward the hydroxyl radical is protonation dependent. Modification was made to the AFT model to account for the pH induced change in reaction affinity. Process condition was optimized at pH 3.2, giving a Fenton reagent delivery ratio of $[H_2O_2]:[Fe^{2+}]$ between 10 to 15. Analysis on structures and evolution pattern of degradation products indicated elimination of the antibiotic activity of the solution after AFT treatment. Cryptomelane is a framework type manganese oxide whose synthetic counterpart has gained wide industry application. Oxidative

degradation of CIP by synthetic cryptomelane (OMS-2) was not successful. Doping V or Mo into the framework of OMS-2 increased its oxidative reactivity significantly. 9% Mo doping was found to give the best performance. Structure characterization results indicated that the improvement was mainly due to increased surface area upon doping. Response surface methodology was applied to find the optimal treatment condition: pH 3 and [Oxidant]:[Substrate] molar ratio ≥ 50 . Analysis of degradation products suggested that the oxidation mainly takes place at the piperazine ring of CIP. Lower biological activity of the products is expected since the piperazine ring is an important substituent on the quinolone core structure that affects antibiotic potency. Biogenic manganese oxide (BioMnO_x) is formed by *Leptothrix discophora* SS-1. Successful removal of CIP and BPA by BioMnO_x can be achieved, but the reaction rates were slower by BioMnO_x, compared to that by synthetic MnO₂. This is probably due to a larger particle size, smaller surface area and lower average oxidation states of BioMnO_x. The bleaching procedure improved the reactivity of BioMnO_x significantly. Generally, lower solution pH is favorable for the oxidation reaction. Presence of cations can slow down the oxidation process even more by competing for the reactive sites. Humic acid can affect the oxidative degradation via two countering effects: blocking of surface reactive sites which reduces reactivity and binding inhibitory MnII ion released during the reaction which accelerates the reaction. The BioMnO_x system yielded fewer degradation products than the synthetic MnO₂ systems as well as different product distributions. The mechanism for the preference of degradation pathways remains unclear. The applicability of BioMnO_x as a water treatment technology is still questionable and requires more evaluation.

BIOGRAPHICAL SKETCH

Xiao Xiao was born in an ancient town with thousands of years of history, Dingzhou, in Hebei province, China. Although Dingzhou is only a mid-sized town, it is also a busy traffic hub in that region. Thus she was able to enjoy the scenic country views as well as the convenience of city life during her childhood and teen years. Being raised up in such a rural historical place, she has fostered love for the nature as well as Chinese literature and history.

In 2003, she was admitted to Nankai University, Tianjin, a school with top Chemistry programs in China. She chose to study environmental science with a concentration in chemistry because chemical industry was blamed for creating environmental problems by the media and public. She was motivated to learn chemical approaches to solve environmental problems and understand environmental processes. With her projects on environmental fate of contaminants, she felt an urgent need to seek higher education and decided to apply for graduate programs.

Not long after the Spring Festival of 2007, she received an exciting offer letter from Prof. Lemley. This is the most meaningful moment in her life by far. In addition to the opportunity of career development, it also made her reunion with her boyfriend, now her husband, possible. Like those Chinese Cornelians since 1900s, she had wonderful years in Cornell. In addition to all the professional training, she also matured and learned to be a good and supporting wife.

In 2012 summer, she will complete her study and become the first Ph.D in her family. With all the assets she gained from Cornell, she will continue her journey.

献给志根,家人和陪我一起成长的朋友

To my beloved parents, Zhenfu Xiao and Yajun Zeng, and my husband, Zhigen Zhao

ACKNOWLEDGMENTS

This PhD thesis would not have been possible without the support of many people. First of all, I'd like to express my deepest gratitude to my supervisor, Prof. Ann Lemley, who was abundantly helpful and offered invaluable assistance, support and guidance for the research and the writing of this thesis, and also provided financial support for my living expenses in the USA.

Deepest gratitude is also due to my committee members and co-worker, Prof. Murray McBride, Prof. Anthony Hay, Prof. Leonard Lion and Prof. Chao Xu, without whose knowledge, instructions, assistance and collaboration, this thesis would not have been completed.

I am indebted to Dr. Xia (Sam) Zeng and Dr. Tewari for their continuous support on the equipments. I also thank support people from Cornell's CCMR, John Grazel, Malcolm Thomas, Dr. Umbach, Jonathan Shu, Dr. Weathers, for their instructions and help on the instruments.

I am grateful to Dr. Xia (Sam) Zeng, Dr. Peng Ye, Dr. Shengpeng Sun and Katherine Neafsey Engler in our lab, for their invaluable discussions and support on my research. I also want to thank all the faculties and students in the Environmental Toxicology program and Fiber Science who provided suggestions on my research during my seminar presentations. I also thank the College of Human Ecology and Department of Fiber Science and Apparel Design for part of the financial support for this thesis research.

I am really grateful to my family, especially to my beloved parents for their continuous support and encouragement. At last, I want to express my special thanks to my husband, Zhigen. I would not have completed my Ph.D thesis without his endless love, understanding, encouragement and support.

TABLE OF CONTENTS

BIOGRAPHIC SKETCH	iii
DEDICATION	iv
ACKNOWLEDGMENTS	v
TABLE OF CONTENTS	vi
LIST OF FIGURES	viii
LIST OF TABLES AND SCHEMES	xii
LIST OF ABBREVIATIONS	xiii
CHAPTER 1: INTRODUCTION	1
CHAPTER 2: SPECIES DEPENDENT DEGRADATION OF CIPROFLOXACIN IN MEMBRANE ANODIC FENTON SYSTEM	19
CHAPTER 3: DEGRADATION OF CIPROFLOXACIN BY CRYPTOMELANE- TYPE MANGANESE (III/IV) OXIDES	46
CHAPTER 4: CHARACTERIZATION OF Mn(II) OXIDATION PROCESS BY <i>LEPTOTHRIX DISCOPHORA SS-1</i> MANGANESE OXIDIZING FACTOR	80
CHAPTER 5: DEGRADATION OF CIPROFLOXACIN AND BISPHENOL A BY BIOGENIC MANGANESE OXIDES	100
CHAPTER 6: CONCLUSIONS AND RECOMMENDATIONS FOR FUTURE RESEARCH	130
APPENDIX A. REPRESENTATIVE CHROMATOGRAM OF CIP DEGRADATION PRODUCTS	134
APPENDIX B. Mn 3S SPECTRA OF OMS-2	135
APPENDIX C. IR AND RAMAN SPECTRA OF V ₂ O ₅ AND MoO ₃	136
APPENDIX D. RESPONSE SURFACE OF DEGRADATION EFFICIENCY	138

AS A FUNCTION OF PROCESS PARAMETERS

APPENDIX E. COMPARISON OF TURBIDITY AND LBB ASSAY

139

FOR MnO_x QUANTIFICATION

LIST OF FIGURES

Figure 1.1	Scheme of membrane Anodic Fenton Treatment System	5
Figure 1.2	Two types of manganese oxide structures	6
Figure 2.1	Speciation of CIP, $pK_{a1} = 6.1$, $pK_{a2} = 8.8$	21
Figure 2.2	Degradation of CIP in AFT system at $pH_0 = 3.2$ and 6.2-6.8	26
Figure 2.3	Structure of Reference compounds: 1-Phenyl Piperazine, 1,6-dimethyl-4-oxo-1,4 dihydroquinoline-3-carboxylic acid and ciprofloxacin methyl ester	27
Figure 2.4	Degradation of reference compounds in AFT system at $pH = 3.2$ and $pH = 6.2-6.8$	28
Figure 2.5	Calculated potential energy surface profiles for reaction between deprotonated and protonated CIP with hydroxyl radical by Gaussian 03 (B3LYP/6-31G)	30
Figure 2.6	(A) Degradation of CIP and CIP-Metal complex in AFT system (B) pH profiles during degradation of ciprofloxacin and ciprofloxacin-metal complex in AFT system	32
Figure 2.7	(A) pH profiles during Ciprofloxacin degradation in AFT system (B) Deprotonated Ciprofloxacin percentage during AFT process	34
Figure 2.8	(A) Degradation of CIP with different current delivery rates at $pH 6.2-6.8$ (B) Comparison of AFT model and AFT' model by fitting degradation data at current delivery = 0.04A	36
Figure 2.9	Degradation of Ciprofloxacin under different current delivery rates at $pH = 3.2$	37

LIST OF FIGURES (CONTD)

Figure 2.10	Degradation of Ciprofloxacin at current delivery = 0.04 A with different $[H_2O_2]/[Fe^{2+}]$ ratios, at pH=3.2	37
Figure 2.11	Proposed degradation pathways of CIP in the AFT system	40
Figure 2.12	Evolution of CIP degradation products. (A) Initial pH = 6.2-6.8; (B) Initial pH = 3.2	41
Figure 3.1	Crystal structure of cryptomelane	48
Figure 3.2	XRD patterns of regular and doped OMS-2	54
Figure 3.3	SEM images of regular and doped OMS-2	55
Figure 3.4	Representative energy dispersive X-ray spectra of doped OMS-2	56
Figure 3.5	A IR and B Raman spectra of regular and doped OMS-2	59
Figure 3.6	A Degradation of CIP by different doped OMS-2; B Degradation of CIP by Mo/OMS-2 with different Mo doping amount	61
Figure 3.7	Predicted values of CIP removal efficiency versus experimental values	62
Figure 3.8	A Response surface of degradation efficiency as a function of pH and 9% Mo/OMS-2; B Response surface of degradation efficiency as a function of C_{cip} and 9% Mo/OMS-2; C Contour plot of degradation efficiency as a function of C_{cip} and 9% Mo/OMS-2.	65
Figure 3.9	Degradation of CIP by 9% Mo/OMS-2 and Mn^{II} release into solution, A pH = 3; B pH = 4 and 5.5.	67
Figure 3.10	Effects of Pre-added Mn^{II} ion on CIP degradation.	68
Figure 3.11	Structures of CIP and reference compound QA	71

LIST OF FIGURES (CONTD)

Figure 3.12	Evolution of CIP degradation by-products by 9% Mo/OMS-2	71
Figure 3.13	Proposed degradation products and pathways of CIP by 9% Mo/OMS-2	73
Figure 4.1	Cell growth and MOF activity of <i>L. Discophora</i> SS-1	86
Figure 4.2	Effect of Mn(II) on MOF activity	88
Figure 4.3	Effect of pyrophosphate on Mn(II) oxidation, measured by the LBB assay	91
Figure 4.4	Effect of kanamycin and tetracycline on Mn(II) oxidation	92
Figure 4.5	Transformation of tetracycline by biogenic manganese oxides, [BioMnO _x] = 200 μM, Tetracycline = 50 μM, pH = 7.3	93
Figure 5.1	XRD analysis of synthetic and biogenic Mn(III/IV) Oxides	107
Figure 5.2	SEM micrographs of synthetic and biogenic Mn(III/IV) Oxides, (a) synthetic MnO ₂ ; (b) BioMnO _x (c) BioBleMnO _x .	108
Figure 5.3	Thermal gravimetric analyses of synthetic and biogenic Mn(III/IV) oxides	109
Figure 5.4	Degradation of CIP and BPA at pH 5 at different BioMnO _x dosage: (A) [CIP] = 5 μM, [BioMnO _x] = 200, 400, 600 μM; (B) [BPA] = 4.4 μM, [BioMnO _x] = 220, 440, 800 μM.	110
Figure 5.5	Degradation of CIP by Mn(III/IV) Oxides at pH 5- 7, [HAc/NaAc]= [MOPS] = 10 mM, A-C: [CIP] = 5 μM, [BioMnO _x] = [synthetic MnO ₂] = [BioBleMnO _x] = 0.24 mM; D-F: [BPA] = 4.4 μM, [BioMnO _x] = [synthetic MnO ₂] = [BioBleMnO _x] = 0.8 mM	112
Figure 5.6	Degradation pathways of CIP by BioMnO _x	122

LIST OF FIGURES (CONTD)

Figure 5.7	Mass spectrum of BPA degradation product analyzed by GC/MS	123
Figure 5.8	Proposed degradation pathway of BPA by BioMnO _x	124
Figure A.1	Total Ion chromatogram of CIP degradation products. (A) pH ₀ =3.2; (B) pH ₀ = 6.2	134
Figure B.1	Mn 3s spectra of regular and doped OMS-2	135
Figure C.1	IR spectra of A. MoO ₃ and B. V ₂ O ₅	136
Figure C.2	Raman spectra of A. MoO ₃ and B. V ₂ O ₅	137
Figure D.1	A. Response surface of degradation efficiency as a function of C _{cip} and pH; B. Response surface of degradation efficiency as a function of C _{cip} and reaction time	138
Figure E.1	BioMnO _x standard curve by turbidity measurement (OD ₆₀₀)	139
Figure E.2	BioMnO _x standard curve by LBB assay (ABS ₆₁₈)	139
Figure E.3	Correlation of turbidity and LBB assay measurement	140

LIST OF TABLES AND SCHEME

Table 2.1	Mass spectrum profiles of peaks for CIP degradation intermediates.	39
Table 3.1	Variable ranges and values of central composite design for degradation of CIP by OMS-2 type manganese oxides	53
Table 3.2	Surface characterization of regular and doped OMS-2	56
Table 3.3	ANOVA analysis of the derived response surface model	63
Table 3.4	Fitted k_{app} of CIP degradation under various pH conditions and different 9% Mo/OMS-2 dosage, $C_{cip}= 50 \mu\text{M}$	66
Table 3.5	Inhibition of Mn^{II} on oxidative reactivity of manganese (III/IV) oxides	69
Table 3.6	CIP degradation products analysis	70
Table 4.1	Evaluation the effects of superoxide on Mn(II) oxidation	87
Table 4.2	Effect of chemical inhibitors on MOF activity	89
Table 5.1	Surface analysis of Mn(III/IV) oxides	108
Table 5.2	Rate constants of CIP and BPA degradation by BioMnO_x and BioBleMnO_x at different pH conditions.	113
Table 5.3	Rate constants of CIP and BPA degradation in presence of co-solutes by BioMnO_x and BioBleMnO_x	118
Table 5.4	Proposed structures of degradation products of CIP	121

LIST OF ABBREVIATIONS

- AFT:** Anodic Fenton treatment
- AOPs:** Advanced oxidation processes
- BET:** Brunauer-Emmett-Teller
- BPA:** Bisphenol A
- CIP:** Ciprofloxacin
- DFT:** Density functional theory
- EDX:** Energy dispersive X-ray spectroscopy
- FTIR:** Fourier Transform Infrared Spectroscopy
- GC:** Gas chromatography
- HA:** Humic acid
- HPLC:** High performance liquid chromatography
- LC-MS:** Liquid chromatography-mass spectrometry
- MOF:** manganese oxidizing factor
- SEM:** Scanning Electron Microscopy
- TGA:** Thermal gravimetric analysis
- WWTP:** Wastewater treatment plants
- XRD:** X-ray diffraction
- XPS:** X-ray photoelectron spectroscopy

CHAPTER 1

INTRODUCTION TO THESIS RESEARCH

The release of trace organic contaminants into the environment from wastewater effluents has gained recent attention for their wide occurrence in the aquatic environment and potential harmful impacts on wildlife and human health (1-4). Two major groups of contaminants of growing concern are pharmaceuticals and endocrine disrupting compounds (EDCs). Unlike conventional pollutants, pharmaceuticals and EDCs are unlikely to exert overt and acute toxic effects on organisms at environmentally relevant concentrations. However, subtle, unintended and chronic effects may occur due to low and consistent exposure. In addition, for contaminants that have U or V shaped dose-response relationships, such as steroid compounds, low concentration exposure is more toxicologically relevant (5).

Despite limited understanding of the ecological risks posed by the presence of such trace contaminants, adverse effects have been observed on aquatic organisms in both laboratory and field studies (5-12, 14-16). Abnormal concentrations of sex steroid hormones, elevated concentrations of the estrogen-dependent blood protein vitellogenin (VTG), and gonadal malformations have been found in fish associated with estrogenic WWTP effluents (6-8). Moreover, incidence and severity of intersex fish in wild roach populations were found to be correlated with their estimated exposure to steroidal estrogens (9). Xenoestrogens that do not have a steroid structure, such as bisphenol A (BPA), and octylphenol, can also mimic the action of hormones and cause alterations in development and reproduction in wildlife (10, 11).

Another major concern about pharmaceuticals in the environment is antibiotic exposure, which may assist in development and spread of microbial resistance. Prolonged exposure to low doses of antibiotics leads to selective proliferation of resistant bacteria, as evidenced by detection of

several antibiotic resistant bacteria or genes in municipal wastewater discharge and their downstream receiving waters (12, 13). What is worse, the resistant genes may be transferred within and between microbial populations, posing a potential threat to public health (14).

Unexpected effects on untargeted organisms may also occur. Aquatic microcosm studies have revealed that fluoroquinolone antibiotics can perturb photosynthetic species although they were originally designed to target bacterial DNA gyrase or topoisomerase II enzyme and inhibit bacterial DNA replication and repair (15, 16). Ciprofloxacin (CIP), a widely used fluoroquinolone(FQ) antibiotic, was found to affect the structure and richness of algal communities exposed to environmentally relevant concentrations (15). Structure-activity analysis indicates that the quinolone ring and secondary amino group known to be representative in most FQ antibiotic structures may function as quinine site inhibitors in photosystem II (PSII) and thus interfere with the enzyme (17).

It is noteworthy that contaminants exist in a complicated mixture in wastewater. Additive or synergistic toxic effects of co-existing contaminants should be factored in when evaluating the ecological risks. For example, beta-blockers have low toxicity when in pure solution but are much more toxic in a wastewater matrix at environmentally relevant concentrations (18). Another scenario for consideration is exposure to multiple contaminants that share the same mode of action, as often seen in antibiotic families that share similar structures, resulting in a higher effective exposure due to additive effects.

A primary source of the trace organic contaminants in the aquatic environment is sewage effluent (5). Thus wastewater treatment plants (WWTPs) represent a critical control point to prevent low levels of pharmaceuticals and EDCs from entering the aquatic environment. However, conventional treatment methods in WWTP are not specifically designed to treat these

specialized organic contaminants and are often not very effective (19-21). The treatment efficiency depends on the design and operation parameters of the treatment process as well as the intrinsic chemical properties and structures of the contaminants (22-24). Generally, two main elimination mechanisms are responsible for removal in conventional WWTPs: <1> sorption and <2> biodegradation. Sorption to suspended solids by hydrophobic interaction or electrostatic attraction and later precipitation as primary sludge or secondary sludge works well for hydrophobic or positively charged compounds, such as fluoroquinolones and tetracyclines (25,26). However, sorption of highly polar and negatively charged pharmaceuticals, such as clofibric acid, is negligible (27). The other important process is biodegradation. In the presence of sufficient nutrients, co-metabolism of low concentration organic contaminants may occur. For example, ibuprofen can be removed by biodegradation to a significant extent (28). However, the biodegradation process may be slow and require an adaptation period for such unconventional substrates. In addition, some compounds, such as antibiotics, have a very limited biodegradability (29). It is also noteworthy that during the biological process some microorganisms can convert the bioactive metabolites (glucuronide or sulfate conjugates) back to the parent compounds, leading to a lower apparent removal rate (30,31).

Due to the incomplete removal of trace contaminants, detection of pharmaceuticals and EDCs has been frequently reported in the effluent of WWTPs, typically in the $\mu\text{g/L}$ - ng/L concentration range (21, 24, 27). Efforts have been made to improve the treatment efficiency, including optimization of plant design and application of post treatment technology (19, 28, 32). Processes that have undergone investigation include granular activated carbon, membrane separation and oxidation. While the former two techniques utilize physical separation and yield waste that requires further treatment, oxidation processes can alter the structure of chemicals and therefore

their bioactivity. Typical oxidation processes include ozonation, chlorination, UV/H₂O₂, and the Fenton reaction. Precautions should be taken when applying these methods because each method has its specific experimental conditions, appropriate targets, and limitations. For example, ozone is a selective oxidant that works well for some functional groups, such as aromatic rings, C=C, thiols and amines (33). Compounds without those functional groups may be refractory to ozonation, such as halogenated X-ray contrast media and some acidic pharmaceuticals (34). On the contrary, advanced oxidation processes, characterized by the hydroxyl radical, give non-selective oxidation, resulting in contaminant mineralization and improved biodegradability (35, 36). It is noteworthy that sometimes more toxic compounds can be formed after the treatment. Such phenomena have been observed in chlorination studies of acetaminophen, which created more toxic compounds (37). Moreover, degradation of the parent compound does not guarantee removal of pharmaceutical activity of the solution since functional groups that are responsible for biological activity may remain unaffected. Therefore, it is necessary to study treatment methods in detail and understand the specifications and limitations.

Among different oxidation processes, Fenton and manganese oxide systems are attractive options due to their low cost, environmental friendliness and high oxidizing potential. Three oxidation systems, the anodic Fenton system, cryptomelane-type manganese oxides and biogenic manganese oxides (BioMnO_x), are evaluated for their potential in treating pharmaceuticals and EDCs in the following chapters.

The anodic Fenton system (AFT) consists of an electrolytic cell with an iron plate as the anode and a graphite electrode as the cathode. A scheme of the reactor is shown in **Figure 1.1**. The two half cells are separated by an ion exchange membrane for the purpose of pH optimization.

Hydrogen peroxide is pumped into the anodic half cell to initiate the reaction. The mechanism of the AFT system is shown as below:

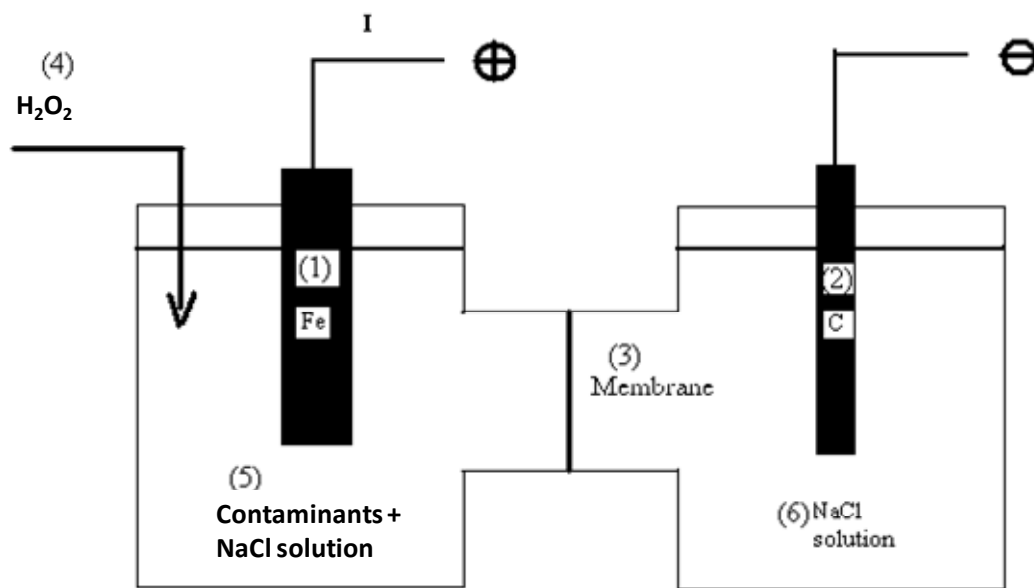
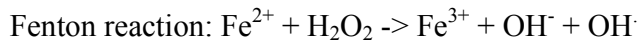
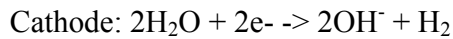
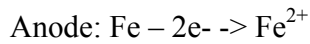


Figure 1.1 Scheme of membrane anodic Fenton Treatment System

Compared to the classical Fenton system, AFT has the advantages of self-optimized pH and sludge reduction (38). This treatment has been successfully applied to remove various pesticides in aqueous and sediment systems (39-41). Generally the degradation is very fast and the treatment is completed in minutes. Kinetic models have been discussed and developed to describe the process (38). Extending application of AFT to sulfamide antibiotics has also been successful. Reduced antibiotic activity of the treated solution was demonstrated by an algal growth assay (42). It is noteworthy that in addition to system condition parameters, such as electrolysis current and H_2O_2 delivery rates, the structure of target pollutants also affect the

degradation kinetics. For example, aromatic N containing compounds like triazine may chelate with the iron and change the amount of available catalytic iron for the Fenton reaction, leading to a change in the kinetic pattern (42, 43). Considering the vast variety of structures presented by pharmaceuticals and EDCs, it is not possible to make a generalization for those compounds in the AFT system. Therefore using compounds with representative structures may be helpful for evaluating treatment efficiency, optimizing process parameters and understanding the mechanisms.

Manganese is another abundant transition metal in the earth that shares great chemical similarity with iron. The most common oxidation states of manganese in the environment are +2, +3 and +4. In the absence of a chelator, Mn(III) and Mn(IV) are sparingly soluble and exist in the oxide form. The structures of manganese dioxides can be categorized into two types, depending on the connection pattern of the MnO_6 octahedral units: 1. framework structure, where MnO_6 octahedral chains formed different sizes of tunnel by sharing corners and edges, such as cryptomelane; 2. Layered type structure, where MnO_6 units form a layer, and cations sit in the interlayer space to balance the charge, such as birnessite.

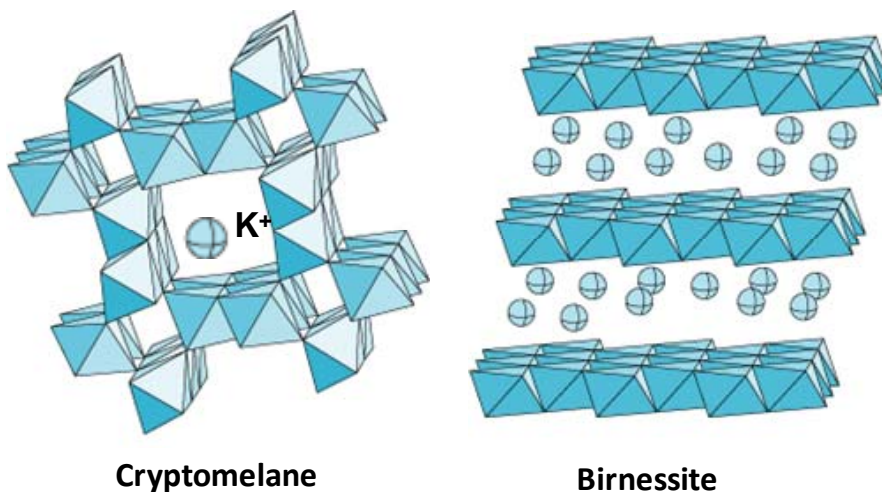


Figure 1.2 Two types of manganese oxide structures

Due to the wide distribution in the environment and the highly reactive surface, manganese oxides have been recognized as an important environmental oxidant. The research interest of exploring the potential of manganese oxides for treating organic contaminants is the result of numerous laboratory and field studies that demonstrate the oxidative versatility of manganese oxides (44 - 48). Interestingly, the reactivity of manganese oxides varies significantly, depending on factors such as mineral phases, average oxidation states of Mn and surface areas (49).

It is generally believed that a biological Mn(II) oxidation process is the predominant pathway for Mn(III/IV) oxide formation in the natural environment due to limited rates of abiotic oxidation of Mn(II) at circum-neutral conditions (50, 51). In addition, various microorganisms are found to perform Mn(II) oxidation directly or indirectly (52). The importance of microbial contributions to Mn(II) oxidation is also confirmed in a few field studies (53-55).

Manganese oxides have been synthesized and used in the laboratory to understand the environmental roles of natural manganese oxides. Birnessite type manganese oxides, the structural analog of neoformed BioMnO_x, have gained considerable research interest. High oxidizing reactivity of this type of manganese oxides has been reported, where phenols, amines and small organic acids are degraded in minutes (45, 56, 57). Emerging contaminants that have reactive functional groups, such as triclosan and fluoroquinolones, are also found susceptible to oxidation (46, 58). Based on the above findings, it is reasonable to hypothesize that BioMnO_x may play a key role in environmental fates of trace organic contaminants and, further, be a potential oxidant for water treatment application. However, it is worth noting that the reactivity of BioMnO_x cannot be reliably predicted from prior knowledge of its synthetic analogs despite the structural similarity (59-61). One major difference between BioMnO_x and its synthetic counterpart is the content of organic materials. The organic debris in BioMnO_x, such as cell

material, may serve as a ligand for Mn(II) and other metal ions. This chelating process is especially important during redox reactions where Mn(II) is released, leading to auto-inhibition of the reaction by blocking of the reactive sites (62). Similarly, inhibition due to co-existing metal ions in the water matrix can be mitigated by such chelation. BioMnO_x may also differ from the synthetic ones in particle size distribution, surface areas and average oxidation states. All of those factors can affect the reactivity of BioMnO_x, leading to different degradation rates and even pathways. Therefore research efforts are needed to obtain such information for evaluating environmental roles of natural manganese oxides and utilizing them for water treatment.

Cryptomelane is a naturally occurring framework type manganese oxide that has gained considerable interest regarding its potential application in environmental pollution control (63-65). The synthetic counterpart of cryptomelane is called octahedral molecular sieve-2 (OMS-2), where 2 stands for the dimension size of the tunnel formed by MnO₆ octahedral units. OMS-2 has been successfully applied for heavy metal immobilization, volatile organic compounds reduction and dye wastewater treatment (64, 66, 67). Despite the effectiveness of OMS-2 in treating dye wastewater, there are limited data on the OMS-2 application as a water treatment process. Generally, the reaction between manganese oxides and organic contaminants is considered to be a two step surface reaction with formation of a complex precursor followed by electron transfer (46). Thus modification of manganese oxides that leads to a larger surface area or faster electron transfer rates can result in an improvement of treatment efficiency. Doping OMS-2 with certain transition metals has been reported to give better dye pollutant removal rates which may be partially due to the surface area change (67). Based on the above discussion, it is scientifically interesting to evaluate the performance of OMS-2 and its derivatives for treating emerging contaminants.

The main objectives of this study are to evaluate the effectiveness of three oxidation processes: anodic Fenton treatment, cryptomelane-type manganese oxides and BioMnO_x, for treating representative pharmaceuticals and EDCs in aqueous solution. Degradation kinetics are modeled for each system and process conditions are optimized. Efforts are made to identify degradation products for each oxidation process; changes of biological activity after the treatments are discussed. Chapter 2 describes degradation of CIP in the anodic Fenton treatment system. Effects of initial solution pH, Fenton reagent delivery rates and CIP initial concentration on degradation kinetics are investigated. Degradation of reference compounds and density functional calculation are conducted to understand the treatment process. Chapter 3 describes degradation of CIP by cryptomelane-type manganese oxides: OMS-2 and doped OMS-2. Effects of doping on structure and reactivity of cryptomelane-type manganese oxides are investigated. Process parameters such as pH, oxidant load, are optimized by surface response methodology. Chapter 4 focuses on describing and understanding the formation of BioMnO_x by *Leptothrix discophora SS-1*, a model Mn(II) oxidizing bacterium. Optimal conditions for manganese oxide formation are discussed. Chapter 5 utilizes pre-formed BioMnO_x as the oxidant to degrade CIP and BPA. The oxidation kinetics by BioMnO_x is compared to those by its synthetic analog. Effects of solution conditions on the kinetics are also discussed. Degradation products in BioMnO_x are discussed and compared to the findings in synthetic analog systems.

References

1. Snyder, S.A. Occurrence, treatment, and toxicological relevance of EDCs and pharmaceuticals in water. *Ozone: Science and Engineering* **2008**, *30*, 65-69.

2. Kolpin, D.W.; Furlong, E.T.; Meyer, M.T.; Thurman, E.M.; Zaugg, S.D.; Barber, L.B.; Buxton, H.T. Pharmaceuticals, hormones, and other organic wastewater contaminants in US streams, 1999-2000: a national reconnaissance. *Environ. Sci. Technol.* **2002**, *36*, 1202-1211.
3. Loraine, G.A. and Pettigrove, M.E. Seasonal variations in concentrations of pharmaceuticals and personal care products in drinking water and reclaimed wastewater in southern California. *Environ. Sci. Technol.* **2006**, *40*, 687-695.
4. Stackelberg, P.E.; Furlong, E.T.; Meyer, M.T.; Zaugg, S.D.; Henderson, A.K.; Reissman, D.B. Persistence of pharmaceutical compounds and other organic wastewater contaminants in a conventional drinking-water-treatment plant. *Sci. Total Environ.* **2004**, *329*, 99-113.
5. Daughton, C.G. Pharmaceuticals and personal care products in the environment: overarching issues and overview. **2001**, *791*, 2-38.
6. Rodgers-Gray, T.P.; Jobling, S.; Morris, S.; Kelly, C.; Kirby, S.; Janbakhsh, A.; Harries, J.E.; Waldock, M.J.; Sumpter, J.P.; Tyler, C.R. Long-term temporal changes in the estrogenic composition of treated sewage effluent and its biological effects on fish. *Environ. Sci. Technol.* **2000**, *34*, 1521-1528.
7. Vajda, A.M.; Barber, L.B.; Gray, J.L.; Lopez, E.M.; Woodling, J.D.; Norris, D.O. Reproductive disruption in fish downstream from an estrogenic wastewater effluent. *Environ. Sci. Technol.* **2008**, *42*, 3407-3414.
8. Jobling, S.; Nolan, M.; Tyler, C.R.; Brighty, G.; Sumpter, J.P. Widespread sexual disruption in wild fish. *Environ. Sci. Technol.* **1998**, *32*, 2498-2506.
9. Jobling, S.; Williams, R.; Johnson, A.; Taylor, A.; Gross-Sorokin, M.; Nolan, M.; Tyler, C.R.; Van Aerle, R.; Santos, E.; Brighty, G. Predicted exposures to steroid estrogens in UK rivers

correlate with widespread sexual disruption in wild fish populations. *Environ. Health Perspect.* **2006**, *114*, 32.

10. Gibson, R.; Smith, M.; Spary, C.; Tyler, C.; Hill, E. Mixtures of estrogenic contaminants in bile of fish exposed to wastewater treatment works effluents. *Environ. Sci. Technol.* **2005**, *39*, 2461-2471.

11. Jobling, S.; Casey, D.; Rodgers-Gray, T.; Oehlmann, J.; Schulte-Oehlmann, U.; Pawlowski, S.; Baunbeck, T.; Turner, A.; Tyler, C. Comparative responses of molluscs and fish to environmental estrogens and an estrogenic effluent. *Aquatic Toxicology* **2003**, *65*, 205-220.

12. Sarmah, A.K.; Meyer, M.T.; Boxall, A.B.A. A global perspective on the use, sales, exposure pathways, occurrence, fate and effects of veterinary antibiotics (VAs) in the environment. *Chemosphere* **2006**, *65*, 725-759.

13. Goni-Urriza, M.; Capdepuy, M.; Arpin, C.; Raymond, N.; Caumette, P.; Quentin, C. Impact of an Urban Effluent on Antibiotic Resistance of Riverine Enterobacteriaceae and *Aeromonas* spp. *Appl. Environ. Microbiol.* **2000**, *66*, 125-132.

14. Kümmerer, K. Significance of antibiotics in the environment. *J. Antimicrob. Chemother.* **2003**, *52*, 5-7.

15. Wilson, B.A.; Smith, V.H.; Denoyelles Jr, F.; Larive, C.K. Effects of three pharmaceutical and personal care products on natural freshwater algal assemblages. *Environ. Sci. Technol.* **2003**, *37*, 1713-1719.

16. Richards, S.M.; Wilson, C.J.; Johnson, D.J.; Castle, D.M.; Lam, M.; Mabury, S.A.; Sibley, P.K.; Solomon, K.R. Effects of pharmaceutical mixtures in aquatic microcosms. *Environmental Toxicology and Chemistry* **2004**, *23*, 1035-1042.

17. Aristilde, L.; Melis, A.; Sposito, G. Inhibition of photosynthesis by a fluoroquinolone antibiotic. *Environ. Sci. Technol.* **2010**, *44*, 1444-1450.
18. Hernando, M.D.; Petrovic, M.; Fernández-Alba, A.; Barceló, D. Analysis by liquid chromatography–electrospray ionization tandem mass spectrometry and acute toxicity evaluation for β -blockers and lipid-regulating agents in wastewater samples. *Journal of chromatography A* **2004**, *1046*, 133-140.
19. Esplugas, S.; Bila, D.M.; Krause, L.G.T.; Dezotti, M. Ozonation and advanced oxidation technologies to remove endocrine disrupting chemicals (EDCs) and pharmaceuticals and personal care products (PPCPs) in water effluents. *J. Hazard. Mater.* **2007**, *149*, 631-642.
20. Paxeus, N. Removal of selected non-steroidal anti-inflammatory drugs (NSAIDs), gemfibrozil, carbamazepine, beta-blockers, trimethoprim and triclosan in conventional wastewater treatment plants in five EU countries and their discharge to the aquatic environment. *Water Sci. Technol.* **2004**, *50*, 253-260.
21. Boyd, G.R.; Reemtsma, H.; Grimm, D.A.; Mitra, S. Pharmaceuticals and personal care products (PPCPs) in surface and treated waters of Louisiana, USA and Ontario, Canada. *Sci. Total Environ.* **2003**, *311*, 135-149.
22. Joss, A.; Andersen, H.; Ternes, T.; Richle, P.R.; Siegrist, H. Removal of estrogens in municipal wastewater treatment under aerobic and anaerobic conditions: consequences for plant optimization. *Environ. Sci. Technol.* **2004**, *38*, 3047-3055.
23. Ternes, T.A.; Joss, A.; Siegrist, H. Peer reviewed: scrutinizing pharmaceuticals and personal care products in wastewater treatment. *Environ. Sci. Technol.* **2004**, *38*, 392-399.
24. Castiglioni, S.; Bagnati, R.; Fanelli, R.; Pomati, F.; Calamari, D.; Zuccato, E. Removal of pharmaceuticals in sewage treatment plants in Italy. *Environ. Sci. Technol.* **2006**, *40*, 357-363.

25. Kim, S.; Eichhorn, P.; Jensen, J.N.; Weber, A.S.; Aga, D.S. Removal of antibiotics in wastewater: effect of hydraulic and solid retention times on the fate of tetracycline in the activated sludge process. *Environ. Sci. Technol.* **2005**, *39*, 5816-5823.
26. Li, B. and Zhang, T. Biodegradation and adsorption of antibiotics in the activated sludge process. *Environ. Sci. Technol.* **2010**, *44*, 3468-3473.
27. Paxeus, N. Removal of selected non-steroidal anti-inflammatory drugs (NSAIDs), gemfibrozil, carbamazepine, beta-blockers, trimethoprim and triclosan in conventional wastewater treatment plants in five EU countries and their discharge to the aquatic environment. *Water Sci. Technol.* **2004**, *50*, 253-260.
28. Smook, T.M.; Zho, H.; Zytner, R.G. Removal of ibuprofen from wastewater: comparing biodegradation in conventional, membrane bioreactor, and biological nutrient removal treatment systems. *Water Sci. Technol.* **2008**, *57*, 1-8.
29. Alexy, R.; Kümpel, T.; Kümmerer, K. Assessment of degradation of 18 antibiotics in the closed bottle test. *Chemosphere* **2004**, *57*, 505-512.
30. Leusch, F.D.L.; Chapman, H.F.; van den Heuvel, M.R.; Tan, B.L.L.; Gooneratne, S.R.; Tremblay, L.A. Bioassay-derived androgenic and estrogenic activity in municipal sewage in Australia and New Zealand. *Ecotoxicol. Environ. Saf.* **2006**, *65*, 403-411.
31. Sun, Q.; Deng, S.; Huang, J.; Shen, G.; Yu, G. Contributors to estrogenic activity in wastewater from a large wastewater treatment plant in Beijing, China. *Environ. Toxicol. Pharmacol.* **2008**, *25*, 20-26.
32. Rudder, J.; Wiele, T.; Dhooge, W.; Comhaire, F.; Verstraete, W. Advanced water treatment with manganese oxide for the removal of 17 [alpha]-ethynylestradiol (EE2). *Water Res.* **2004**, *38*, 184-192.

33. Ternes, T.A.; Stüber, J.; Herrmann, N.; McDowell, D.; Ried, A.; Kampmann, M.; Teiser, B. Ozonation: a tool for removal of pharmaceuticals, contrast media and musk fragrances from wastewater? *Water Res.* **2003**, *37*, 1976-1982.
34. Huber, M.M.; Göbel, A.; Joss, A.; Hermann, N.; Löffler, D.; McArdell, C.S.; Ried, A.; Siegrist, H.; Ternes, T.A.; von Gunten, U. Oxidation of pharmaceuticals during ozonation of municipal wastewater effluents: a pilot study. *Environ. Sci. Technol.* **2005**, *39*, 4290-4299.
35. Ikehata, K.; Naghashkar, N.J.; El-Din, M.G. Degradation of aqueous pharmaceuticals by ozonation and advanced oxidation processes: A review. *Ozone: Science and Engineering* **2006**, *28*, 353-414.
36. Tekin, H.; Bilkay, O.; Ataberk, S.S.; Balta, T.H.; Ceribasi, I.H.; Sanin, F.D.; Dilek, F.B.; Yetis, U. Use of Fenton oxidation to improve the biodegradability of a pharmaceutical wastewater. *J. Hazard. Mater.* **2006**, *136*, 258-265.
37. Bedner, M. and MacCrehan, W.A. Transformation of acetaminophen by chlorination produces the toxicants 1, 4-benzoquinone and N-acetyl-p-benzoquinone imine. *Environ. Sci. Technol.* **2006**, *40*, 516-522.
38. Wang, Q. and Lemley, A.T. Kinetic model and optimization of 2, 4-D degradation by anodic Fenton treatment. *Environ. Sci. Technol.* **2001**, *35*, 4509-4514.
39. Wang, Q. and Lemley, A.T. Oxidation of carbaryl in aqueous solution by membrane anodic Fenton treatment. *J. Agric. Food Chem.* **2002**, *50*, 2331-2337.
40. Wang, Q. and Lemley, A.T. Kinetic effect of humic acid on alachlor degradation by anodic Fenton treatment. *J. Environ. Qual.* **2004**, *33*, 2343-2352.

41. Ye, P. and Lemley, A.T. Adsorption Effect on the Degradation of Carbaryl, Mecoprop, and Paraquat by Anodic Fenton Treatment in an SWy-2 Montmorillonite Clay Slurry. *J. Agric. Food Chem.* **2008**, *56*, 10200-10207.
42. Neafsey, K.; Zeng, X.; Lemley, A.T. Degradation of sulfonamides in aqueous solution by membrane anodic Fenton treatment. *J. Agric. Food Chem.* **2009**, *58*, 1068-1076.
43. Wang, Q.; Scherer, E.M.; Lemley, A.T. Metribuzin degradation by membrane anodic Fenton treatment and its interaction with ferric ion. *Environ. Sci. Technol.* **2004**, *38*, 1221-1227.
44. Laha, S. and Luthy, R.G. Oxidation of aniline and other primary aromatic amines by manganese dioxide. *Environ. Sci. Technol.* **1990**, *24*, 363-373.
45. McBride, M. Adsorption and oxidation of phenolic compounds by iron and manganese oxides. *Soil Sci. Soc. Am. J.* **1987**, *51*, 1466-1472.
46. Zhang, H. and Huang, C.H. Oxidative transformation of triclosan and chlorophene by manganese oxides. *Environ. Sci. Technol.* **2003**, *37*, 2421-2430.
47. Chen, W.; Ding, Y.; Johnston, C.T.; Teppen, B.J.; Boyd, S.A.; Li, H. Reaction of Lincosamide Antibiotics with Manganese Oxide in Aqueous Solution. *Environ. Sci. Technol.* **2010**, *44*, 4486-4492.
48. Lafferty, B.J.; Ginder-Vogel, M.; Zhu, M.; Livi, K.J.T.; Sparks, D.L. Arsenite Oxidation by a Poorly Crystalline Manganese-Oxide. 2. Results from X-ray Absorption Spectroscopy and X-ray Diffraction. *Environ. Sci. Technol.* **2010**, *44*, 8467-8472.
49. Liu, C.; Zhang, L.; Li, F.; Wang, Y.; Gao, Y.; Li, X.; Cao, W.; Feng, C.; Dong, J.; Sun, L. Dependence of Sulfadiazine Oxidative Degradation on Physicochemical Properties of Manganese Dioxides. *Ind Eng Chem Res* **2009**, *48*, 10408-10413.

50. Diem, D. and Stumm, W. Is dissolved Mn^{2+} being oxidized by O_2 in absence of Mn-bacteria or surface catalysts? *Geochim. Cosmochim. Acta* **1984**, *48*, 1571-1573.
51. Tebo, B.M.; Bargar, J.R.; Clement, B.G.; Dick, G.J.; Murray, K.J.; Parker, D.; Verity, R.; Webb, S.M. Biogenic manganese oxides: properties and mechanisms of formation. *Annu. Rev. Earth Planet. Sci.* **2004**, *32*, 287-328.
52. Tebo, B.M.; Johnson, H.A.; McCarthy, J.K.; Templeton, A.S. Geomicrobiology of manganese (II) oxidation. *Trends Microbiol.* **2005**, *13*, 421-428.
53. Emerson, S.; Kalthorn, S.; Jacobs, L.; Tebo, B.M.; Nealson, K.H.; Rosson, R.A. Environmental oxidation rate of manganese (II): bacterial catalysis. *Geochim. Cosmochim. Acta* **1982**, *46*, 1073-1079.
54. Fuller, C.C. and Harvey, J.W. Reactive uptake of trace metals in the hyporheic zone of a mining-contaminated stream, Pinal Creek, Arizona. *Environ. Sci. Technol.* **2000**, *34*, 1150-1155.
55. Kay, J.T.; Conklin, M.H.; Fuller, C.C.; O'Day, P.A. Processes of nickel and cobalt uptake by a manganese oxide forming sediment in Pinal Creek, Globe Mining District, Arizona. *Environ. Sci. Technol.* **2001**, *35*, 4719-4725.
56. Stone, A.T. Reductive dissolution of manganese (III/IV) oxides by substituted phenols. *Environ. Sci. Technol.* **1987**, *21*, 979-988.
57. Stone, A.T. and Morgan, J.J. Reduction and dissolution of manganese (III) and manganese (IV) oxides by organics: 2. Survey of the reactivity of organics. *Environ. Sci. Technol.* **1984**, *18*, 617-624.
58. Zhang, H. and Huang, C. Oxidative Transformation of Fluoroquinolone Antibacterial Agents and Structurally Related Amines by Manganese Oxide. *Environ. Sci. Technol.* **2005**, *39*, 4474-4483.

59. He, J.; Meng, Y.; Zheng, Y.; Zhang, L. Cr(III) oxidation coupled with Mn(II) bacterial oxidation in the environment. *Journal of Soils and Sediments* **2010**, *10*, 767-773.
60. Forrez, I.; Carballa, M.; Verbeken, K.; Vanhaecke, L.; , M.S.; Ternes, T.; Boon, N.; Verstraete, W. Diclofenac Oxidation by Biogenic Manganese Oxides. *Environ. Sci. Technol.* **2010**, *44*, 3449-3454.
61. Nelson, Y.M.; Lion, L.W.; Ghiorse, W.C.; Shuler, M.L. Production of biogenic Mn oxides by *Leptothrix discophora* SS-1 in a chemically defined growth medium and evaluation of their Pb adsorption characteristics. *Appl. Environ. Microbiol.* **1999**, *65*, 175.
62. Lin, K.; Liu, W.; Gan, J. Oxidative removal of bisphenol A by manganese dioxide: efficacy, products, and pathways. *Environ. Sci. Technol.* **2009**, *43*, 3860-3864.
63. Sun, L.; Cao, Q.; Hu, B.; Li, J.; Hao, J.; Jing, G.; Tang, X. Synthesis, characterization and catalytic activities of vanadium–cryptomelane manganese oxides in low-temperature NO reduction with NH₃. *Applied Catalysis A: General* **2011**, *393*, 323-330.
64. Hu, B.; Chen, C.; Frueh, S.J.; Jin, L.; Joesten, R.; Suib, S.L. Removal of Aqueous Phenol by Adsorption and Oxidation with Doped Hydrophobic Cryptomelane-Type Manganese Oxide (K–OMS-2) Nanofibers. *The Journal of Physical Chemistry C* **2010**, *114*, 9835-9844.
65. Lemus, M.A.; López, T.; Recillas, S.; Frías, D.; Montes, M.; Delgado, J.; Centeno, M.; Odriozola, J. Photocatalytic degradation of 2, 4-dichlorophenoxyacetic acid using nanocrystalline cryptomelane composite catalysts. *Journal of Molecular Catalysis A: Chemical* **2008**, *281*, 107-112.
66. Zhang, T.; Zhang, X.; Ng, J.; Yang, H.; Liu, J.; Sun, D.D. Fabrication of magnetic cryptomelane-type manganese oxide nanowires for water treatment. *Chem. Commun.* **2011**,

67. Sriskandakumar, T.; Opembe, N.; Chen, C.H.; Morey, A.; King'onde, C.; Suib, S.L. Green Decomposition of Organic Dyes Using Octahedral Molecular Sieve Manganese Oxide Catalysts. *The Journal of Physical Chemistry A* **2009**, *113*, 1523-1530.

CHAPTER 2

SPECIES DEPENDENT DEGRADATION OF CIPROFLOXACIN IN THE MEMBRANE ANODIC FENTON SYSTEM

Xiao Xiao, Xia Zeng and Ann T. Lemley

Graduate Field of Environmental Toxicology, FSAD, MVR Hall, Cornell University,

Ithaca, New York 14853-4401

Abstract

The anodic Fenton treatment method (AFT) was successfully applied to the removal of Ciprofloxacin (CIP), a widely used fluoroquinolone antibiotic, from aqueous solution. Degradation kinetics were found to be species dependent. At initial pH 3.2, CIP remained in its cationic form and the kinetics followed a previously developed AFT model. At an initial near-neutral pH, CIP speciation changed during the degradation, due to pH changes over the process, and no obvious model fit the data. Density functional theory (DFT) calculations indicated a protonated species-dependent reaction affinity toward hydroxyl radicals. A new model was derived based on the AFT model with the addition of species distribution during the degradation, and it was shown to describe the degradation kinetics successfully. Degradation of reference compounds further confirmed that the free carboxylic acid group, which contributes to the species changes, plays a key role in the observed degradation pattern. Furthermore, degradation of reference ciprofloxacin-metal complexes confirmed that the formation of these complexes does not have a major effect on the degradation pattern. Optimization of CIP degradation was carried out at pH 3.2 with an optimal $\text{H}_2\text{O}_2:\text{Fe}^{2+}$ ratio found between 10:1 and 15:1. Three degradation pathways were also proposed based on mass spectrometry data: <1> hydroxylation and defluorination on the aromatic ring; <2> oxidative decarboxylation; and <3> oxidation on the piperazine ring and dealkylation. By the end of the AFT treatment, neither CIP nor its degradation products were detected, indicating successful removal of antibacterial properties.

Introduction

Based on their annual global sale and therapeutic versatility, fluoroquinolones represent one of the most important classes of antibiotics (1, 2). They are active against a wide spectrum of bacteria and are considered as “drugs of last resort”. Ciprofloxacin (CIP) is one member of the second-generation of fluoroquinolone derivatives. It is also a primary degradation product of enrofloxacin, another widely used fluoroquinolone drug. The structure of CIP is shown in **Figure 2.1**. CIP possesses a carboxylic acid group in the quinolone moiety (C-3, $pK_{a1} = 6.1$) and an amine group in the piperazine moiety (C-7, $pK_{a2} = 8.7$). Depending on the pH of the solution, CIP can exist as different species: anionic, cationic or zwitterionic form. Speciation of CIP affects its sorption in soil, its photo degradation, and its reaction affinity toward ozone (3-5).

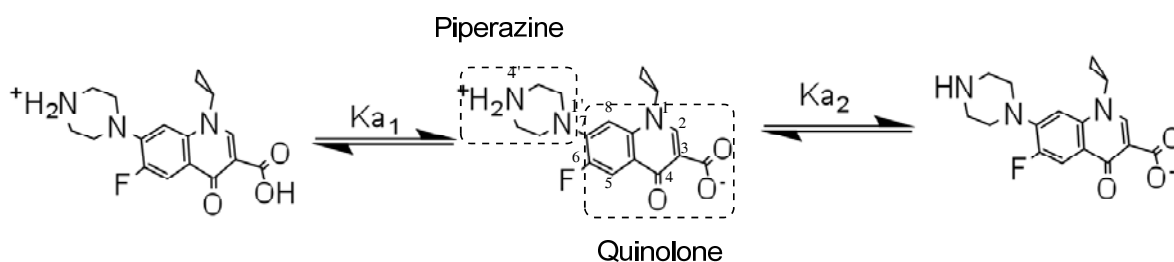


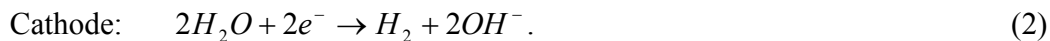
Figure 2.1 Speciation of CIP, $pK_{a1} = 6.1$, $pK_{a2} = 8.8$.

Antibiotics and their metabolites are ultimately discharged into wastewater treatment plants (WWTPs). However, there is a potential for releasing residual compounds into the aquatic environment within the treated effluents due to limited removal efficiency. In fact, CIP has been detected in WWTP effluents in the $\mu\text{g/L}$ concentration range and in the ng/L concentration range in surface water after dilution (6, 7). The presence and accumulation of fluoroquinolone antibiotics, even at low concentrations, may still pose threats to the ecosystem and human health by inducing development and spread of drug resistance in bacteria due to long term exposure. In

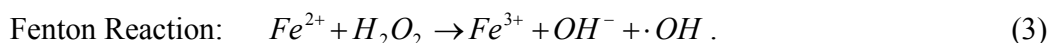
addition, high concentrations of CIP, up to 31 mg/L, have been found in waste effluents from pharmaceutical manufacturers (8). In terms of precaution, it is necessary to explore effective treatment methods for removing contaminants before discharge.

Advanced oxidation processes (AOPs), characterized by hydroxyl radical generation, are attractive options for removing pharmaceuticals due to their capacity to rapidly and completely destroy organic compounds. One of the most employed and studied AOPs is the Fenton/ Fenton-like system. Anodic Fenton treatment (AFT) has been developed in our laboratory and has shown great effectiveness in degrading organic pollutants (9, 10). This treatment system is separated into two half-cells, which are connected by an anion exchange membrane. Sodium chloride is used as background electrolyte with a higher concentration in the cathodic cell.

The ferrous ion is delivered into the anodic half-cell via electrolysis of a sacrificial iron electrode, as shown in the following:



Hydrogen peroxide solution is pumped into the anodic half-cell to initiate the Fenton reaction.



The concentration gradient of Cl^{-} in the two half cells is beneficial for Cl^{-} to compete with OH^{-} in movement across the anion exchange membrane to the anodic cell, exerting less effect on the anodic pH and assisting in development of an optimized acidic pH. A decrease of three pH units from initial circum-neutral pH value has been observed in the anode.

The AFT kinetic model has been developed to simulate pollutant degradation in aqueous systems (9). While the model has been successfully applied to several contaminants, it has not been tested for a compound with changing speciation during the AFT process. Since the pK_{a1} of

CIP falls in the typical working pH range of AFT, species distribution will change due to pH changes during the process. In addition, in a Fenton system CIP may complex with the ferric ion. The extent of complexation depends on solution pH and may affect the degradation process. The purpose of the present study is to: 1) document degradation of CIP in AFT; 2) determine the effect of pH-dependent speciation changes on the degradation process of CIP; 3) develop a kinetic model for CIP degradation; 4) Identify degradation products of CIP and propose degradation pathways in this system.

Materials and methods

Chemicals. All reagents were used without further purification. CIP (98%), 1-phenyl piperazine (99%) and hydrogen peroxide (30%) were purchased from Sigma-Aldrich Chemicals (Milwaukee, WI). 1,6-dimethyl-4-oxo-1,4-dihydroquinoline-3-carboxylic acid (>95%) was purchased from Chembridge Corporation (San Diego, CA). All solutions were prepared from de-ionized water.

Anodic Fenton Treatment. The AFT apparatus consisted of two 400 mL glass half-cells separated by an anion exchange membrane (Electrosynthesis, Lancaster, NY). Typically, 200 mL of CIP solution with a NaCl concentration of 0.05 M and the same volume of 0.20 M NaCl solution were added to the anodic and cathodic half-cells, respectively. The reaction was initiated by turning on the power supply when the first drop of hydrogen peroxide entered the solution in the anodic half-cell. Unless specified otherwise, electric current was kept at 0.040 A, with a Fe^{2+} : H_2O_2 delivery ratio of 1:10. At given time intervals, 1 mL of anodic effluent was collected and transferred to a 2 mL HPLC vial containing 0.1 mL of methanol which quenches hydroxyl radicals. Each treatment was done with three replicates. AFT degradation of CIP-metal complexes (CIP-Al, CIP-Fe), and reference compounds was conducted similarly. CIP-Al and

CIP-Fe complexes were synthesized by addition of excess metal ions into the CIP solution at pH ~ 4. The methyl ester of CIP was synthesized in methanol catalyzed by concentrated sulfuric acid with 4 hours refluxing and was confirmed by mass spectrometry. Esterification of the reference compound 1,6-dimethyl-4-oxo-1,4-dihydroquinoline-3-carboxylic acid was conducted similarly. The pH was adjusted to the desired level before the anodic Fenton treatment.

Analytical methods. The concentrations of CIP, reference compounds and their degradation products were analyzed by a reverse-phase high-performance liquid chromatograph (HPLC) with a diode array UV-Vis detector (HP series 1200, Agilent Technology) and a Restek ultra C18 (5 μm) reverse phase column (4.6 \times 150 mm). The detector wavelength was set at 230-280 nm. Gradient elution was used with the mobile phase containing 0.1% formic acid (eluent A) and acetonitrile (eluent B). Degradation products were identified by an Agilent G1978B Multimode source for 6100 series Single Quadrupole MS in the positive ES mode with a full scan from $m/z = 50$ to $m/z = 350$.

Kinetic Modeling. The derivation of the AFT kinetic model was established in previous work (9). The degradation kinetics of the target organic compound can be described by the following equation:

$$\ln \frac{[C]_t}{[C]_0} = \frac{1}{2} K \lambda \pi \omega v_0^2 t^2, \quad (4)$$

where $K = k k_1$ ($\mu\text{M}^{-2} \text{min}^{-2}$), k ($\mu\text{M}^{-1} \text{min}^{-1}$) and k_1 ($\mu\text{M}^{-1} \text{min}^{-1}$) are the second order rate constants of the Fenton reaction and the reaction between hydroxyl radical and target compound, respectively; $[C]_0$ (μM) and $[C]_t$ (μM) are the concentrations of the target compound at 0 and t min, respectively; λ (min) and π (min) are the average lifetime of the hydroxyl radical and the ferrous ion respectively; ω is a constant related to the delivery ratio of hydrogen peroxide to

ferrous ion and to the consumption ratio of hydrogen peroxide; v_0 ($\mu\text{M min}^{-1}$) is the delivery rate of ferrous ion by electrolysis and t (min) is time.

Density Functional Theory (DFT) Calculation. The hybrid method B3LYP with the standard 6-31G (d) basis set was used to calculate the potential energies of the compounds involved during the reaction of CIP and hydroxyl radicals (Gaussian 03 software). All structures involved in the reaction were located on the potential energy surface by performing full geometry optimization, and their natures were identified by performing frequency calculations.

Experimental Data Analysis. All experiments were carried out in triplicate and all of the figures and statistical analyses were completed using SigmaPlot 9.0.

Results and Discussion

Degradation of CIP at different initial pH values. CIP was degraded at two different initial pH conditions, 3.2 and 6.2-6.8. These two pH ranges were chosen for several reasons. The acidic pH (3.2) is a favorable condition for the Fenton reaction, and it is also an unfavorable condition for complex formation between CIP and ferric ion. Thus, CIP should exist mainly in the cationic form. The pH range of 6.2-6.8 is near the $\text{pK}_{\text{a}1}$ of CIP. With this starting pH, CIP species ratios will change continuously during the self-acidifying AFT process. This range also gives pH values similar to the natural environment. Over the pH range of this study, the piperazinyl 4'-N, which corresponds to $\text{pK}_{\text{a}2}$, remains protonated. Thus, we refer to protonated or deprotonated CIP according to the speciation of the carboxylic acid group (**Figure 2.1**).

AFT treatment worked efficiently to remove CIP at both pH conditions, where a total removal was observed within 4 minutes (**Figure 2.2**). CIP degradation showed different patterns at different initial pH values. At initial pH 3.2, the solution pH remained almost stable during the process and the AFT model fitted the degradation kinetics well with $R^2 > 0.99$. At initial pH 6.2-

6.8, the solution pH changed from above 6 to around 3.7. The degradation data deviated from a typical AFT-type curve with a much faster degradation in the first minute. Neither a first order kinetic model, the AFT model, nor the modified AFT model gave a good fit to the data at this initial pH. (The modified model accounts for a weak interaction between the ferric ion and a heterocyclic nitrogen.)

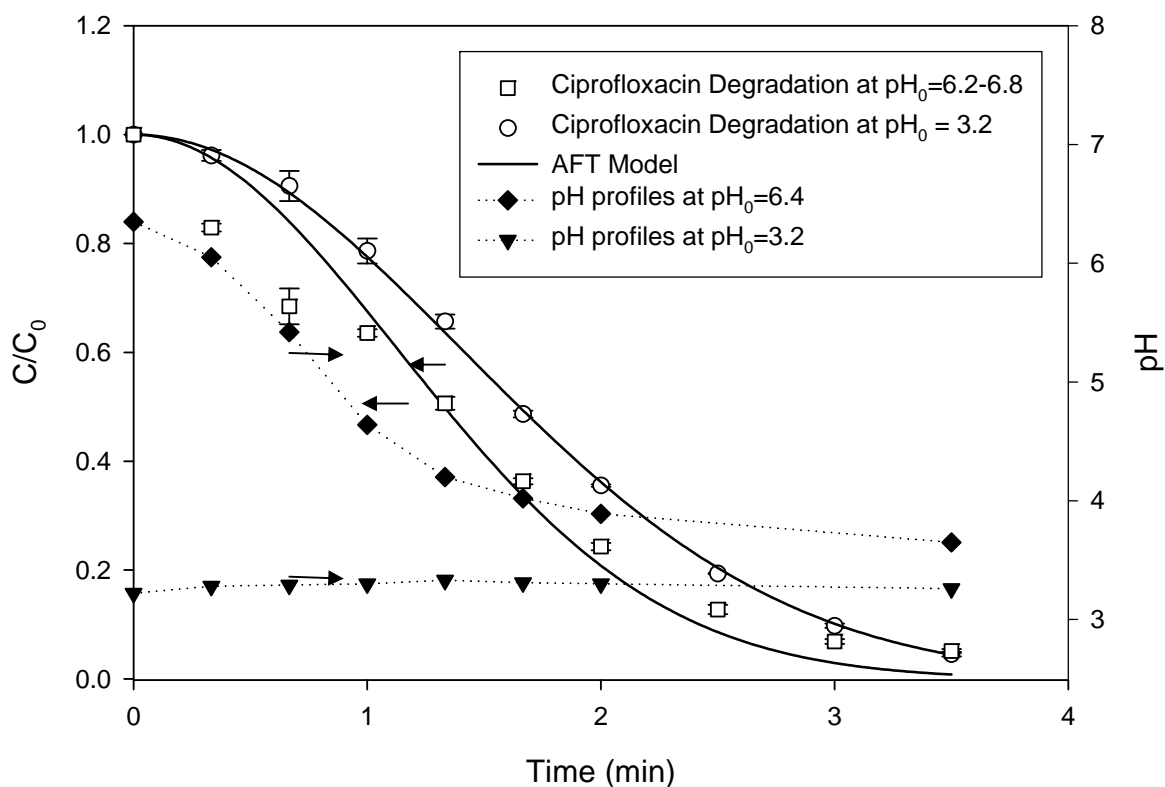


Figure 2.2 Degradation of CIP in AFT system at $pH_0 = 3.2$ and $6.2-6.8$. Current delivery = $0.04A$, $[H_2O_2]:[Fe^{2+}] = 10:1$, $[CIP]_0 = 55 \mu M$.

Degradation of reference compounds. In order to confirm the role of the carboxylic acid functional group in the degradation kinetics observed at the initial pH of $6.2-6.8$, a series of reference compounds, 1-phenyl piperazine (PP), 1,6-dimethyl-4-oxo-1,4-dihydroquinoline-3-carboxylic acid (QA), and the methyl ester of CIP (CIPM) were studied with AFT, similar to the

CIP experiments (**Figure 2.3**). These compounds were chosen to represent the two structural parts of CIP, which correspond to the two protonation sites, and also susceptible sites for ozonation and hydroxyl radical attack (*II*). The reference compound PP has a piperazinyl substituent on the benzene ring, and reference compound QA maintains the quinolone core structure. CIPM was synthesized via methylation of the carboxylic acid. CIPM and PP exist only in the cationic form while QA speciation changes with pH changes during AFT.

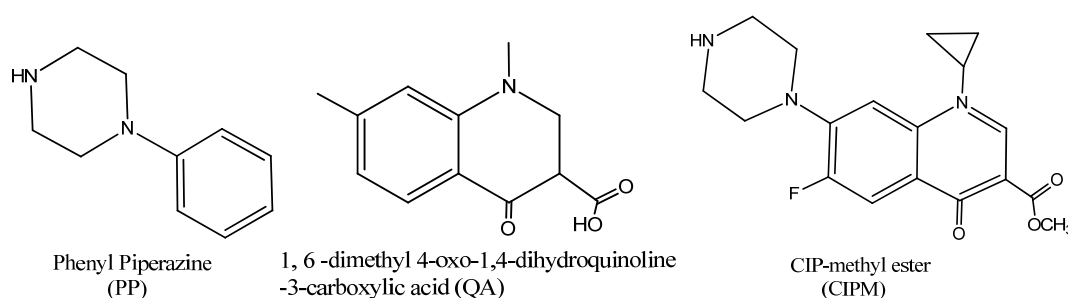


Figure 2.3 Structure of Reference compounds: 1-Phenyl Piperazine, 1,6-dimethyl-4-oxo-1,4-dihydroquinoline-3-carboxylic acid and ciprofloxacin methyl ester.

AFT effectively degraded all of the reference compounds, although different kinetic patterns were observed. At pH 3.2, all of the compounds followed the AFT model, indicating that the model worked well for this optimized, simplified condition (**Figure 2.4A**). At pH 6.2-6.8, the degradation kinetics of PP and CIPM followed the modified AFT model, indicating a weak interaction between the probe chemicals and iron, possibly via the heterocyclic nitrogen. The degradation profile of QA gave an interesting curve that looks similar to CIP-type kinetics at the initial pH, though subtler during the first minute. (**Figure 2.4B**).

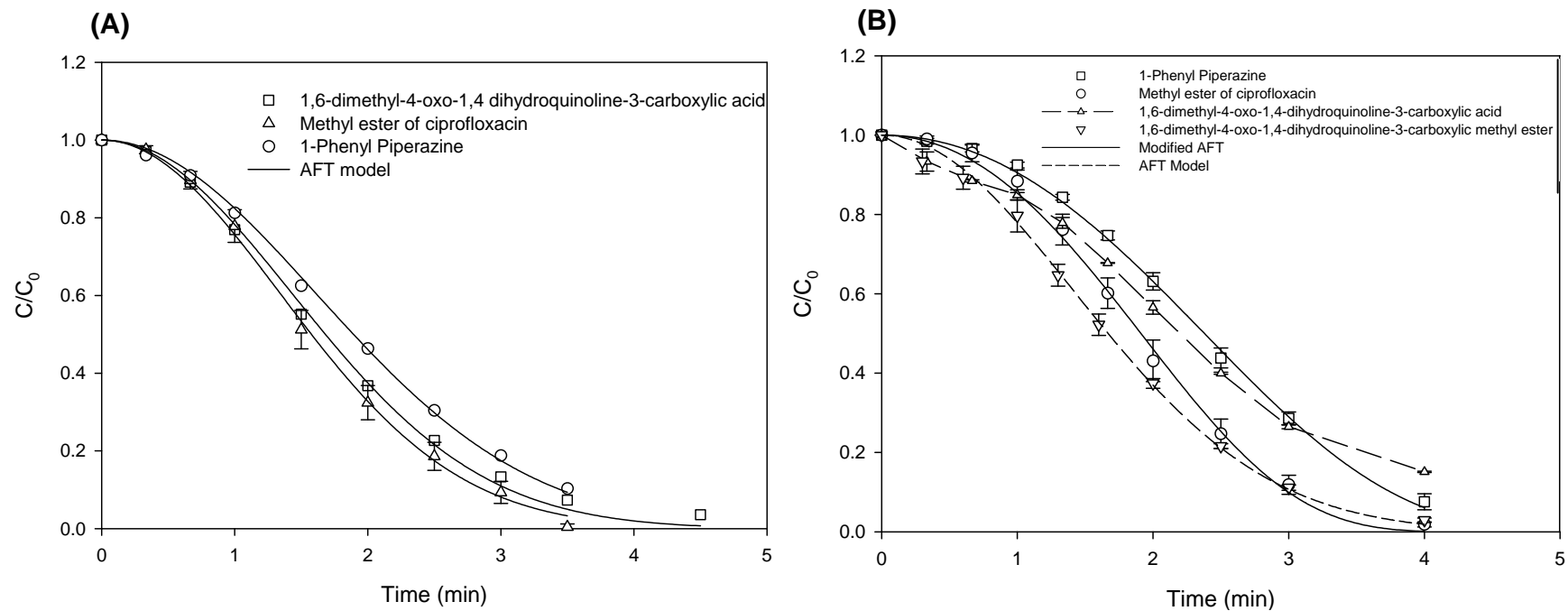


Figure 2.4 Degradation of reference compounds in AFT system. $[\text{H}_2\text{O}_2]:[\text{Fe}^{2+}]=10:1$, **(A)** Current delivery = 0.04A, pH = 3.2, $[\text{PP}]_0 = [\text{QA}]_0 = [\text{CIPM}]_0 = 55\mu\text{M}$. **(B)** Current delivery = 0.03A, pH = 6.2-6.8, $[\text{H}_2\text{O}_2]:[\text{Fe}^{2+}] = 10:1$, $[\text{PP}]_0 = [\text{QA}]_0 = [\text{CIPM}]_0 = [\text{QAM}]_0 = 55\mu\text{M}$.

The results indicate that the carboxylic acid group may play a key role in the kinetics of degradation, because absence of this functional group (as in PP) and methylation of CIP gave different degradation patterns. In contrast, QA, a structural analog with a free carboxylic acid, followed a degradation pattern similar to that of CIP. To further confirm the role of the carboxylic acid on the quinolone structure, QA was esterified and degraded by AFT. The degradation kinetics shifted from a CIP-type curve to a typical AFT curve, further supporting the essential role of the free carboxylic acid group (**Figure 2.4 B**).

In addition to protonation at the acidic pH, the carboxylic acid group may complex with iron easily when it is in a deprotonated form at a higher pH. Thus, two hypotheses were proposed as to how the carboxylic acid group might affect the degradation kinetics: (I) CIP undergoes protonation during the treatment, leading to a change in distribution of CIP species, which have different reactivities with hydroxyl radicals, and the resulting degradation pattern is a hybrid of the two kinetic degradation patterns, one from each species; (II) CIP may complex with iron at near neutral initial pH and this complex formation may affect either the Fenton reaction or the CIP reaction affinity toward the OH radical, resulting in a shift in kinetics during the first minute.

CIP protonation/deprotonation effect on degradation. A buffer system at neutral pH, which assists in maintaining CIP speciation, cannot be used in the AFT system due to strong interference with the Fenton reaction. In order to test the first hypothesis of speciation-dependent reactivity of CIP with hydroxyl radicals due to protonation, DFT calculations of potential energies during the reaction were carried out. Since the change in kinetics took place during the first minute, it was assumed that the first major reaction determined the kinetic pattern. Based on the mass spectrometric data of the CIP degradation products, the first reaction is hydroxyl addition to the aromatic ring. Therefore, the potential energy surface profiles of CIP, the

hydroxyl radical, and 5-hydroxylated CIP were calculated and are shown in **Figure 2.5**. For the deprotonated CIP and OH radical, a lower transition state energy was found compared to that of protonated CIP, with a significant energy difference of 26.16 kJ mol⁻¹ for the transition states. An observable difference in reaction rates is expected, supporting our first hypothesis, that the difference in reaction affinity of the different CIP species with hydroxyl radicals is an explanation for the kinetic degradation pattern. This result is consistent with the hydroxyl radical being a strong electrophile with greater affinity for and reactivity with the neutral deprotonated CIP than the positively charged protonated CIP.

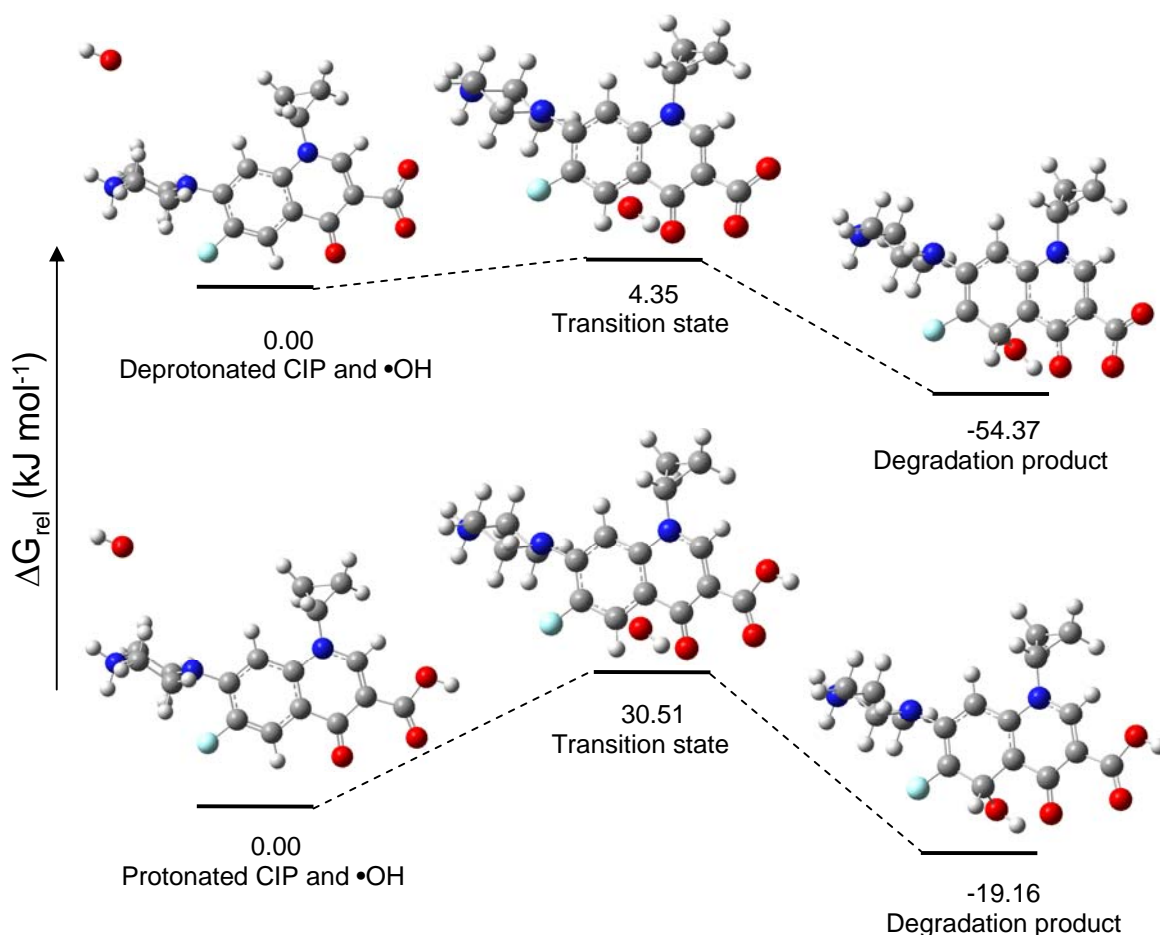


Figure 2.5 Calculated potential energy surface profiles for reaction between deprotonated and protonated CIP with hydroxyl radical by Gaussian 03 (B3LYP/6-31G).

CIP-metal complex effect on degradation. Another possible cause for the change in kinetics is the complexation between CIP, a carboxylate Lewis base, and iron, a strong Lewis acid. Various studies have shown the formation of CIP-metal complexes, most likely in a bidentate mode via the 3-carboxylate and 4-carbonyl groups (12, 13). The complex formation between metal ions and fluoroquinolones depends on pH due to the competition between polyvalent ions and protons (14).

To investigate the complex formation hypothesis, AFT was carried out on a CIP-Al complex and a CIP-Fe complex (**Figure 2.6A**). Since Al has a CIP binding affinity similar to ferric ion, pre-addition of excess Al ion before AFT should cause the formation of a CIP-Al complex and minimize CIP-ferric complexation. Degradation data of the CIP-Al complex at pH 6.2-6.8 overlapped with that of CIP during the first minute, indicating a negligible effect of this complex on the Fenton reaction. There is a slower degradation of CIP-Al after 1.5 minute with the remainder of the degradation pattern appearing to follow a first-order curve. This phenomenon might be due to the buffering capacity of $\text{Al}(\text{OH})_4^-$ at the starting pH, thus preventing a shift to the ideal, lower pH for Fenton systems and a consequent slowing of the reaction (**Figure 2.6B**) (15). The pH buffering effect of humic acid that slows degradation has been observed in a previous study where a similar first-order like curve was found (16).

To further test how complex formation affects reaction affinity of CIP toward the hydroxyl radical, AFT was run in a system with pre-addition of excess ferric ion, thus causing formation of a CIP-ferric complex before AFT treatment. If the complex has a major effect on the reaction affinity of CIP, we would expect to see a change in the degradation curve, especially during the first minute because this is the critical period when ferric ion accumulates (from oxidation of ferrous ion) and begins to bind with CIP. Interestingly, a degradation pattern similar to that of

CIP was observed, indicating no effect of excess ferric ion on CIP degradation (**Figure 2.7A**).

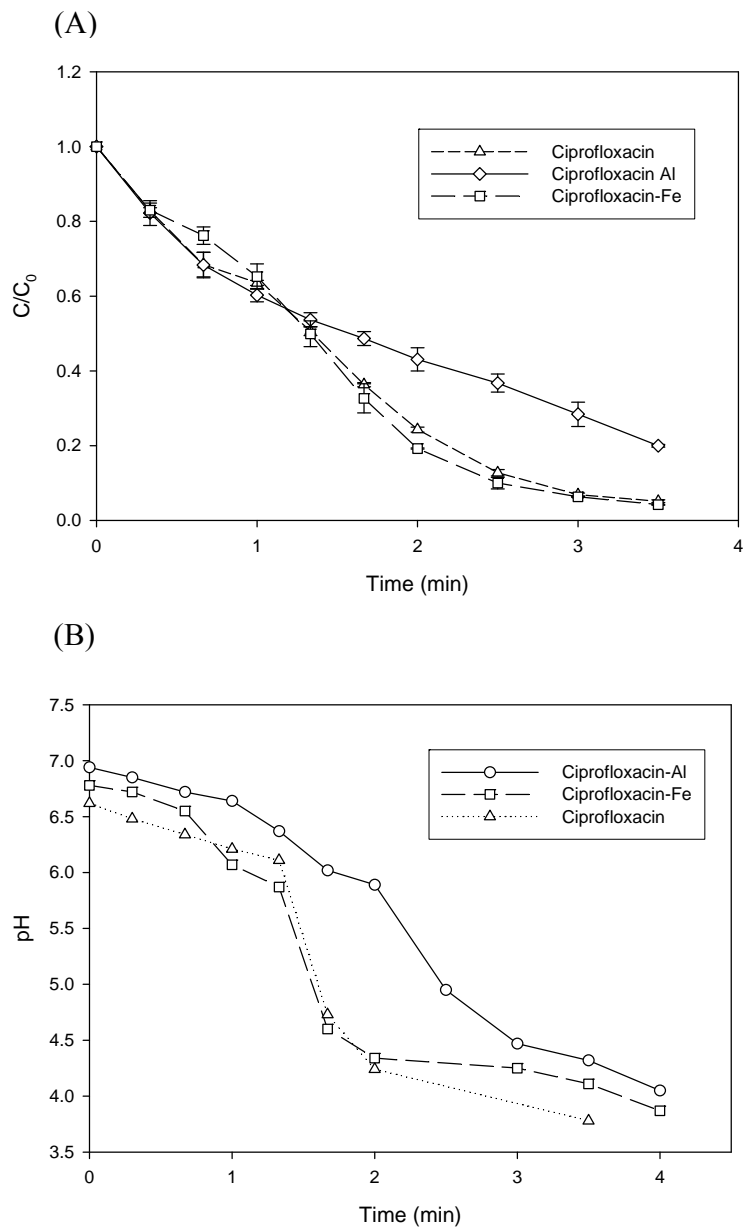


Figure 2.6 (A) Degradation of CIP and CIP-Metal complex in AFT system; **(B)** pH profiles during degradation of ciprofloxacin and ciprofloxacin-metal complex in AFT system; Current delivery = 0.04A; $[H_2O_2]:[Fe^{2+}] = 10:1$; $[CIP]_0, [CIP-Al]_0, [CIP-Fe]_0 = 55 \mu M$, initial pH 6.2-6.8;

Based on the degradation kinetics of both the CIP-metal complexes, it can be concluded that the complex formation with metal ion is too weak to cause effects, if any, on the degradation kinetics. Therefore the observed kinetics are caused by protonation/ deprotonation, generating two species of CIP that react differently with OH radicals.

Development of the AFT' model. A model based on the protonation/ deprotonation hypothesis (the AFT' model) was developed that accounts for the change of species distribution during degradation. The goal was not to develop a generalized model but to simulate the CIP degradation in the AFT system. Successful model fitting further provides a confirmation of the hypothesis.

The pH was monitored throughout the degradation (**Figure 2.7A**), and a distribution of CIP species was calculated according to the following acid-base equilibrium and Henderson-Hasselbalch Equation.



$$\frac{[Ciprofloxacin]}{[HCiprofloxacin^+]} = \frac{10^{-pka}}{10^{-pH}} = Ratio \quad (6)$$

$$Ciprofloxacin\% = \frac{Ciprofloxacin}{Ciprofloxacin + HCiprofloxacin^+} * 100\% = \frac{Ratio}{Ratio + 1} \quad (7)$$

Species distribution curves were obtained by plotting the percentage of deprotonated CIP as a function of time (**Figure 2.7B**). Of several mathematical models tried, the Gaussian model provided the best fit for the distribution curves ($R^2 > 0.98$). This function can be represented by

$$CIP \% = a + c * \exp(-b * t^2), \quad (8)$$

where t is reaction time, and a, b, and c are coefficients used in the Gaussian Model.

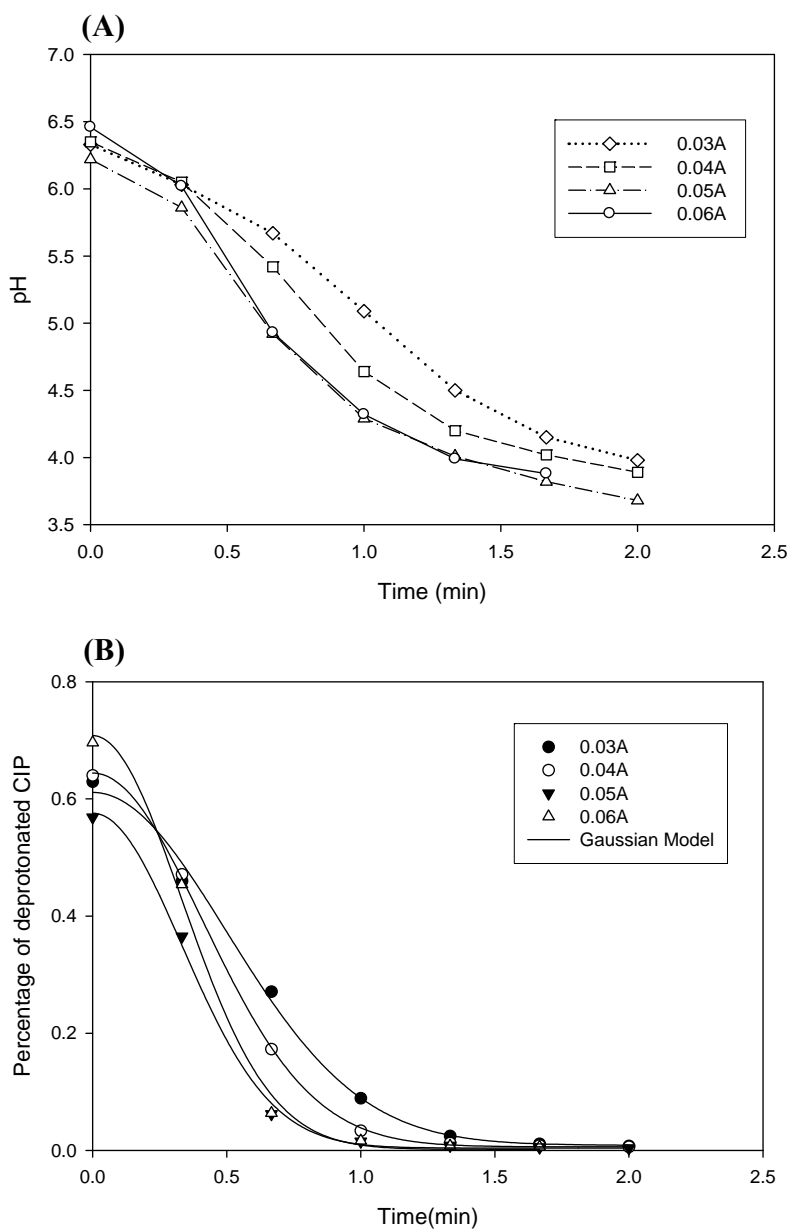


Figure 2.7 (A) pH profiles during Ciprofloxacin degradation in AFT system, with current delivery rates from 0.03-0.06 A. **(B)** Deprotonated Ciprofloxacin percentage during AFT process at different current delivery rates $[H_2O_2]/[Fe^{2+}] = 10:1$, $[Ciprofloxacin]_0 = 55 \mu M$, $pH = 6.5-6.8$.

Assuming each species has a different reaction rate with the hydroxyl radical and each species follows the AFT model, i.e., both the Fenton reaction and the reaction between the CIP species

and hydroxyl radicals follow second order kinetics, a new model can be derived, which we call the AFT' model, the derivation process is shown below:

$$\frac{dc}{dt} = k_1 * [OH\cdot] * [Ciprofloxacin] + k_2 * [OH\cdot] * [HCiprofloxacin^+] \quad (9)$$

$$Ciprofloxacin\% = a + c * \exp(-b * t^2) \quad (10)$$

$$[HCiprofloxacin^+] = (1 - Ciprofloxacin\%) * c \quad (11)$$

$$-\frac{dc}{dt} = Kk_1' * t * (a + c * \exp(-b * t^2)) * [c] + Kk_2' * t * (1 - a - c * \exp(-b * t^2)) * [c] \quad (12)$$

$$\frac{C}{C_0} = \exp\left(\frac{-Kk_1'}{2} * (a * x^2 - \frac{c}{b} * \exp(-b * x^2))\right) - \frac{Kk_2'}{2} * \left(\frac{c}{b} * \exp(-b * x^2) - (a - 1)x^2\right) - \frac{c}{b} * \left(\frac{Kk_2'}{2} - \frac{Kk_1'}{2}\right) \quad (13)$$

$$where K = k\lambda\pi\omega v_0^2,$$

k_1' and k_2' are the second order reaction rate constants of deprotonated and protonated CIP with hydroxyl radicals, respectively.

To test the validity of the AFT' model, concentration profiles of CIP degradation at various currents (iron delivery rates) at initial pH 6.2-6.8 were fitted (**Figure 2.8A**). Compared to the previous AFT model ($R^2 \sim 0.9$), the AFT' model showed a major improvement in describing the kinetics ($R^2 > 0.97$, **Figure 2.8B**). The AFT' model worked best for degradation at the higher Fenton reagent delivery rates ($\geq 0.04A$). At lower delivery rates, the model cannot capture the changes of CIP concentration well in the first few seconds. This observation may indicate a larger error in estimating distribution of CIP species at lower iron deliveries or other complicating factors that may need to be taken into consideration.

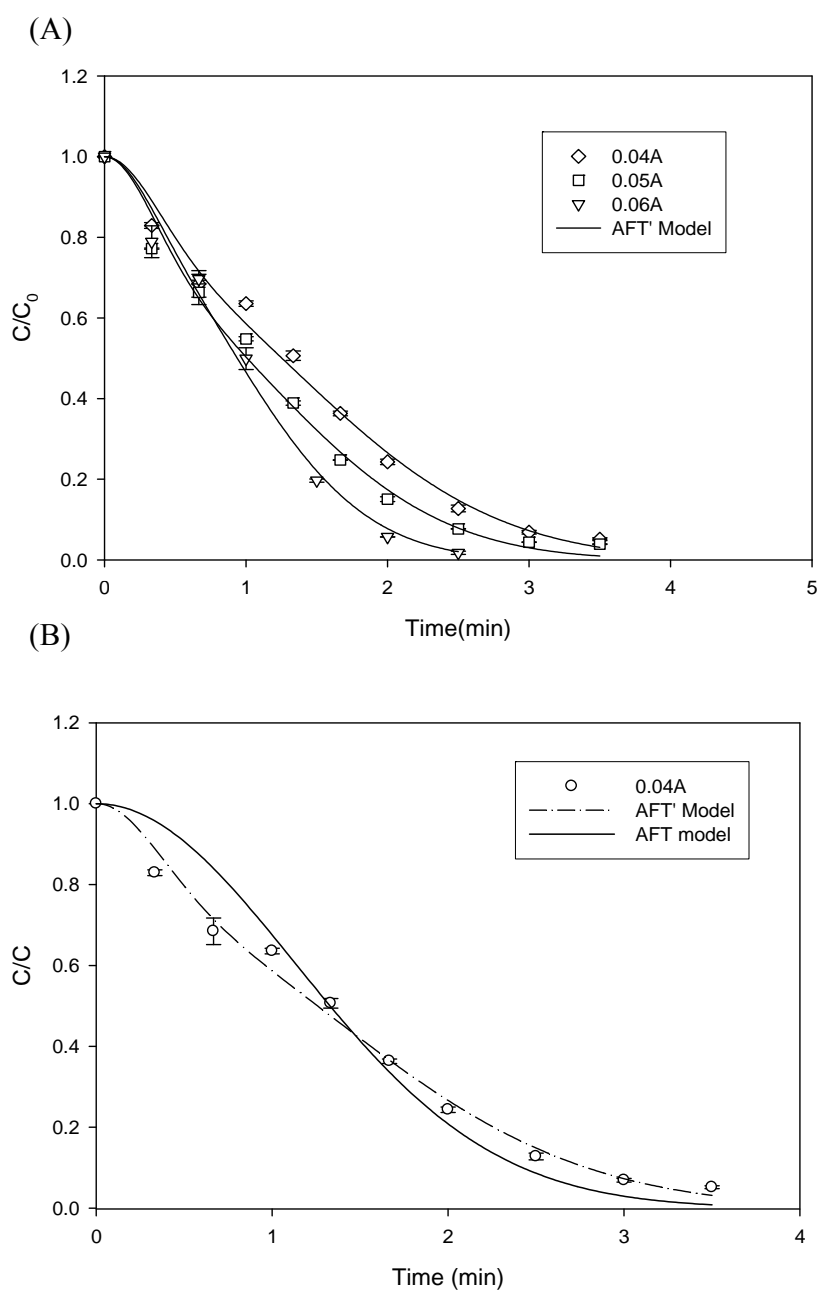


Figure 2.8 (A) Degradation of CIP with current delivery = 0.04A-0.06; $[\text{H}_2\text{O}_2]:[\text{Fe}^{2+}] = 10:1$; initial pH = 6.2-6.8; $[\text{CIP}]_0 = 55 \mu\text{M}$. The data were fit by the AFT' model. **(B)** Comparison of AFT model and AFT' model by fitting degradation data at current delivery = 0.04A.

Optimization of CIP degradation. The experimental conditions of CIP degradation by AFT were optimized at pH 3.2. A series of experiments were carried out with various Fenton reagent

delivery rates, $\text{H}_2\text{O}_2:\text{Fe}^{2+}$ ratios, and initial CIP concentrations (Figure 2.9, Figure 2.10).

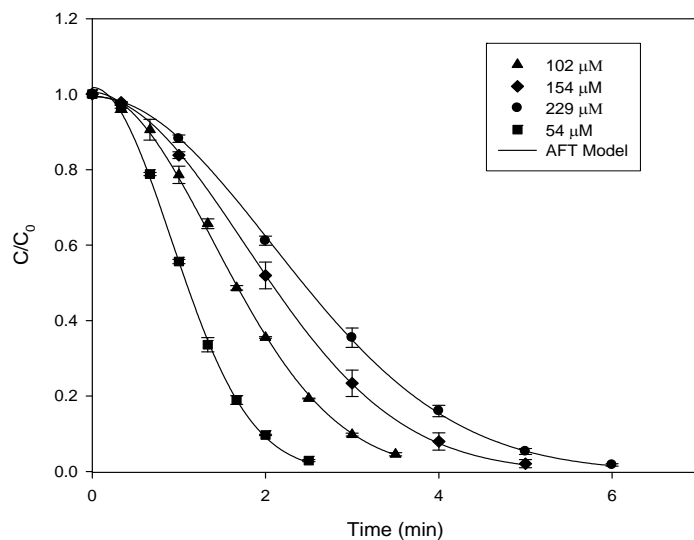


Figure 2.9 Degradation of Ciprofloxacin under different current delivery rates at $\text{pH} = 3.2$.

$[\text{H}_2\text{O}_2]:[\text{Fe}^{2+}] = 10:1$, $[\text{Ciprofloxacin}]_0 = 55 \mu\text{M}$

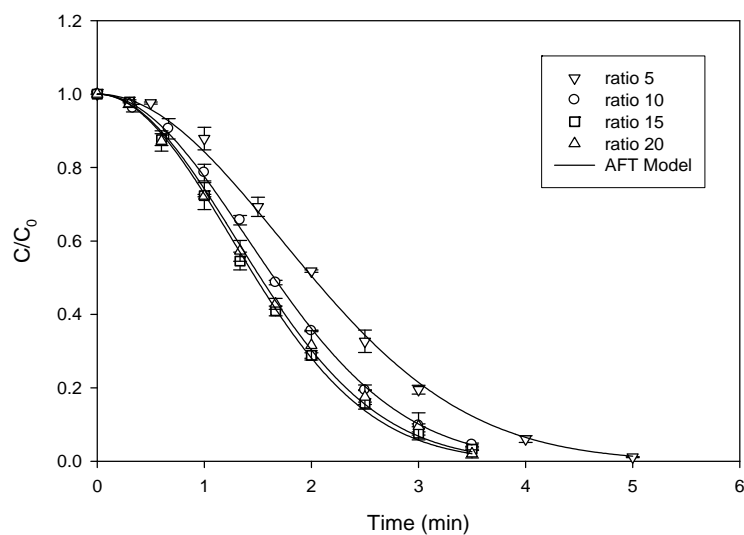


Figure 2.10 Degradation of Ciprofloxacin at current delivery = 0.04 A with different $[\text{H}_2\text{O}_2]:[\text{Fe}^{2+}]$ ratios, $[\text{Ciprofloxacin}]_0 = 55 \mu\text{M}$.

All degradation kinetics followed the AFT model. The degradation rate was faster with increased Fenton reagent delivery rates, where a faster generation of hydroxyl radicals would be expected, and slower with increased initial CIP concentration. Due to hydroxyl radical quenching by iron and hydrogen peroxide, the ratio of ferrous ion to hydrogen peroxide is seldom stoichiometric. An optimal ratio between 10 and 15 was found, consistent with previous results that showed an optimal ratio of 11 (**Figure 2.10**) (9).

Identification of CIP degradation products and proposed pathways. In order to understand the degradation pathways of CIP, degradation products obtained at two initial pH conditions were identified by HPLC-MS. Representative chromatograms are shown in **Appendix A**.

Degradation mixtures at 2.5 minutes at both conditions were chosen for analysis due to the relatively high concentrations of major products. The products were identified by the $[M+H]^+$ ion in the positive mode. Four major products with molecular ions of m/z 348, 362, 330, 263 were found at both pHs, although slight differences in degradation pattern were observed. A trace amount of m/z 334 was seen at neutral condition while a much higher concentration of m/z 334 was detected at acidic condition. This observation may indicate a species-dependent preference in pathways. In addition, a different pathway may occur with a neutral initial pH because the product m/z 328 was detected only at this condition. Several minor products were also observed at both pH conditions, including m/z 291, m/z 304, m/z 302, and m/z 261. Due to their low concentrations, it is hard to determine if the degradation products were preferentially formed at a given pH. The fragmentation patterns of products were also compared with those reported in the literature. Several similar products have been found in previous studies where CIP was oxidized by various methods (17-19).

The mass spectrum profiles of the peaks are summarized in **Table 2.1** and proposed pathways

are shown in **Figure 2.11**. Most product profiles show peaks at a mass increase of 22 Da and a mass loss of 18 Da, corresponding to the ions $[M-H+Na]^+$ and $[M-H_2O]^+$, respectively.

The aromatic ring of CIP has been observed to be a susceptible site for hydroxylation (19, 20); thus, m/z 348 is believed to be the product of such hydroxylation. The reaction can take place at C-5 or C-8. Under the LC conditions used, the two products cannot be separated efficiently, and a mixture is expected. The observed fast formation of m/z 348 supports hydroxyl addition on the aromatic ring, a well known fast reaction (20).

Table 2.1 Mass spectrum profiles of peaks for CIP degradation intermediates.

Pseudo-molecular Ion($M+H^+$)	Mass difference	Mass spectrum profile	Retention Time(min)	Observed reaction system pH
332	0	354(29), 332(83), 314(32), 288(1.2) (CIP)	9.46	-----
263	-69	285(13), 263(39), 245(100)	13.49	Both
348	16	370(31), 348(54), 330(85),	9.01	Both
330	-2	352(33), 330(65), 312(24),	8.22	Both
304	-28	326(4), 304(15), 286(14)	7.619	Both
302	-30	302(16)	7.811	Both
362	30	384(61), 362(100), 344(51),	8.53	Both
334(1)	2	356(26), 334(64), 316(57)	8.73	Mainly Acidic
334(2)	2	356(17), 334(78), 316(41)	12.34	Mainly Acidic
291	-41	291(20), 273(56)	13.063	Acidic
328	-4	350(11), 328(69), 310(32)	8.682	Neutral

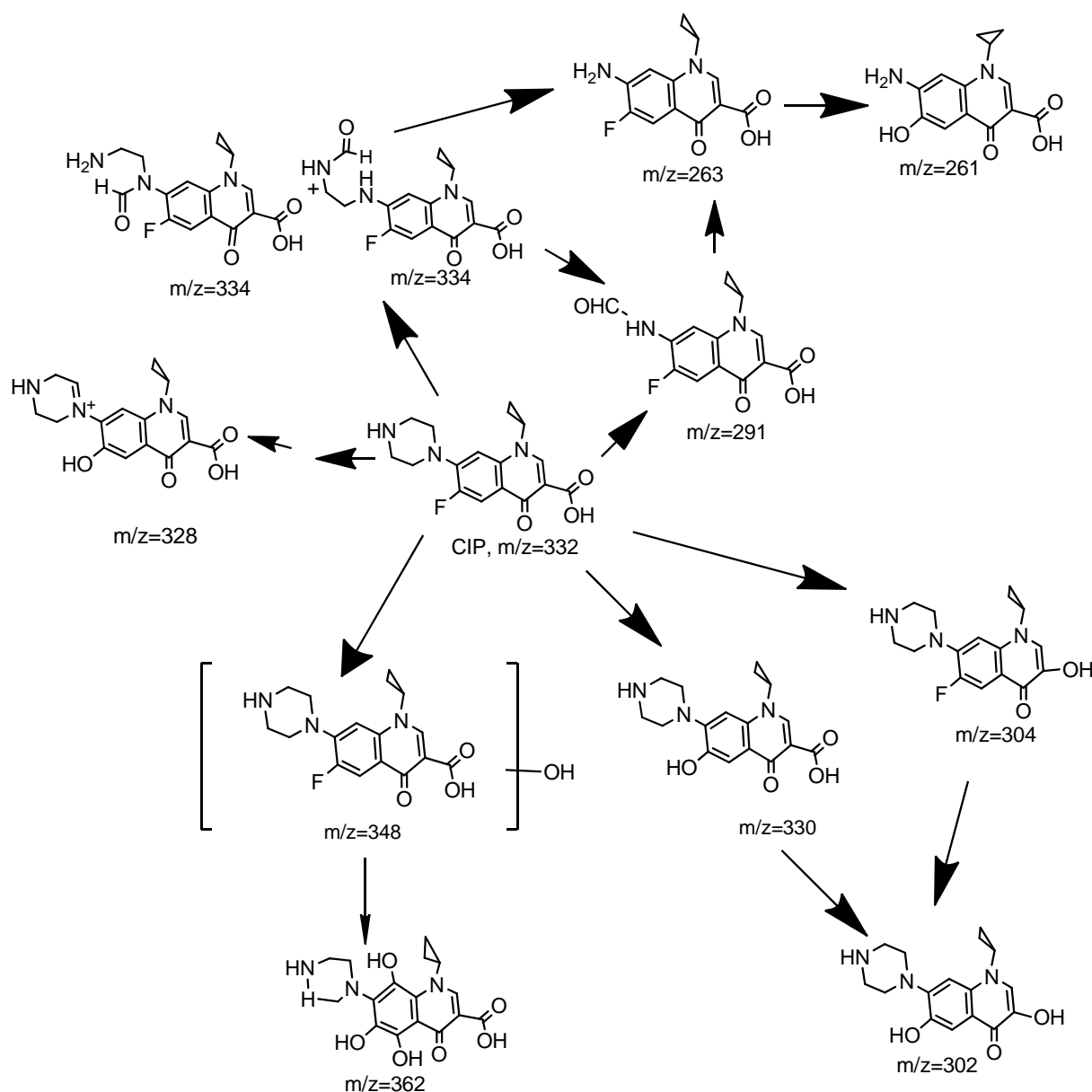


Figure 2.11 Proposed degradation pathways of CIP in the AFT system

Another well known degradation pathway is defluorination (11, 19, 20). During defluorination, the attack of the hydroxyl radical at the carbon-fluorine position leads to a geminal fluorohydrin intermediate that undergoes HF elimination. The m/z 330 product is consistent with this pathway. Multiple hydroxylation is also likely to happen which may explain

the formation of m/z 362. Its relatively late formation time also supports this multiple step reaction pathway (**Figure 2.12**).

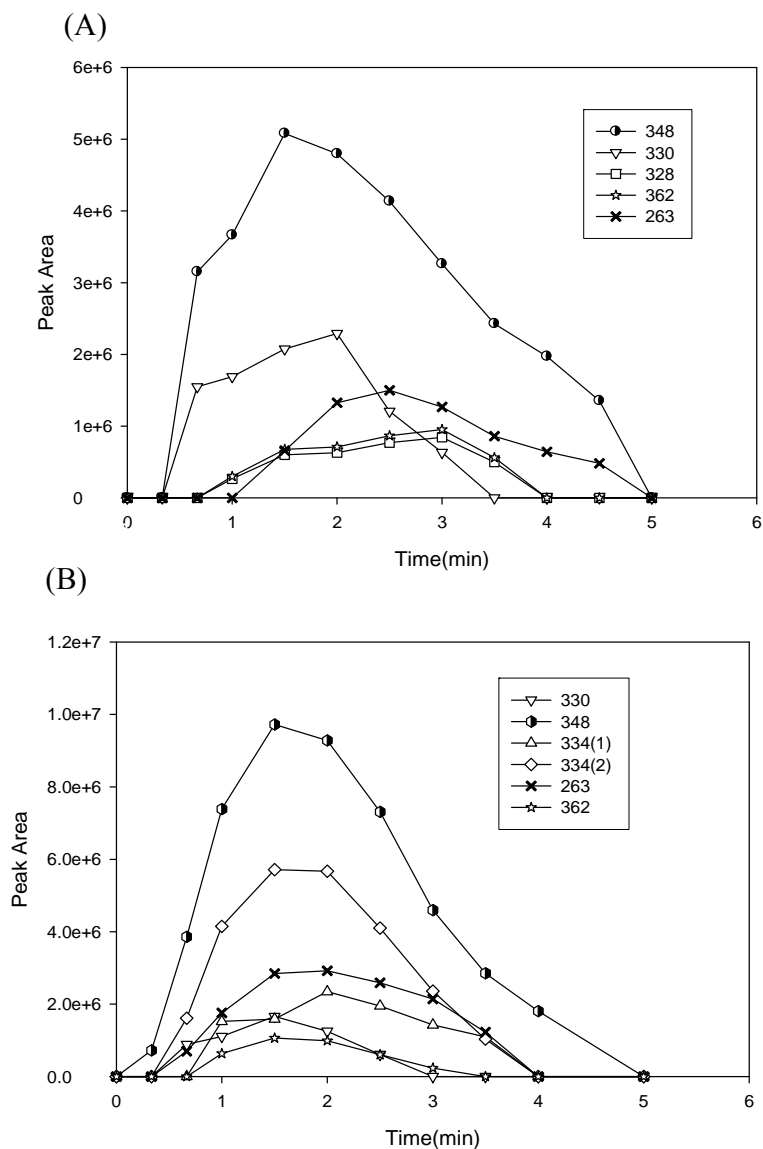


Figure 2.12 Evolution of CIP degradation products. Current delivery = 0.04A; $[H_2O_2]:[Fe^{2+}] = 10:1$; $[CIP] = 55 \mu M$. **(A)** Initial pH = 6.2-6.8; **(B)** initial pH = 3.2.

Previous studies on CIP degradation suggest that the piperazinyl substituent is a likely susceptible site to hydroxyl radical attack (11, 18, 19). The m/z 263 species is believed to form

via the complete dealkylation of the piperazine ring. A trace amount of m/z 261 was also observed. This compound may be formed via a similar pathway to that of m/z 263, except for a further defluorination step. The m/z 263 and 261 species were the final products observed which is consistent with their late formation time (**Figure 2.12**). Intermediates of dealkylation reported in other studies, such as desethylene CIP, were not observed. This result may be due to a short half-life or very low concentration of the intermediates in AFT. The m/z 334 and m/z 291 species are believed to be derived from oxidation of the piperazine ring of CIP and are upstream products of m/z 263. Two m/z 334 isomers were observed with a large difference in LC retention time. This may be explained by the different polarities of the secondary and tertiary amines.

The m/z 328 species has not been reported before. It may be formed by OH radical attack at both the piperazine ring and the C-6 of the quinolone ring, resulting in a C-N double bond formation in the piperazine ring and defluorination on the quinolone core (22). Oxidative decarboxylation is also a likely mechanism for degradation of CIP although it occurs to a lesser extent. This pathway may account for the trace amounts of m/z 302 and m/z 304 observed.

It is believed that destruction of piperazinyl substituents only partially remove the antibiotic activity of CIP (23). Also, most of the modifications on the quinolone ring observed here cannot alter the antibiotic properties to a great extent since the structures still share considerable similarity to CIP (24). In addition, the antibiotic properties of m/z 328 are not well understood. Therefore, we monitored the CIP reaction mixtures during the entire process to study the evolution of the products (only primary products are shown in **Figure 2.12**). All the peak areas show an increase in area (qualitatively correlated with concentration) followed by a general trend toward decrease in area at 3-5 minutes. By the end of the treatment, not only was CIP completely removed, but the degradation products were degraded to below the LC-MS detection limit,

indicating successful removal of antibacterial intermediates.

References

1. Dodd, M. C.; Shah, A. D.; Gunten, U. V.; Huang, U. C-H. Interactions of fluoroquinolone antibacterial agents with aqueous chlorine: reaction kinetics, mechanisms, and transformation pathways. *Environ. Sci. Technol.* **2005**, 39, 7065-7076.
2. Picó, Y.; Vicente, A. Fluoroquiolones in soil-risks and challenges. *Anal. Bioanal. Chem.* **2007**, 387, 1287-1299.
3. Gu, C.; Karthikeyan, K. G. Sorption of antimicrobial CIP to aluminum and iron hydrous oxides. *Environ. Sci. Technol.* **2005**, 39, 9166–9173.
4. Torniainen, K.; Tammilehto, S.; Ulvi, V. The effect of pH, buffer type and drug concentration on the photodegradation of CIP. *Int. J. Pharm.* **1996**, 132, 53-61.
5. Dodd, M. C.; Buffle, M. O.; Gunten, U. V. Oxidation of antibacterial molecules by aqueous ozone: moiety-specific reaction kinetics and application to ozone-based wastewater treatment. *Environ. Sci. Technol.* **2006**, 40, 1969-1977.
6. Kolpin, D. W.; Furlong, E. T.; Meyer, M. T.; Thurman, E. M.; Zaugg, S. D.; Barber, L. B.; Buxton, H. T. Pharmaceuticals, hormones, and other organic wastewater contaminants in U. S. Streams, 1999-2000: a national reconnaissance. *Environ. Sci. Technol.* **2002**, 36, 1201-1211.
7. Gros, M.; Petrovic, M.; Barcelo, D. Tracing pharmaceutical residues of different therapeutic classes in environmental waters by using liquid chromatography/quadrupole-linear ion trap mass spectrometry and automated library searching. *Anal. Chem.* **2009**, 81, 898-912.
8. Larsson, D. G.; De Pedro, C.; Paxeus, N. Effluent from drug manufactures contains extremely high levels of pharmaceuticals. *J. Hazard. Mater.* **2007**, 148, 751–755.
9. Wang, Q.; Lemley, A. T. Kinetic model and optimization of 2, 4-D degradation by anodic

- Fenton treatment. *Environ. Sci. Technol.* **2001**, 35, 4509-4514.
10. Neafsey, K.; Zeng, X.; Lemley, A. T. Degradation of sulfonamides in aqueous solution by membrane anodic Fenton treatment. *J. Agric. Food Chem.* **2010**, 58, 1068-1076.
11. Dewitte, B.; Dewulf, J.; Demeestere, K.; Vyvere, V.; Wispelaere, P.; Langenhove, H. Ozonation of CIP in water: HRMS identification of reaction products and pathways. *Environ. Sci. Technol.* **2008**, 42, 4889-4895.
12. Trivedi, P.; Vasudevan, D. Spectroscopic investigation of CIP speciation at the goethite-water interface. *Environ. Sci. Technol.* **2007**, 41, 3153-3158.
13. Djurdjević, P., Stankov, M. J., Odović, J. Study of solution equilibria between iron(III) ion and CIP in pure nitrate ionic medium and micellar medium. *Polyhedron.* **2000**, 19, 1085-1096.
14. Walls, S. C.; Charles, B. G.; Gahan, L. R.; Filippich, L. J.; Bredhauer, M. G.; Duckworth, P. A. Interaction of norfloxacin with divalent and trivalent pharmaceutical cations. In vitro complexation and in vivo pharmacokinetic studies in the dog. *J. Pharm. Sci.* **1996**, 85, 803-809.
15. Pignatello, J. J. Advanced oxidation processes for organic contaminant destruction based on the Fenton reaction and related chemistry. *Environ. Sci. Technol.* **2006**, 36, 1-84.
16. Wang, Q. Q.; Lemley, A. T. Kinetic effect of humic acid on Alachlor degradation by anodic Fenton treatment. *J. Environ. Qual.* **2004**, 33, 2343-2352.
17. Calza, P.; Medana, C.; Carbone, F.; Giancotti, V.; Baiocchi, C. Characterization of intermediate compounds formed upon photoinduced degradation of quinolones by high-performance liquid chromatography/high resolution multiple-stage mass spectrometry. *Rapid Commun. Mass Spectrom.* **2008**, 22, 1533-1552.
18. Zhang, H. C.; Huang, C. H. Oxidative transformation of fluoroquinolone antibacterial agents and structurally related amines by manganese oxide. *Environ. Sci. Technol.* **2005**, 39, 4474-4483.

19. Wetzstein, H. G.; Stadler, M.; Tichy, H. V.; Dalhoff, A.; Karl, W. Degradation of CIP by basidiomycetes and identification metabolites generated by the brown rot fungus *Gloeophyllum striatum*. *Appl. Environ. Microbiol.* **1999**, *65*, 1556-1563.
20. Santoke, H.; Song, W.; Cooper, W. J.; Greaves, J.; Miller, G. E. Free-radical-induced oxidative and reductive degradation of fluoroquinolone pharmaceuticals: kinetic studies and degradation mechanism. *J. Phys. Chem. A.* **2009**, *113*, 7846-7851.
21. Wetzstein, H.; Schneider, J.; Karl, W. Patterns of metabolites produced from the fluoroquinolone enrofloxacin by basidiomycetes indigenous to agricultural sites, *Appl. Microbiol. Biotechnol.* **2006**, *71*, 90-100.
22. Surdhar, P. S.; Armstrong, D. A. Reactions of α -carbon- and nitrogen-centered radicals of piperazine with lumiflavin and paranitroacetophenone at pH 7. *Can. J. Chem.* **1988**, *66*, 535-540.
23. Vasconcelos, T. G.; Henriques, D. M.; König, A.; Martins, A. F.; Kümmerer, K. Photo-degradation of the antimicrobial CIP at high pH: identification and biodegradability assessment of the primary by-products. *Chemosphere.* **2009**, *76*, 487-493.
24. Jjemba, P.; Robertson, B. Antimicrobial agents with improved clinical efficacy versus their persistence in the environment: synthetic 4-quinolone as an example. *Ecohealth.* **2005**, *2*, 171-182.

CHAPTER 3

DEGRADATION OF CIPROFLOXACIN BY CRYPTOMELANE-TYPE MANGANESE(III/IV) OXIDES

Xiao Xiao[†], Sheng-Peng Sun[†], Murray B. McBride[‡], and Ann T. Lemley[†]

[†]Graduate Field of Environmental Toxicology, FSAD, HEB, Cornell University

[‡]Department of Soil and Crop Science, Cornell University

Ithaca, New York 14853-4401

Abstract

The objective of this study is to investigate and understand the oxidizing properties of a manganese oxide, specifically synthetic cryptomelane ($\text{KMn}_8\text{O}_{16}$) and its derivatives, in aqueous solution. Ciprofloxacin (CIP), a commonly used fluoroquinolone antibiotic was used as the probe. Synthetic cryptomelane, known as octahedral molecular sieves (OMS-2), was synthesized, and its derivatives were prepared by adding transition metal oxides, V_2O_5 or MoO_3 , as dopants during synthesis. The solids were characterized by XRD, SEM-EDX, XPS, FTIR, Raman and N_2 -BET. Degradation of CIP by different doped OMS-2 was carried out. Process conditions were optimized using response surface methodology (RSM). XRD patterns indicated the crystal phase of regular and doped OMS-2 as the cryptomelane type. Presence of the dopants in doped cryptomelane was confirmed by SEM-EDX and XPS. FTIR and Raman results suggested that the dopants were substituted into the framework in place of manganese. SEM images, XRD analysis, and surface area analysis of doped OMS-2 indicated decreased particle size, decreased crystallinity and increased surface area compared to regular OMS-2. Higher oxidizing reactivity of doped OMS-2 was also observed with increased CIP removal rates from aqueous solution. The enhancement of reactivity may be due to the increase of surface areas. 9% Mo/OMS-2, the most effective oxidant of all synthesized derivatives, was selected for optimization study. Favorable treatment conditions were obtained using RSM at pH 3 with molar ratio [9% Mo/OMS-2]:[CIP] ≥ 50 . Under such conditions, more than 90% CIP can be removed in 30 minutes. The degradation kinetics was modeled by a modified first order rate with introduction of a retardation factor α ($R^2 > 0.98$). Analysis of degradation products indicated that oxidation takes place mainly on the piperazine ring of CIP.

Introduction

Manganese (III/IV) oxides are naturally occurring minerals that are widely distributed in surface water, sediment and soil. With their abundance in the environment, they are potential oxidizing agents of natural and xenobiotic compounds. Oxidative transformation of a variety of natural organics and xenobiotics, such as phenols and amines, by manganese (III/IV) oxides has been reported (1-6). Recognized as an important participant in environmental oxidation-reduction reactions, manganese (III/IV) oxides have a potential for water treatment application.

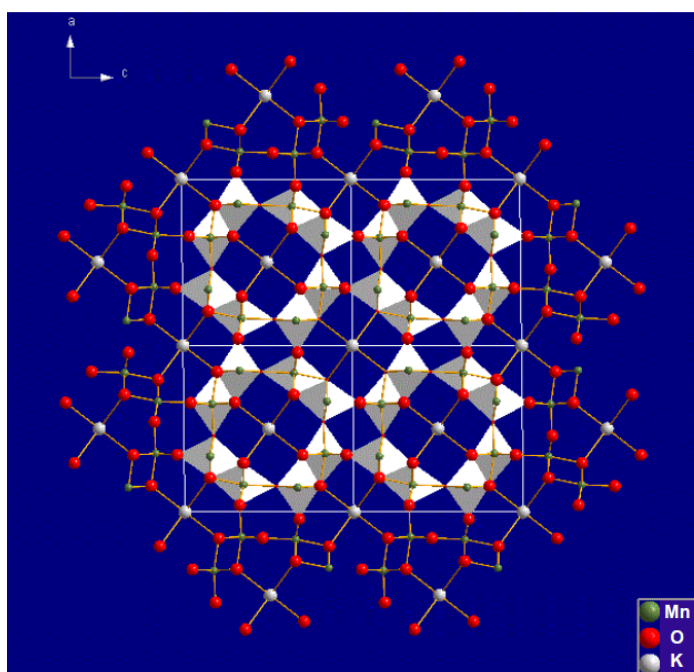


Figure 3.1 Crystal structure of cryptomelane

Cryptomelane is a type of manganese (III/IV) oxide with a 2×2 tunnel structure formed by edge and corner sharing of MnO_6 octahedral units (**Figure 3.1**). Potassium ions are situated in the tunnel of cryptomelane to balance the charge of the manganese oxide framework. The synthetic counterpart of cryptomelane is known as octahedral molecular sieve OMS-2, where “2” denotes the dimension of the tunnel size. Good catalytic activity of OMS-2 has been reported, and its synthesis, characterization and application have recently

gained considerable research interest (7-10). Doping cryptomelane with foreign metals changes its electronic, structural and catalytic properties and enhancement of activity has been achieved (8, 11-12). The metal dopants can either enter the tunnel and replace some of the potassium ions or be substituted into the framework of OMS-2 and replace the manganese. The coordination and crystal radii of the dopant cations determine where the doping occurs (8, 13).

Fluoroquinolones are a group of potent antibiotics and have been used widely in human and veterinary medicine. Like most pharmaceuticals, they are not completely metabolized in the body and can be released into the environment. Detection of fluoroquinolones has been reported in wastewater effluent in the range of $\mu\text{g/l}$ and surface water in the range of ng/L (14-15). Fluoroquinolones share great similarity in their structures and modes of reaction and may have additive effects on untargeted organisms, resulting in increased environmental risk. In addition, adverse effects of fluoroquinolones at environmentally relevant concentrations have been reported in toxicity studies (16-17). Therefore, effective treatment methods for fluoroquinolones need to be explored. In this study, ciprofloxacin (CIP), a commonly used second generation fluoroquinolone antibiotic, was selected as the probe.

The objectives of this study are to: evaluate the effectiveness of synthetic cryptomelane and its doped derivatives for CIP removal from aqueous solution; determine the effects of doping on structure and morphology of cryptomelane type manganese oxides; optimize treatment conditions using central composite design (CCD) and response surface methodology (RSM); model the kinetic process and propose the degradation pathways of CIP.

Materials and methods

Chemicals. All reagents were used without further purification. Ciprofloxacin (CIP) (98%) was purchased from Sigma-Aldrich Chemicals (Milwaukee, WI). 1, 6-dimethyl-4-oxo-1,4-dihydroquinoline-3-carboxylic acid (QA) (>95%) was purchased from Chembridge Corp

(San Diego, CA). Manganese sulfate monohydrate, vanadium pentoxide, molybdenum trioxide, potassium permanganate, and nitric acid (63%) were purchased from Fisher Scientific. All solutions were prepared from distilled deionized (DDI) water.

Synthesis of OMS-2 and doped OMS-2. Cryptomelane (OMS-2) was synthesized by refluxing potassium permanganate (KMnO_4) and manganese sulfate (MnSO_4) in the presence of nitric acid in aqueous solution for 24h (18). For doped cryptomelanes, similar procedures were used except that 3% and 6% (V:Mn molar ratio) vanadium pentoxide and 3%, 6% and 9% (Mo:Mn molar ratio) molybdenum trioxide were added to the mixture. Doped cryptomelanes were denoted as V/OMS-2 or Mo/OMS-2. The obtained solids were washed with distilled and deionized (DDI) water, dried at 120°C overnight and ground in an agate mortar.

Characterization of OMS-2 and doped OMS-2. The X-ray powder diffraction (XRD) spectra were collected with a Scintag Theta Theta X-ray diffractometer equipped with $\text{Cu K}\alpha$ radiation ($\lambda=1.5418 \text{ \AA}$). The scanning angles (2θ) ranged from 1.5° to 60° , with a 0.02° step size and a collecting time of 0.24s per point.

Morphological studies were carried out using a field emission scanning electron microscope (LEO 1550 FESEM). The surface chemical composition was analyzed by both x-ray photoelectron spectroscopy (XPS) and energy dispersive spectrometry (EDX). XPS spectra were recorded at room temperature with an aluminum anode for $\text{K}\alpha$ radiation (Model SSX-100). The instrument is calibrated to Au $4f_{7/2}$ peak at 84eV. A wide scan ranging from 0-1000eV was obtained for surface chemical composition analysis. Mn $3s$ spectra were collected at narrower scan ranges for valence information. All data were analyzed by CasaXPS v2.3.15.

The Brunauer-Emmett-Teller (BET) surface area measurements were carried out using a micromeritics ASAP 2010. Prior to the analysis, the samples were degassed at 120°C for 12h.

Fourier-transform infrared spectra (FTIR) were recorded on a Mattson Galaxy 5020 FTIR spectrometer in the range of 4000 - 400 cm^{-1} with a resolution of 4 cm^{-1} for samples in KBr pellets at room temperature. Raman spectra were obtained using a Renishaw inVia confocal Raman microscope with an Ar^+ laser (488nm).

Batch experiments of CIP degradation. Degradation of CIP by regular and doped OMS-2 was investigated. In a 50 ml aluminum foil covered conical tube, the desired amount of manganese oxides was added to 40ml of CIP solution. The suspension was constantly shaken at room temperature, and the solution pH was adjusted to the desired value before each reaction. One-milliliter samples were taken at desired time intervals, and 0.1ml 1N ascorbic acid was added to the sample to dissolve manganese oxides and quench the reaction. The total amount of CIP in the system was measured as aqueous CIP + adsorbed CIP.

The concentration of CIP was analyzed by a reverse phase high performance liquid chromatography (HPLC) with a diode array UV-Vis detector (HP series 1200, Agilent) and a Restek ultra C18 (5 μm) reverse phase column (4.6 \times 150 mm) thermostated at 30°C. 0.1ml of 1N H_3PO_4 was added to each sample to stabilize CIP (Zhang and Huang 2005). The detector wavelength was set at 278 nm. Gradient elution was used with the mobile phase containing 0.1% formic acid (eluent A) and acetonitrile (eluent B). The eluent A/eluent B ratio was changed from 95:5 to 85:15 over 1 min, and then to 72:28 over 3 min, and to 0:100 over 14min, and from 0:100 back to 95:5 over 2 min.

Degradation products were analyzed by HPLC-UV/MS. The HPLC condition for degradation products separation was the same as that of CIP analysis. The degradation products were found to have similar UV spectra to that of CIP. Therefore the concentration of degradation products was monitored at the same UV wavelength as that of CIP. For MS spectral analysis, a different quenching method, filtration by a 0.22 μm nylon filter, was used for sample preparation due to the limitation of MS instrumentation. Filtration may lead to

fewer by-products detected due to the adsorption of by-products on the solid surface. The MS spectra were obtained using an Agilent G1978B Multimode source for the 6100 series single-quadrupole MS in the positive ES mode with a full scan from m/z 50 to m/z 700 and a fragmentor of 180. The specific parameters set up for the mass detector was as follows: drying gas flow, 12 L min^{-1} ; nebulizer pressure, 40 Psig; drying gas temperature, $300 \text{ }^\circ\text{C}$; vaporizer temperature, $250 \text{ }^\circ\text{C}$; capillary voltage, 2000 V; corona current, $4.0 \text{ } \mu\text{A}$; and charging voltage, 2000 V.

Release of Mn^{II} into aqueous solution was measured by atomic absorption spectrometry (Buck Scientific 210 VGP) with air acetylene flame at 279.5 nm.

Process optimization by RSM. The experimental design of CIP degradation by OMS-2 type manganese oxide was carried out using response surface methodology (RSM) coupled with central composite design (CCD). RSM-CCD is a collection of mathematical and statistical techniques that are beneficial for modeling and analyzing a complex system where a response of interest is influenced by several variables. The objective of this method is to search and determine the optimal conditions of variables for the predicted response. In the present study a four-factorial five-level central composite experimental design with six replicas at the center point, resulting in a total number of thirty experiments, was employed for response surface modeling. A further ten experiments were carried out to validate the developed model. The variables (independent factors) used in this study were: initial load of oxidant (X_1), initial pH of CIP solution (X_2), initial concentration of CIP (X_3), and reaction time (X_4). CIP removal efficiency (Y) was considered as the dependent factor (response). The actual values and coded values of the independent factors are shown in **Table 3.1**.

Table 3.1 Variable ranges and values of central composite design for degradation of CIP by OMS-2 type manganese oxides

Process variables	Symbol	Actual Values of the coded variable levels				
		-2	-1	0	1	2
Oxidant (mg/L)	X ₁	50	100	150	200	250
pH	X ₂	3	4	5	6	7
C _{cip} (mg/L)	X ₃	5	10	15	20	25
T (min)	X ₄	15	45	75	105	135

Data analysis. The experimental data were analyzed by using Design-Expert software. The response variable was fitted by an empirical second-order polynomial model in the form given below:

$$Y = b_0 + \sum b_i X_i + \sum b_{ii} X_i^2 + \sum b_{ij} X_i X_j$$

where Y is the predicted response, X_i (i= 1, 2, 3, and 4) are the independent factors and b₀, b_i (i=1, 2, 3 and 4), b_{ii} and b_{ij} (i=1, 2, 3 and 4, j=1, 2, 3 and 4) are the model coefficients, respectively. Two-dimensional contour plots and three-dimensional curves of the response surfaces were developed using the same program. Degradation kinetic data were analyzed and modeled by Sigma Plot software.

Results and Discussion

Characterization of OMS-2 and doped OMS-2. The XRD patterns of OMS-2 and doped OMS-2 are shown in **Figure 3.2**. The diffraction peaks of OMS-2 (curve a) can be indexed to reported data of cryptomelane (JCPDS 44-1386). All doped OMS-2 samples showed similar diffraction patterns to that of OMS-2, and no additional peaks attributed to vanadium or molybdenum species were found. This implies that only the cryptomelane type crystal phase was formed. With increased doping amount, the intensity of the peaks decreased and the peak

width broadened. Such observations indicate the loss of long range order, reduced crystallinity and decreased particulate sizes.

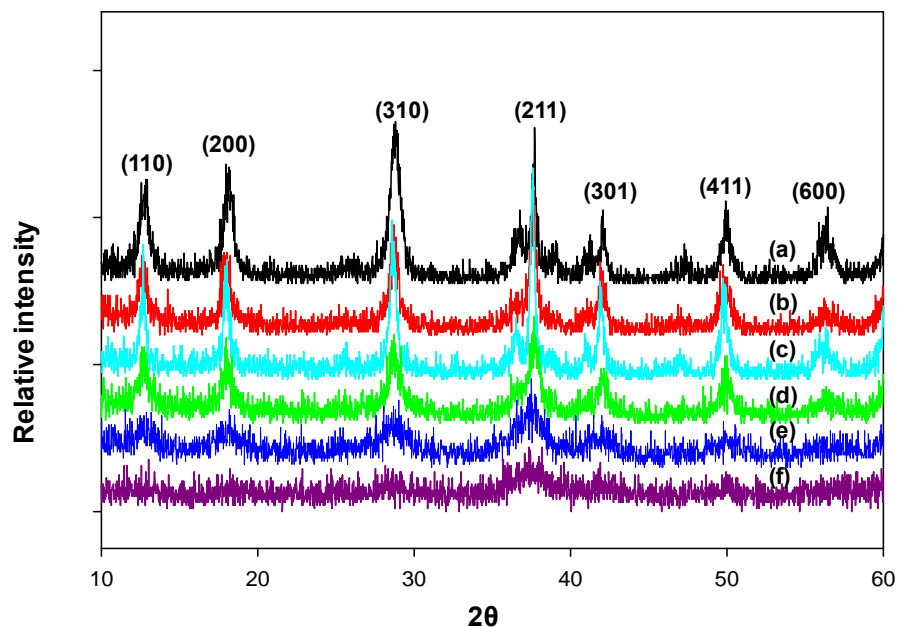


Figure 3.2 XRD patterns of regular and doped OMS-2: (a) OMS-2; (b) 3% V/OMS-2; (c) 6% V/OMS-2; (d) 3% Mo/OMS-2; (e) 6% Mo/OMS-2; (f) 9% Mo/OMS-2.

SEM micrographs of OMS-2 and doped OMS-2 are shown in **Figure 3.3**. OMS-2 has a fibrous morphology, with a fiber diameter of 50-100 nm and fiber length of a few micrometers (19). Upon doping, manganese oxide particles lose their distinct needle shape morphology and the formation of pseudo-flakes is observed. Similar morphology has been reported for multi-doped manganese oxides (13). The inhibitory effects of doping on the nanofiber length are due to distortion of octahedral units after V/Mo substitution and subsequent introduction of defects (20-21). Aggregations of both fibrous and flaky particles were observed to form microspheres with an average diameter of 0.2-2 μm (**Figure 3.3**).

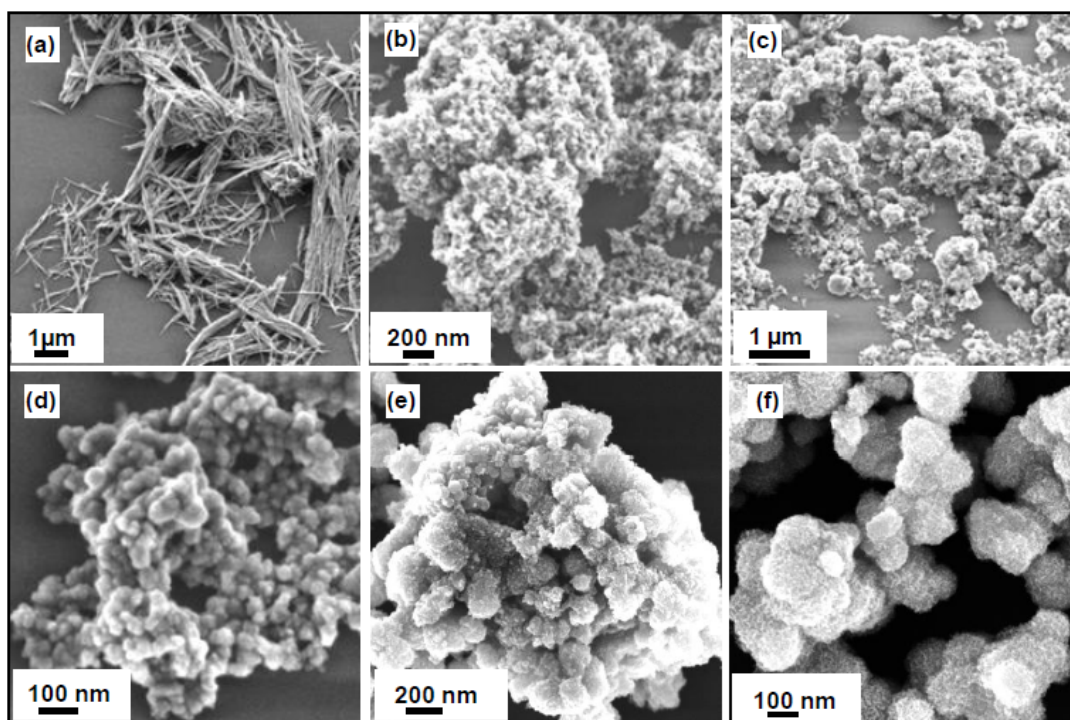
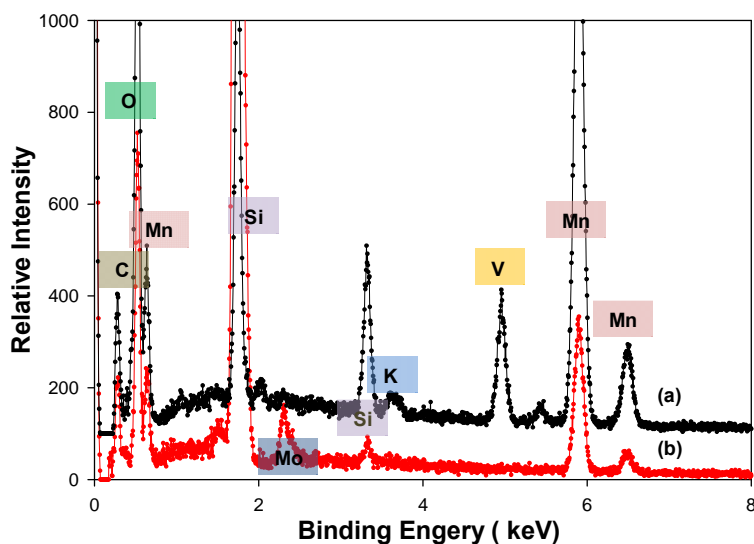


Figure 3.3 SEM images of regular and doped OMS-2: (a) OMS-2; (b) 3% V/OMS-2; (c) 6% V/OMS-2; (d) 3% Mo/OMS-2; (e) 6% Mo/OMS-2; (f) 9% Mo/OMS-2.

The surface areas were measured by the N₂-BET method (**Table 3.2**). OMS-2 has a moderate surface area of 70.5 m²/g. The lowest percentage doping with Mo (3%) does not have much effect on surface area. However, the same percentage doping with V resulted in an increase in surface area, from 70.5 to 101.4 m²/g. A further increase in surface area was observed with higher percentage doping of either Mo or V ($\geq 6\%$). For instance, 6% Mo doping gave a surface area 3.6 times larger than that of undoped OMS-2. Such high surface areas are consistent with the previously observed phenomenon that high-valent metal (V^V/Mo^{VI}) doping can increase surface areas effectively (13).

Table 3.2 Surface characterization of regular and doped OMS-2

Sample	Surface Area (m ² /g)	Std Error	Dopant (M/Mn)	Mn 3s Splitting (ev)
OMS-2	70.51	0.71	--	5.1845
3% V/OMS-2	101.45	0.9	3.1%	5.1473
6% V/OMS-2	180.97	1.9	8.3%	5.1302
3% Mo/OMS-2	74.33	0.74	6.4%	5.1751
6% Mo/OMS-2	232.51	4.56	12.5%	5.1972
9% Mo/OMS-2	285.92	3.32	16.6%	5.1672

**Figure 3.4** Representative energy dispersive X-ray spectra of doped OMS-2: (a) 6%V/OMS-2; (b) 9% Mo/OMS-2; The silicon signal is from the Si substrate.

Elemental composition analysis by EDX confirmed the presence of V and Mo (**Figure 3.4**). The ratios of dopants to Mn were quantified by XPS (**Table 3.2**). Since XPS is a surface characterization tool, the results only indicate surface conditions. As shown in **Table 3.2**, the ratio of dopants/Mn increased with the increase of doping percentage. It is noteworthy that the dopant/Mn ratios on the surface are larger than the corresponding values in reaction mixtures, implying that more dopants are situated on the surface than in the bulk. A study by

others on vanadium doped cryptomelane also found more vanadium cations present on the surface than in the bulk phase (21).

Oxidation states of manganese were analyzed by the energy splitting of Mn3s spectra (**Table 3.2, Appendix B**). For Mn^{IV}, an energy splitting at 4.6-4.7ev is expected, and for Mn^{III}, an energy splitting of ~5.3ev is expected (22-23). Energy splittings observed for regular and doped OMS-2 ranged from 5.13-5.2ev. Thus Mn oxidation states of all OMS-2 type manganese oxides are primarily in the Mn^{III} form. Presence of dopants during synthesis does not seem to cause a shift in Mn^{III}/Mn^{IV} composition in doped OMS-2 samples.

Due to the similar crystal radii of six coordinated V^V and Mo^{VI} ions with that of Mn^{IV}/Mn^{III}, these two dopants are expected to enter the framework of OMS-2 (13). To understand the doping process, IR and Raman spectra were collected to provide complementary structural information to XRD results through vibrational spectroscopy.

FTIR spectra are shown in **Figure 3.5 A**. OMS-2 shows spectral features similar to those reported in the literature, with vibrational peaks close to 470 cm⁻¹, 530 cm⁻¹, and 720 cm⁻¹ (13, 24). Upon doping, the position and intensity of peaks changed. The spectral change for 3%V/OMS-2 is relatively subtle, with a shoulder peak occurring at 580 cm⁻¹. More distinct changes were observed for all other doped OMS-2 samples. The peaks at 470 cm⁻¹, 530 cm⁻¹ in OMS-2 shifted to higher frequency and the intensity of the 720cm⁻¹ peak decreased. Meanwhile, there is a small peak at 930 cm⁻¹ for molybdenum doping and at 980 cm⁻¹ for vanadium doping. The intensity of these two peaks becomes stronger with increased doping amount. The two peaks are proposed to correspond to the Mo-O and V-O stretching modes respectively (25-26). Bands corresponding to V=O stretching modes at 1020cm⁻¹ and the Mo=O stretching mode at 990 cm⁻¹ are expected if out-of-framework vanadium or molybdenum species are present (**Appendix C**). However, no peaks were found at these positions. The above observations indicate that the dopants were substituted into the

framework of the manganese oxides, leading to a change in the local environment of the oxygen coordinating around the octahedral sites and subsequently to a change in the vibrational patterns observed.

Figure 3.5B shows the Raman spectra of all OMS-2 samples. The Raman spectrum of OMS-2 is characterized by two sharp peaks at 570 cm^{-1} and 640 cm^{-1} , indicating a well-developed tetragonal structure with (2×2) tunnels (19). The Mo/OMS-2 spectra exhibit features similar to that of OMS-2 with a peak positioned at $\sim 640\text{ cm}^{-1}$. In addition, no other peaks that match crystalline or amorphous molybdenum trioxide are observed (**Appendix C**). For vanadium doped cryptomelane, an additional peak at 840 cm^{-1} occurs, which can be assigned to the V-O vibrational band (13, 27). Absence of a terminal V=O vibrational band is consistent with the framework substitution hypothesis (**Appendix C**) (28). Based on the FTIR and Raman results, the dopants are believed to have been well dispersed into the framework of OMS-2.

It is expected that the degradation to be studied will take place on the surface of the OMS-2 oxides. Since the dopants are well dispersed in the framework and are higher on the surface than in the initial reaction mixture, as discussed above, it was concluded that this set of results gives the important characterization necessary for the proposed study of CIP degradation in this system.

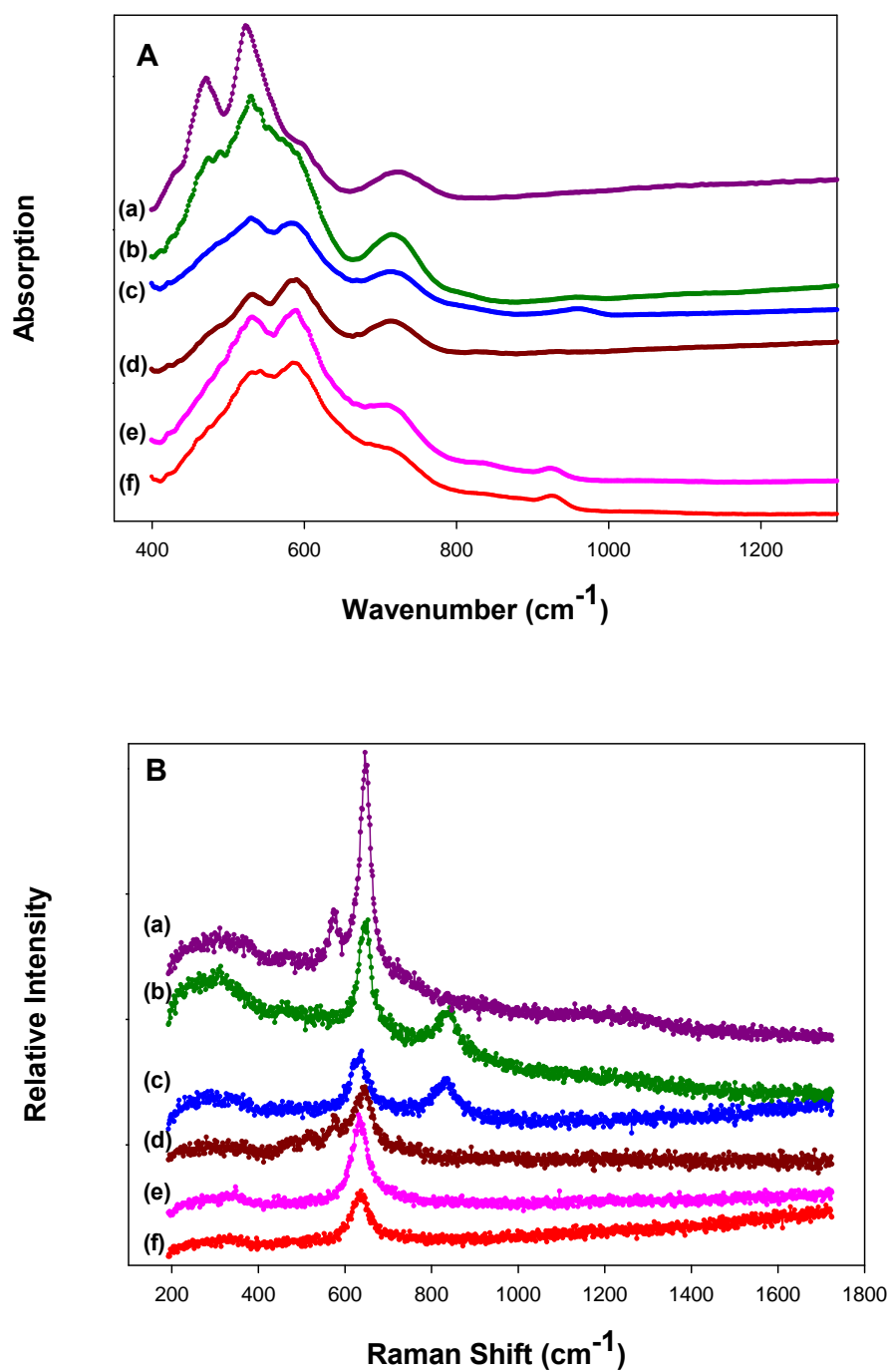


Figure 3.5 A IR and B Raman spectra of regular and doped OMS-2: (a) OMS-2; (b) 3% V/OMS-2; (c) 6% V/OMS-2; (d) 3% Mo/OMS-2; (e) 6% Mo/OMS-2; (f) 9% Mo/OMS-2

CIP degradation by different doped OMS-2. The oxidative reactivity of the OMS-2 type oxides was studied by comparing their ability to remove CIP from aqueous solution. The degradation curves are shown in Figure 5A. OMS-2 is not an effective oxidant, with only 10% degradation achieved after 200 minutes. Relatively low oxidative activity of cryptomelane has been reported previously in comparison studies of different manganese(III/IV) (hydro)oxides (29 - 30). Doping with either 3% Mo or V gave limited improvement to the reaction rates. However, upon 6% doping, reaction rates increased significantly, with the 6% Mo/OMS-2 removing CIP faster than the 6% V/OMS-2 (**Figure 3.6A**). This improvement is consistent with the larger surface area of 6% Mo/OMS-2 (**Table 3.2**). In a following study, the effects of doping percentages of the molybdenum trioxide were examined (**Figure 3.6B**). Degradation rates increased as doping percentage increased up to 9%; 12% doping did not give any further improvement (data not shown). Therefore 9% Mo/OMS-2 was selected as the oxidant to be studied.

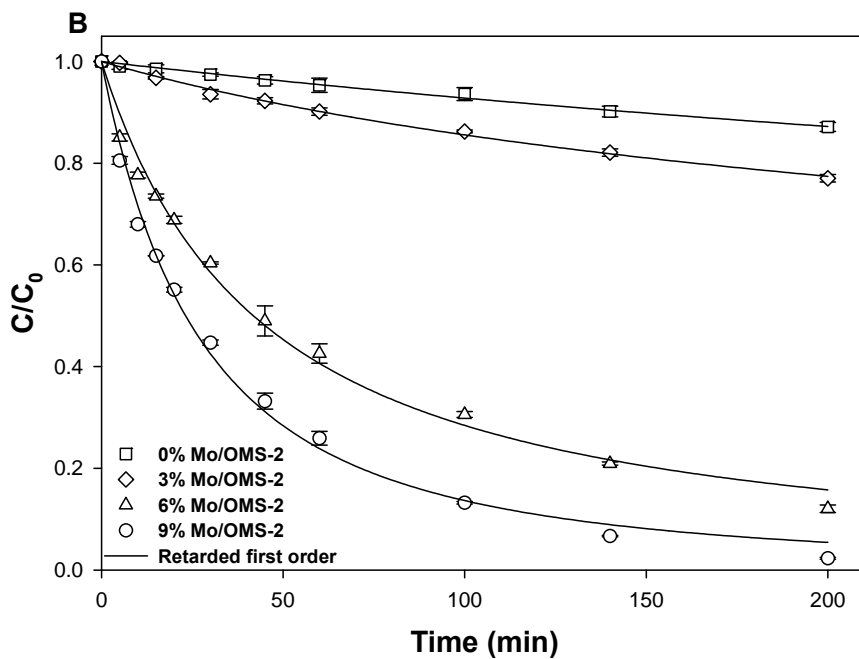
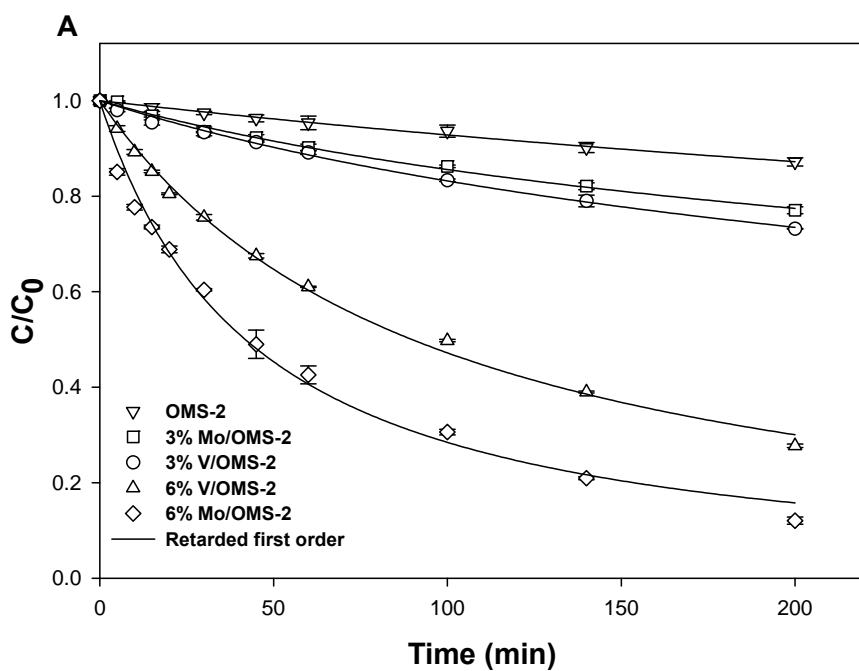


Figure 3.6 **A** Degradation of CIP by different doped OMS-2; **B** Degradation of CIP by Mo/OMS-2 with different Mo doping amount, $C_{cip} = 50\mu\text{M}$, $[M/OMS-2] = 0.1\text{g/L}$, $\text{pH}=3.0$.

Optimization of CIP degradation by 9% Mo/OMS-2. A central composite design coupled with response surface methodology was used for the optimization study. This statistical approach allowed for studying interactions between different factors in a complex system and obtaining the optimal conditions while greatly reducing the number of experiments. The degradation efficiency of CIP was modeled as the response of four independent factors: initial load of oxidant 9% Mo/OMS-2 (X_1), initial pH of CIP solution (X_2), initial concentration of CIP (X_3), and reaction time (X_4). The form of the empirical second order equation obtained is shown below:

$$Y (\%) = 144.83 + 0.34X_1 - 42.3X_2 - 3.83X_3 + 0.84X_4 - 0.00038X_1^2 + 3.26X_2^2 + 0.091X_3^2 - 0.0031X_4^2 + 0.0076X_1X_2 - 0.0015X_1X_3 - 5E-5X_1X_4 - 0.043X_2X_3 + 0.0049X_2X_4 - 0.0067X_3X_4$$

The statistical analysis for the model is shown in **Table 3.3**. All four factors are significant for the response ($p < 0.0001$), while there are no significant interactions between the factors. Lack of fit analysis is insignificant, indicating that the model is sufficient to describe the treatment process. Validation of the model is further shown in **Figure 3.7**. The predicted degradation efficiency of CIP agrees well with the experimental values, confirming that the model is a robust fit.

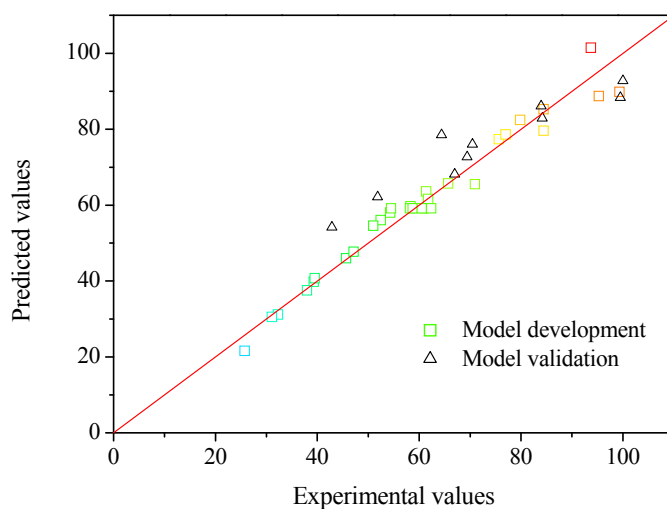


Figure 3.7 Predicted values of CIP removal efficiency versus experimental values.

Table 3.3 ANOVA analysis of the derived response surface model

Source	Sum of Squares	Df	Mean Square	F Value	p-value Prob > F	
Model	10536.02	14	752.57	30.96	< 0.0001	Significant
X ₁ : Oxidant	3519.89	1	3519.89	144.79	< 0.0001	
X ₂ : pH	1868.66	1	1868.66	76.87	< 0.0001	
X ₃ : C _{cip}	2524.08	1	2524.08	103.83	< 0.0001	
X ₄ : T	1831.38	1	1831.38	75.34	< 0.0001	
X ₁ X ₂	2.33	1	2.33	0.096	0.76	
X ₁ X ₃	2.27	1	2.27	0.093	0.76	
X ₁ X ₄	0.10	1	0.10	0.0041	0.95	
X ₂ X ₃	0.75	1	0.75	0.031	0.86	
X ₂ X ₄	0.34	1	0.34	0.014	0.91	
X ₃ X ₄	15.94	1	15.94	0.66	0.43	
X ₁ ²	24.37	1	24.37	1.00	0.33	
X ₂ ²	291.74	1	291.74	12.00	0.0035	
X ₃ ²	141.29	1	141.29	5.81	0.029	
X ₄ ²	211.80	1	211.80	8.71	0.0099	
Residual	364.64	15	24.31			
Lack of Fit	326.26	10	32.63	4.25	0.062	not significant
Pure Error	38.39	5	7.68			
Cor Total	10900.66	29				

Based on the developed polynomial model, the three dimensional (3D) response surface of degradation efficiency is plotted as a function of two independent factors (**Figure 3.8, Appendix D**). **Figure 3.8A** shows the effects of pH and 9% Mo/OMS-2 dosage on CIP

degradation at a fixed C_{cip} and reaction time. At a fixed oxidant load, pH 3 is always the preferred condition. Even at the lowest oxidant load, more than 60% removal of CIP can be achieved. The observed pH-dependent activity may be due to increased oxidizing potential of 9% Mo/OMS-2 at low pH. The contour is steeper at pH 3-5 and approaches a plateau at pH 5-7. This implies that when pH is larger than 5, the degradation efficiency is not much affected by pH. A positive relation between degradation efficiency and 9% Mo/OMS-2 concentration is also shown in this graph. At a fixed pH, the degradation efficiency increases as the oxidant load increases. Such improvement is more drastic at pH 7 where degradation efficiency increases from ~20% to 75% over the oxidant dosage range studied.

A response surface as a function of C_{cip} and oxidant loads is shown in **Figure 3.8B**. A similar positive relation between degradation efficiency and oxidant load was observed. In addition, the degradation efficiency has a negative relation with CIP initial concentration. At low C_{cip} concentrations, 100% CIP removal can be achieved at high oxidant loads. However, at high C_{cip} concentrations, removal rates can only go up to ~80%, indicating a total consumption of reactive sites. Therefore the minimal oxidant to substrate ratio to achieve acceptable CIP removal rates was determined for optimization purposes. A contour plot of degradation efficiency as a function of C_{cip} and 9% Mo/OMS-2 is shown in **Figure 3.8 C**. As degradation efficiency increases, the slopes of the linear part of the contour become steeper. At removal rates equal to or above 90%, the contours become nearly parallel. 90% removal rate is set as the boundary. A minimal molar ratio of [9% Mo/OMS-2, as MnO_2]:[CIP] at 50 was obtained by calculating the molar ratios along this boundary. Therefore, to treat CIP effectively, the preferred working condition is at pH 3 with an oxidant:substrate ratio equal to or larger than 50.

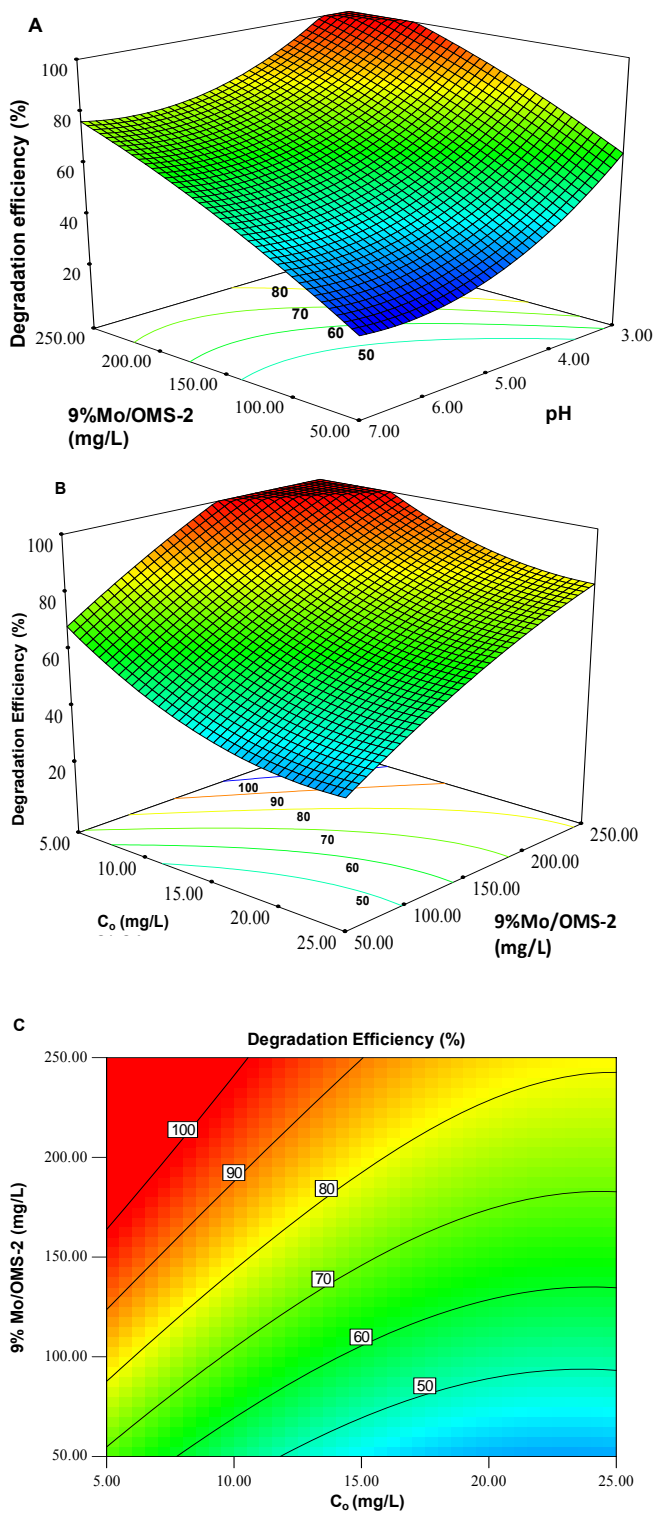


Figure 3.8 **A** Response surface of degradation efficiency as a function of pH and 9% Mo/OMS-2, $C_{cip} = 15\text{mg/L}$, $RT = 75\text{min}$; **B** Response surface of degradation efficiency as a function of C_{cip} and 9% Mo/OMS-2, $\text{pH} = 3$, $RT = 30\text{min}$; **C** Contour plot of degradation efficiency as a function of C_{cip} and 9% Mo/OMS-2, $\text{pH} = 3$, $RT = 30\text{min}$.

Kinetics of CIP degradation by 9% Mo/OMS-2. The kinetic process of CIP degradation was modeled at different pH conditions, with release of Mn^{II} ions monitored by atomic absorption spectrometry (AAS). At pH 3, a pseudo first order model fits the degradation data well. However, at pH 4 and 5.5, the reaction slows down with time and the kinetics change (**Figure 3.9**). Therefore an empirical model with the introduction of a retardation factor α was used to describe the process, as shown below:

$$C = C_0(1+\alpha t)^{-k_{app}/\alpha}$$

where $k_{app} = k/(1+\alpha t)$ and is the apparent rate constant that depends on α , the retardation factor which accounts for all the reasons that cause retardation of the reaction, such as shift of surface reaction sites and competition for reactive sites from by-products formed and from released Mn^{II} during the process (31 - 32) . When $\alpha=0$, the model becomes a first order reaction model. Further validation of the model was carried out with different 9% Mo/OMS-2 loads at each pH condition. All the data were fitted well by the retarded first order model ($R^2 > 0.98$) and obtained apparent rate constants k_{app} are summarized in **Table 3.4**.

Table 3.4 Fitted k_{app} of CIP degradation under various pH conditions and different 9% Mo/OMS-2 dosage, $C_{cip}= 50\mu\text{M}$

9% Mo/OMS-2 (μM)	pH3		pH4		pH5	
	k_{app}	R^2	k_{app}	R^2	k_{app}	R^2
1000	0.0327	0.9894	--	--	--	--
1500	0.0694	0.9934	0.0357	0.9862	0.0261	0.9929
2000	0.101	0.9919	--	--	--	--
2500	0.187	0.9954	0.049	0.9935	0.0468	0.9938
4000	0.419	0.9987	0.0923	0.9915	0.0594	0.9939

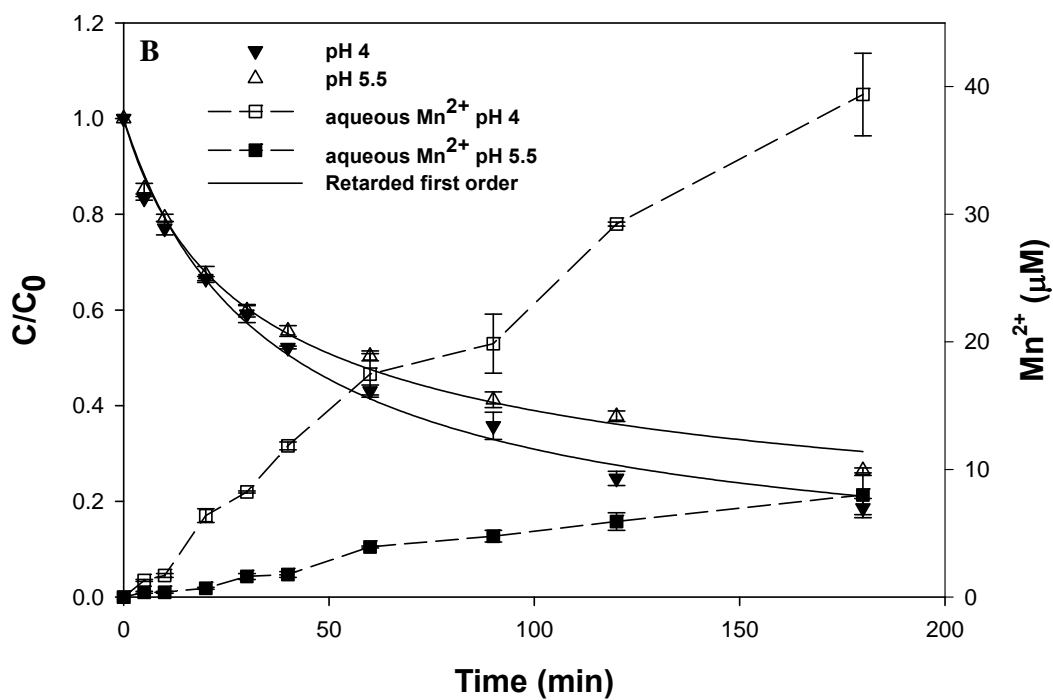
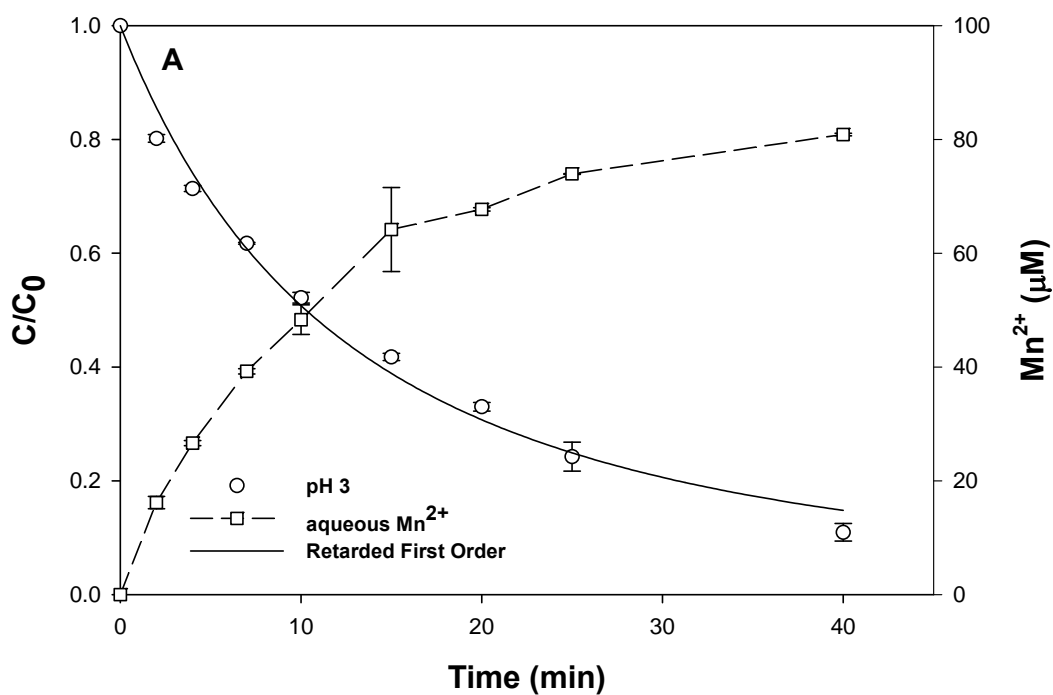


Figure 3.9 Degradation of CIP by 9% Mo/OMS-2 and Mn^{II} release into solution, [9% Mo/OMS-2] = 0.22 g/L, $C_{cip} = 50\mu M$, **A** pH = 3; **B** pH = 4 and 5.5.

Release of Mn^{II} ions into the solution along the reaction is also shown in **Figures 3.9**. Accumulation of aqueous Mn^{II} with time confirms the occurrence of reductive dissolution of the reactive Mn center of the oxide by CIP. In addition, at the same percentage CIP removal, aqueous Mn^{II} concentration is pH dependent: $[\text{Mn}^{\text{II}}]_{\text{pH}=5.5} < [\text{Mn}^{\text{II}}]_{\text{pH}=4} < [\text{Mn}^{\text{II}}]_{\text{pH}=3}$, indicating that adsorption of Mn^{II} heavily depends on pH. Auto-inhibition of redox reactions by Mn^{II} has been observed in the birnessite system (5, 33). To examine the effects of Mn^{II} ions on the degradation process in the OMS-2 system, different amounts of Mn^{II} were added before the reaction, with the experiments carried out at pH 5.5, the high adsorption scenario. Inhibition of the reaction kinetics was observed, but was less severe compared to that in the $\delta\text{-MnO}_2$ system, a commonly used birnessite analog (**Figure 3.10, Table 3.5**) (5, 32). This can be one advantage of Mo/OMS-2 over birnessite in water treatment applications.

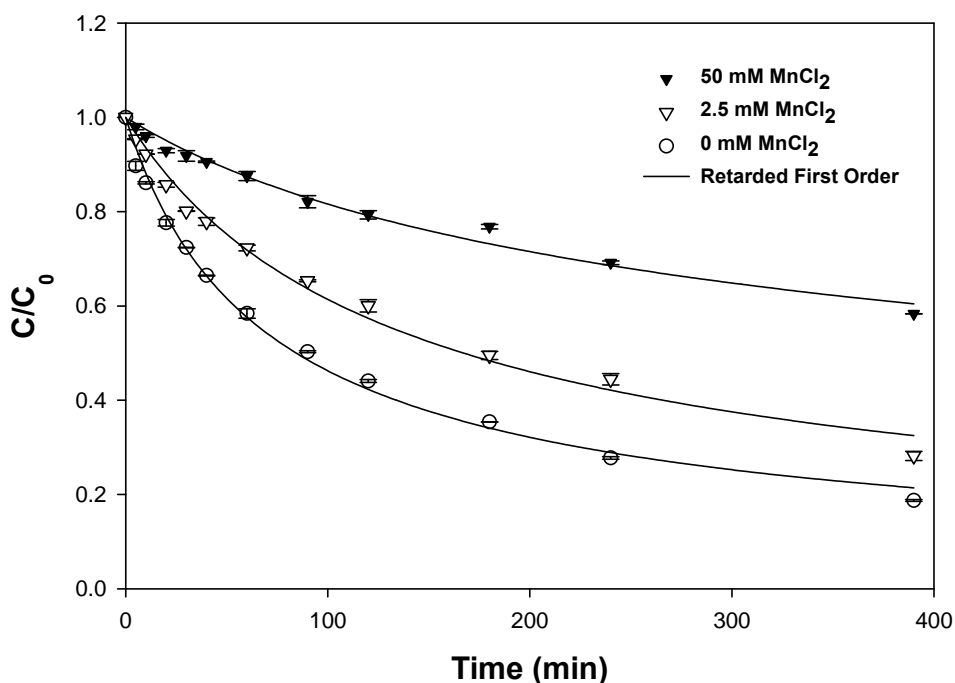


Figure 3.10 Effects of Pre-added Mn^{II} ion on CIP degradation. $[\text{9\%Mo/OMS-2}] = 0.22 \text{ g/L}$, $\text{pH}=5.5$, $C_{\text{cip}} = 50 \text{ }\mu\text{M}$.

Table 3.5 Inhibition of Mn^{II} on oxidative reactivity of manganese(III/IV) oxides

Mn ^{II} /Manganese oxides * (%)	Inhibition of rate constant k _{app} (%)
100 (OMS-2)	62.8
2000 (OMS-2)	78.6
10 (δ -MnO ₂) ^a	69.9
125 (δ -MnO ₂) ^b	100

a: calculated from Zhang and Huang 2003 (3) b: estimated from Lin et al. 2009 (32)

* manganese (II) is added to the reaction at an amount of % of initial Manganese oxide concentration (molar ratio)

Degradation products and mechanism. The treatment conditions for the degradation by-products study were set at the optimal conditions obtained using RSM. The degradation products were analyzed by HPLC-UV/MS. The detected MS peaks match well with their corresponding UV peaks in terms of relative intensity and retention time. Because of better signal intensity, evolution of degradation products was analyzed using UV absorption area changes. The MS spectral data obtained in this study provide preliminary results for possible structures of CIP degradation products by 9% Mo/OMS-2.

The products were analyzed by identifying the [M + H]⁺ molecular ions in the positive ionization mode. The molecular ion of CIP is m/z 332. Five major peaks with [M + H]⁺ molecular ions of m/z 364, 362, 334(b), 306, 263 were observed, corresponding to products with a mass change of + 32, +30, +2, -26, -69 units respectively (**Table 3.6**). A minor peak with [M + H]⁺ molecular ion of m/z 334(a) was also observed at a different retention time from that of the major peak m/z 334(b). All detected products exhibited similar fragmentation patterns to that of CIP, indicating a similarity in structure and possible conservation of the quinolone core structure. For example, all of the products detected by MS have the [M+H-

$\text{H}_2\text{O}]^+$ fragmentation ion which is likely formed by loss of H_2O from the carboxylate group of the quinolone ring.

Table 3.6 CIP degradation products analysis

Retention Time (min)	Mass spectrum Profiles				Mass difference (Da)
	$[\text{MH}]^+$	$[\text{M}+\text{Na}]^+$	$[\text{MH}-\text{H}_2\text{O}]^+$	$[\text{MH}-\text{CO}_2]^+$	
8.98	334a(35)	356(53)	316(100)	288(22)	+2
9.85	306(46)	328(16)	288(100)		-26
10.24	332(100)	354(47)	316(64)		0 (CIP)
11.36	364(100)	386(25)	346(82)		+32
12.64	362(62)	384(18)	344(100)		+30
14.15	334b(62)	356(18)	316(100)	246(12)	+2
14.4	263(18)	285(5)	245(100)		-69

To further test the hypothesis that the quinolone ring is retained in the structures of degradation products, reactivity of the quinolone ring toward 9% Mo OMS-2 was studied using a reference compound, 1, 6-dimethyl-4-oxo-1, 4-dihydroquinoline-3-carboxylic acid (QA). QA is a CIP analog except for the piperazine moiety (**Figure 3.11**). Degradation of QA by 9% Mo/OMS-2 was carried out at the same conditions as CIP degradation. Less than 5% degradation occurred after 24 hour reaction, confirming that the quinolone ring is relatively inert to oxidation in the manganese (III/IV) oxide system (data not shown). Such an observation is consistent with the previous literature where only fluoroquinolone antibiotics with piperazine substituents are reactive (6, 34). Therefore the piperazine ring is identified as the reactive site and the structures of degradation products are proposed accordingly.

transfer can take place at the N4' atom, another identified reactive site, forming a second iminium species. Subsequent hydrolysis of this N4' iminium species generates the desethylene CIP, the species m/z 306 (6). This pathway is named the N-dealkylation pathway. The species m/z 306 is the first product detected in the system. Its concentration accumulated fast in the first fifteen minutes, indicating that dealkylation may be a favorable pathway (**Figure 3.12**). Rapid decrease of the species m/z 306 concentration indicates that it undergoes a further degradation, likely another dealkylation process. Simultaneous accumulation of the species m/z 263 suggests it as a downstream product of the species m/z 306. The abundance of the species m/z 263 increased over the reaction, suggesting it is a final product (**Figure 3.12**). The species m/z 263 has been unambiguously reported as a fully dealkylated product (6, 35-36). Therefore the species m/z 263 is proposed to be a primary amine with the other two alky substitutes of N1' eliminated (**Figure 3.13**).

It is also possible that a “double iminium ion” species is formed as a reactive intermediate (6). Electrons are transferred from both the N1' atom and the N4' atom to a reactive Mn(III/IV) center to form this intermediate. The species m/z 364 is suggested to be formed via alpha-carbon hydroxylation from this “double iminium ion” species (**Figure 3.13**). Concentration analysis of the species m/z 364 indicates that it is a reaction intermediate because as the reaction progressed the concentration decreased below detection (**Figure 3.12**). Oxidation of the species m/z 364 may lead to formation of the species m/z 362 a dialdehyde compound and two monoaldehyde compounds with m/z 334. The stability of the three products in the presence of 9% Mo/OMS-2 seems to be different (**Figure 3.12**). While the concentration of the species m/z 362 and m/z 334a reached a plateau at the end of the reaction, the concentration of the species m/z 334b gradually decreased. During degradation of the species m/z 334b, the species m/z 263 accumulated at the same time. Thus transformation of the species m/z 334b is believed to be another source for the species m/z

263. The oxidative N-dealkylation process is likely to be the reaction mechanism. Based on this assumption, the species m/z 334b is proposed to be a N4' formamide with the N1' atom available to oxidation. And the species m/z 263 is suggested to form via a N1' iminium species (**Figure 3.13**).

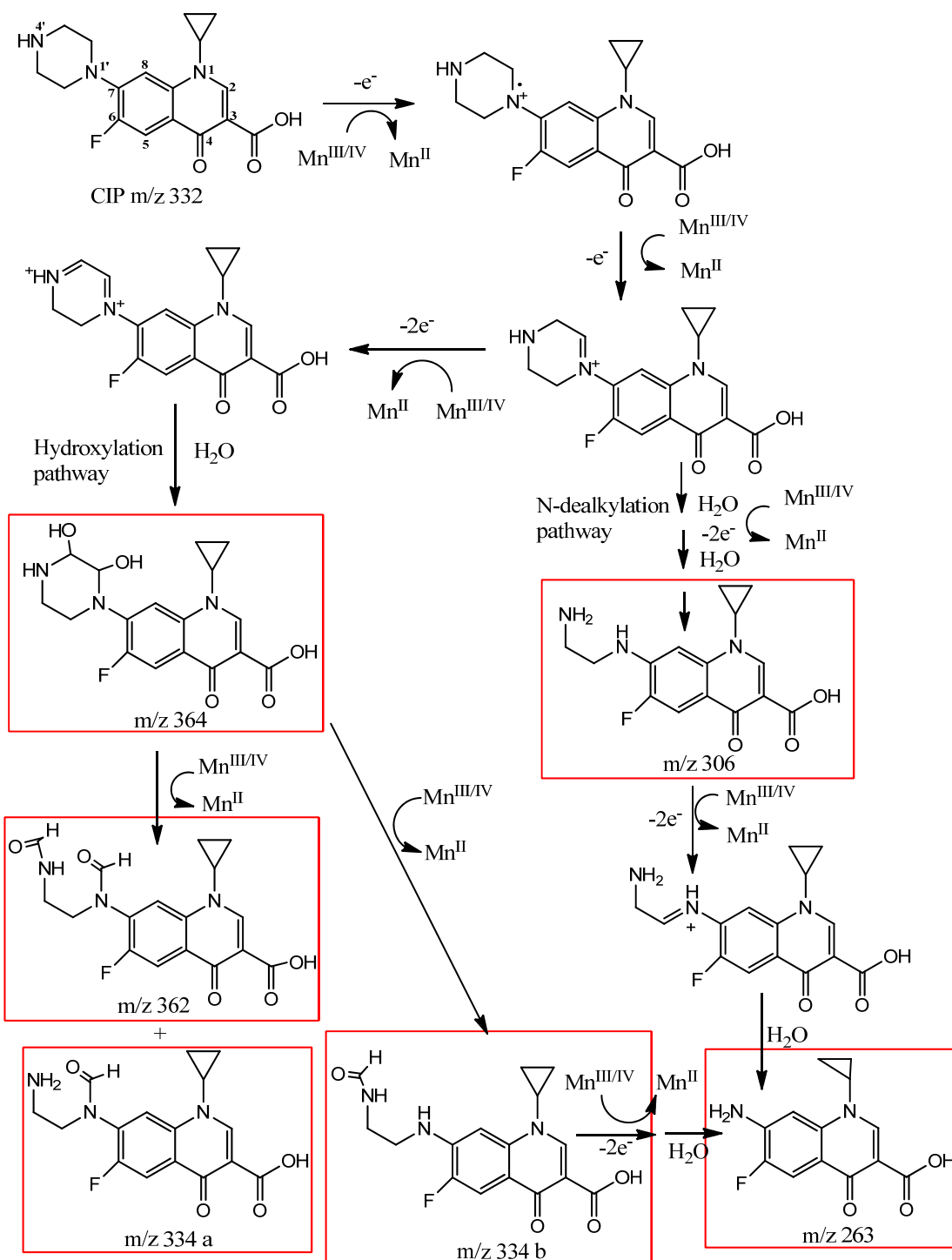


Figure 3.13 Proposed degradation products and pathways of CIP by 9% Mo/OMS-2

Unlike the Fenton system where degradation products are unselectively degraded, the species m/z 263, m/z 362 and m/z 334a were relatively stable in the 9% Mo/OMS-2 system (**Figure 3.12**) (36). Similar persistence of degradation products was also observed in a δ -MnO₂ system (6). A substantial amount of m/z 263 is still present after extending the reaction time to 16 hours. This may be due to the total consumption of reactive sites or recalcitrance of this species toward 9% Mo/OMS-2 or a combination of both. Slow removal of the species m/z 263 was observed by increasing initial oxidant dosage and extending the reaction time to days (data not shown). This transformation of the species m/z 263 may be via a radical coupling pathway similar to degradation of anilines, generating dimeric products (6, 37).

Based on the above discussion, the transformation of CIP by 9% Mo/OMS-2 is mainly occurring at the piperazine ring. The piperazine ring is the substitute at the C7 position for the quinolone antibiotic family. This position controls the potency and pharmacokinetics of the antibiotic, and five or six membered rings are considered to be the most reactive (38). Therefore, the products with an opened piperazine ring may be less potent compared to the parent compound. However, the quinolone core structure with its essential functional groups for Gyrase binding remained unattacked (38). The possibility of residual antibacterial activity cannot be ruled out. In addition, the degradation products not identified by HPLC/MS may also be biologically active (Section 2.3). For further study, biological activity tests will be conducted to give further evaluation of the treatment.

Conclusion

Doping cryptomelane with vanadium pentoxide and molybdenum trioxide increased its oxidative reactivity. Successful removal of CIP from aqueous solution can be achieved. Such improvement positively correlates with the increased surface areas of the doped derivatives. 9% Mo/OMS-2 is found to be the most effective oxidant. Optimal treatment conditions were obtained by response surface methodology at pH 3 and the [9% Mo/OMS-2, as MnO₂]:[CIP]

molar ratio ≥ 50 . Under such conditions, more than 90% CIP can be degraded within 30 minutes. Release of Mn^{II} was observed during the reaction, indicating that the redox reaction is occurring between the Mn(III/IV) reactive site and CIP. The presence of Mn^{II} ion slows down the reaction. Therefore, the kinetics was modeled by an empirical model which includes a retardation factor. Analysis of degradation products suggests that degradation of CIP mainly takes place on its piperazine ring. If by-products removal is also considered, higher ratios of oxidant to substrate and longer reaction time are suggested.

References:

1. Matocha CJS, Amonette DL, Kukkadapu JE, Ravi K (2001) Kinetics and mechanism of birnessite reduction by catechol. *Soil Sci Soc Am J* 65:58-66
2. Stone AT (1987a) Microbial metabolites and the reductive dissolution of manganese oxides: oxalate and pyruvate. *Geochim Cosmochim Acta* 51:919-925
3. Stone AT (1987b) Reductive dissolution of manganese(III/IV) oxides by substituted phenols. *Environ Sci Technol* 21:979-988
4. Wang Y, Stone AT (2006) The citric acid– $\text{Mn}^{\text{III,IV}}\text{O}_2$ (birnessite) reaction. Electron transfer, complex formation, and autocatalytic feedback. *Geochim Cosmochim Acta* 70:4463-4476
5. Zhang H, Huang CH (2003) Oxidative transformation of triclosan and chlorophene by manganese oxides. *Environ Sci Technol* 37:2421-2430
6. Zhang H, Huang C (2005) Oxidative Transformation of Fluoroquinolone Antibacterial Agents and Structurally Related Amines by Manganese Oxide. *Environ Sci Technol* 39:4474-4483
7. Lemus MA, López T, Recillas S, Frías D, Montes M, Delgado J, Centeno M, Odriozola J (2008) Photocatalytic degradation of 2, 4-dichlorophenoxyacetic acid using nanocrystalline cryptomelane composite catalysts. *Journal of Molecular Catalysis A: Chemical* 281:107-112

8. Hu B, Chen C, Frueh SJ, Jin L, Joesten R, Suib SL (2010) Removal of Aqueous Phenol by Adsorption and Oxidation with Doped Hydrophobic Cryptomelane-Type Manganese Oxide (K-OMS-2) Nanofibers. *The Journal of Physical Chemistry C* 114:9835-9844
9. Peluso MA, Gambaro LA, Pronsato E, Gazzoli D, Thomas HJ, Sambeth JE (2008) Synthesis and catalytic activity of manganese dioxide (type OMS-2) for the abatement of oxygenated VOCs. *Catalysis Today* 133:487-492
10. Zhang T, Zhang X, Ng J, Yang H, Liu J, Sun DD (2011) Fabrication of magnetic cryptomelane-type manganese oxide nanowires for water treatment. *Chem Commun* 47:1890-1892
11. Abecassis-Wolfovich M, Jothiramalingam R, Landau M, Herskowitz M, Viswanathan B, Varadarajan T (2005) Cerium incorporated ordered manganese oxide OMS-2 materials: Improved catalysts for wet oxidation of phenol compounds. *Applied Catalysis B: Environmental* 59:91-98
12. Sriskandakumar T, Opembe N, Chen CH, Morey A, King'onde C, Suib SL (2009) Green Decomposition of Organic Dyes Using Octahedral Molecular Sieve Manganese Oxide Catalysts. *The Journal of Physical Chemistry A* 113:1523-1530
13. King'onde CK, Opembe N, Chen C, Ngala K, Huang H, Iyer A, Garcés HF, Suib SL (2011) Manganese Oxide Octahedral Molecular Sieves (OMS-2) Multiple Framework Substitutions: A New Route to OMS-2 Particle Size and Morphology Control. *Advanced Functional Materials* 21:312-323
14. Gros M, Petrovic M, Barceló D (2008) Tracing pharmaceutical residues of different therapeutic classes in environmental waters by using liquid chromatography/quadrupole-linear ion trap mass spectrometry and automated library searching. *Anal Chem* 81:898-912

15. Kolpin DW, Furlong ET, Meyer MT, Thurman EM, Zaugg SD, Barber LB, Buxton HT (2002) Pharmaceuticals, hormones, and other organic wastewater contaminants in US streams, 1999-2000: a national reconnaissance. *Environ Sci Technol* 36:1202-1211
16. Ebert I, Bachmann J, Kühnen U, Küster A, Kussatz C, Maletzki D, Schlüter C (2011) Toxicity of the fluoroquinolone antibiotics enrofloxacin and ciprofloxacin to photoautotrophic aquatic organisms. *Environmental Toxicology and Chemistry* 30: 2786-2792
17. Robinson AA, Belden JB, Lydy MJ (2005) Toxicity of fluoroquinolone antibiotics to aquatic organisms. *Environmental toxicology and Chemistry* 24:423-430
18. DeGuzman RN, Shen YF, Neth EJ, Suib SL, O'Young CL, Levine S, Newsam JM (1994) Synthesis and characterization of octahedral molecular sieves (OMS-2) having the hollandite structure. *Chemistry of materials* 6:815-821
19. Gao T, Glerup M, Krumeich F, Nesper R, Fjellvåg H, Norby P (2008) Microstructures and Spectroscopic Properties of Cryptomelane-type Manganese Dioxide Nanofibers. *The Journal of Physical Chemistry C* 112:13134-13140
20. Seguin L, Figlarz M, Cavagnat R, Lassègues JC (1995) Infrared and Raman spectra of MoO_3 molybdenum trioxides and $\text{MoO}_3 \cdot x\text{H}_2\text{O}$ molybdenum trioxide hydrates. *Spectrochimica Acta Part A: Molecular and Biomolecular Spectroscopy* 51:1323-1344
21. Sun L, Cao Q, Hu B, Li J, Hao J, Jing G, Tang X (2011) Synthesis, characterization and catalytic activities of vanadium–cryptomelane manganese oxides in low-temperature NO reduction with NH_3 . *Applied Catalysis A: General* 393:323-330
22. Cerrato JM, Hochella Jr MF, Knocke WR, Dietrich AM, Cromer TF (2010) Use of XPS to Identify the Oxidation State of Mn in Solid Surfaces of Filtration Media Oxide Samples from Drinking Water Treatment Plants. *Environ Sci Technol* 44: 5881-5886

23. Toupin M, Brousse T, Bélanger D (2002) Influence of microstructure on the charge storage properties of chemically synthesized manganese dioxide. *Chemistry of materials* 14:3946-3952
24. Cai J, Liu J, Willis WS, Suib SL (2001) Framework doping of iron in tunnel structure cryptomelane. *Chemistry of materials* 13:2413-2422
25. Frederickson Jr L, Hausen D (1963) Infrared Spectra-Structure Correlation Study of Vanadium-Oxygen Compounds. *Anal Chem* 35:818-827
26. Tsilomelekis G, Boghosian S (2011) In Situ Raman and FTIR Spectroscopy of Molybdenum (VI) Oxide Supported on Titania Combined with $^{18}\text{O}/^{16}\text{O}$ Exchange: Molecular Structure, Vibrational Properties, and Vibrational Isotope Effects. *The Journal of Physical Chemistry C* 115: 2146-2154
27. Polverejan M, Villegas JC, Suib SL (2004) Higher valency ion substitution into the manganese oxide framework. *J Am Chem Soc* 126:7774-7775
28. Hardcastle FD, Wachs IE (1991) Determination of vanadium-oxygen bond distances and bond orders by Raman spectroscopy. *J Phys Chem* 95:5031-5041
29. Shin JY, Cheney MA (2004) Abiotic transformation of atrazine in aqueous suspension of four synthetic manganese oxides. *Colloids Surf Physicochem Eng Aspects* 242:85-92
30. Liu C, Zhang L, Li F, Wang Y, Gao Y, Li X, Cao W, Feng C, Dong J, Sun L (2009) Dependence of Sulfadiazine Oxidative Degradation on Physicochemical Properties of Manganese Dioxides. *Ind Eng Chem Res* 48:10408-10413
31. Rubert IV KF, Pedersen JA (2006) Kinetics of oxytetracycline reaction with a hydrous manganese oxide. *Environ Sci Technol* 40:7216-7221
32. Lin K, Liu W, Gan J (2009) Reaction of tetrabromobisphenol A (TBBPA) with manganese dioxide: kinetics, products, and pathways. *Environ Sci Technol* 43:4480-4486

33. Xu L, Xu C, Zhao M, Qiu Y, Sheng GD (2008) Oxidative removal of aqueous steroid estrogens by manganese oxides. *Water Res* 42:5038-5044
34. Wang P, He YL, Huang CH. (2010) Oxidation of fluoroquinolone antibiotics and structurally related amines by chlorine dioxide: reaction kinetics, product and pathway evaluation. *Water Res* 44: 5989-5998
35. DeWitte B, Dewulf J, Demeestere K, Vyvere VVD, Wispelaere PD, Langenhove HVL (2008) Ozonation of ciprofloxacin in water: HRMS identification of reaction products and pathways. *Environ Sci Technol* 42: 4889-4895
36. Xiao X, Zeng X, Lemley AT (2010) Species-dependent degradation of ciprofloxacin in a membrane anodic Fenton system. *J Agric Food Chem* 58: 10169-10175
37. Laha S, Luthy R (1990) Oxidation of aniline and other primary aromatic amines by manganese dioxides. *Environ Sci Technol* 24, 363-373
38. Domagala JM (1994) Structure-activity and structure-side-effect relationships for the quinolone antibacterials. *J Antimicrob Chemother* 33:685-706

CHAPTER 4

CHARACTERIZATION OF Mn(II) OXIDATION PROCESS BY LEPTOTHRIX

DISCOPHORA SS-1 MANGANESE OXIDIZING FACTOR

Introduction

The environmental significance of the Mn(II) oxidation process has been well recognized for decades because the solid-phase products oxidize various organic and inorganic compounds, scavenge many metals, and serve as electron acceptors for anaerobic respiration (1-6). Many phylogenetically diverse microorganisms are known to deposit manganese oxides in cultures or the natural environments (7-11). Microbial Mn(II) oxidation processes have gained considerable interest because it is generally believed that the biological oxidation pathway is the predominant pathway for Mn(III/IV) oxide formation in the natural environment (8, 12, 13).

Due to their oxidative versatility, natural and synthetic manganese oxides have been applied to water treatment (14, 15). One great challenge in this technology is the release and accumulation of Mn(II) during the redox reaction since Mn(II) reoxidation by aeration is slow, limiting its application. It has now been recognized that Mn(II) oxidizing microorganisms may provide a prospective solution (16).

Enzymes, including a multi copper oxidase (MCO) from *Bacillus spp.* and heme-containing Mn(II)-oxidizing peroxidases (MOP) from *Aurantimonas* and *Erythrobacter* species, have been identified by tandem mass spectrometry and linked to Mn(II) oxidation in bacteria (17, 18). Genetic approaches to identifying the microbial Mn(II) oxidation mechanism have been less successful so far. Deletion of the MCO gene (*cumA*) and the MOP gene in *P. putida* GB-1 does not impair its Mn(II) oxidation ability (19). Temporal variation of *mofA* transcript level, a MCO gene of *L. discophora SS-1*, did not correlate with the change of its manganese oxidizing activity (20). In addition, cloning and co-expression of the *mof* operon of *L. discophora SS-1* in *E. Coli* did not yield any manganese oxidizing activity (21). In addition to the direct Mn(II) oxidation by enzymes, indirect enzymatic processes may also contribute to the Mn(II) oxidation, such as

bacterially generated superoxide mediated Mn(II) oxidation, which was discovered recently in a marine bacterium (22). In this scenario, Mn(III/IV) oxides are formed as a combination of abiotic and biotic process.

Despite numerous research efforts as mentioned above, the mechanism and ecological role of Mn(II) oxidation by microorganisms remain unclear and are still under active research. Advancing the understanding of these mechanisms will provide insights on the Mn cycle in the environment and its ecological impacts and facilitate development of a feasible biotechnology for pollution control and remediation.

It should be noted that solution conditions, such as presence of certain co-solutes, can have a significant effect on biological Mn (II) oxidation processes (23, 24). The consideration of matrix effects is especially important when utilizing this biotechnology method for water treatment because wastewater matrices are often complicated and may have potential chemical inhibitors for Mn(II) oxidation (16). While previous research focused on the effects of co-solutes on biogenic manganese oxide (BioMnO_x) oxidative reactivity, potential interference with biological Mn(II) oxidation and re-oxidation, crucial processes for initiating oxidation and controlling secondary pollution due to Mn(II) release, has been long neglected (16, 25, 26). Gaining knowledge of the biochemical aspect of Mn(II) oxidation is helpful for developing and optimizing the treatment process.

Leptothrix discophora SS-1, a well studied model Mn(II) oxidizing microorganism, was selected in this study. The main objectives of this study are: 1. develop a method that describes kinetics of Mn(II) oxidation process by *L. discophora* SS-1; 2. evaluate the contribution of superoxide mediated abiotic Mn(II) oxidation to BioMnO_x formation; 3. evaluate the effects of co-solutes on Mn(II) oxidation in batch experiments.

Materials and Methods

Bacterial growth and filtrate preparation. *L. discophora SS-1* is a sheathless variant of the gram-negative bacterium *L. discophora SP-6*. The bacterium was grown at room temperature under 100 rpm shaking in PYG medium as described previously by Adams *et al.* (23). Specifically, the medium contained 0.25g each of peptone, yeast extract, and glucose, plus 0.60g $\text{MgSO}_4 \cdot 7\text{H}_2\text{O}$ and 0.07g $\text{CaCl}_2 \cdot 2\text{H}_2\text{O}$ per liter Milli-Q water. The pH of the medium was adjusted with 1M NaOH to 7.6 prior to autoclaving. Cell growth was monitored by determining the optical density at 600 nm.

During growth, the manganese oxidizing factor (MOF) was excreted to the culture medium by the bacterium. In the culturing condition used in this study, the majority of Mn(II) oxidation activity was in this excreted form and only 10% of the total activity was associated with the cell material (23). Although a minor portion of the manganese oxidizing activity was associated with the cells, only extracellular fluid was used to avoid interference on cell growth and other metabolic process. Cell free filtrate was prepared by growing *L. discophora SS-1* without MnCl_2 to early stationary phase ($\text{OD}_{600} \sim 0.25$) and centrifuging at 3000g for 10 min. The supernatant was passed through a 0.22 μm filter (Millipore, USA) and the resulting solution was the cell free filtrate.

Determination of Mn(II) – oxidizing activity. The oxidation reaction was started by adding the desired amount of MnCl_2 to the cell free filtrate in HEPES buffer (pH = 7.4). The Mn(II) oxidizing activity of MOF was determined quantitatively by both turbidity measurement and Leucoberbelin blue (LBB) assay (23, 27). Upon oxidation of Mn(II), a fine yellow or light brown suspension formed. The turbidity was measured as the optical density at 600 nm, a wavelength at which no significant interference would be expected from proteins, nucleic acids or other organic

material. A serial dilution of BioMnO_x was used to make the standard curve, giving linearity up to 200 μM. LBB, a reducing reagent, is oxidized by Mn with valences of +3 or higher, resulting in a blue product with a peak absorption at 618 nm. Since the manganese in BioMnO_x was likely to be a mixture of Mn(II), Mn(III) and Mn(IV), KMnO₄ was used as the standard. In the LBB assay, 40 μM KMnO₄ was equivalent to 100 μM MnO₂. All Mn(II) oxidation assays were performed at room temperature. Since the Mn(II) oxidizing activity of cells differed slightly from batch to batch, effects of variation in oxidizing activity were eliminated by using the same batch of cell culture to investigate a single factor.

Test of superoxide hypothesis. Super oxide dismutase (SOD) (0.5-5 μM) was added to the cell free filtrate and Mn(II) oxidation kinetics were monitored in two hours. The oxidation kinetics was compared to a positive control which is done in absence of SOD. In addition, effects of a superoxide quencher (Cu²⁺) (0.2-20 μM) and a substrate for superoxide production (NADH, 200 μM) on Mn(II) oxidation kinetics were studied as well at the same time range.

Inhibition of Mn^{II} oxidation. Before the chemical inhibitor screening test for the co-solutes, an optimal range of initial Mn(II) concentration was established. Then a desired amount of co-solutes, including a ligand (pyrophosphate), and trace organic contaminants (antibiotics), were added to the cell-free filtrate. The mixture was incubated for 5 minutes and then Mn²⁺ was added to initiate the oxidation process. Since certain reductive organic contaminants will cause interference in the LBB measurement by competing for the oxidant (BioMnO_x) observed in preliminary experiments, only turbidity measurement was used to quantify MOF activity.

Results and Discussion

Measurement of MOF activity. Mn(II) oxidation was conducted at room temperature in HEPES buffer at pH 7.4, an optimal pH for the process (28, 29). The oxidation took place in 30-

50 minutes with formation of a brown suspension. The oxides were quantified by the LBB method and turbidity measurement. The LBB assay is a more established method for Mn(III/IV) quantification (22, 27). Thus turbidity measurement was compared with the results from the LBB assay. Both methods gave standard curves which were linear up to 200 μM , and the two measurements correlate well with each other (**Appendix E**). Thus, turbidity measurement was justified to give a reasonably accurate measurement (4-200 μM), and, in the following kinetic study, it was used as the quantification method unless stated otherwise.

A typical growth curve of *L. discophra* SS-1 in the PYG medium in the 1L flask culture is shown in **Figure 4.1**. The cells reached stationary phase after 96 hours growth. The MOF activity seems to correlate closely with cell density: Mn(II) oxidation was negligible in the first 24 hours when cell density was very low; as cells grew to log phase, the MOF activity increased and reached a plateau at the stationary phase. Decrease of MOF activity was observed when cells began to decay in the death phase. The MOF activity is similar to that cultured in minimum mineral salt (MMS) medium (27). However, the growth curve is slower in this study which may be due to a smaller initial inoculation percentage. Compared to a delay of peak MOF activity in MMS medium and a steep drop of the activity in the death phase, the intensity of MOF activity correlates with the cell density until the stationary phase and remains almost the same through the early death phase (27). This observed difference in MOF activity – growth phase relationship may be due to a difference in the testing method (whole cell suspension versus cell free filtrate tested) and the culturing medium (MMS vs PYG). Since MOF activity becomes stable from the late log phase, filtrate was prepared from cells at an early stationary phase for the further studies.

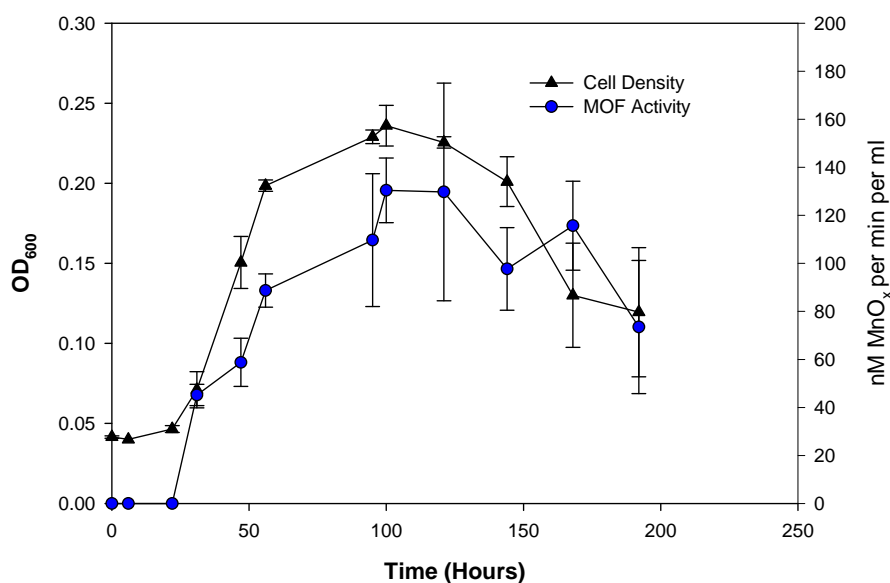
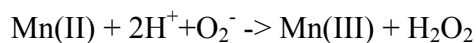


Figure 4.1 Cell growth and MOF activity of *L. discophora* SS-1.

Test of superoxide hypothesis. Recently, a novel indirect enzymatic oxidation pathway involving extracellular superoxide was discovered in a marine bacterium *Roseobacter sp. AzwK-3b*. The process is shown below.



The abiotically oxidized Mn(III) intermediate is further oxidized by an unknown oxidant or undergoes disproportionation, generating the Mn(III/IV) oxides. The role of superoxide in Mn(II) oxidation by *L. discophora* SS-1 was studied. Compared to the *Roseobacter sp. AzwK-3b* system, a different response to the superoxide quenchers and production promoter was observed.

As shown in **Table 4.1**, the presence of superoxide dismutase (SOD) did not affect Mn(II) oxidation. Cu^{2+} , a known superoxide quencher, was added to the filtrate to further evaluate the effects of superoxide. Presence of Cu^{2+} up to 20 μM did not affect the oxidation rates (**Table 4.1**). Interestingly, on the contrary, MOF seems to be more sensitive to Zn^{2+} , an analog to Cu^{2+} without catalytic superoxide dismutation activity. A similar trend was observed in a previous

study reported in the literature, where Zn^{2+} was more inhibitory than Cu^{2+} (30). The non-inhibitory effect of Cu^{2+} observed in this study may be due to the chelating effect of organic ligands in the filtrate, leading to a reduced effective Cu^{2+} concentration.

A link between NADH oxidoreductase and bacterial extracellular superoxide production has been observed by others (31, 32). Addition of NADH, a substrate for superoxide production, inhibited $BioMnO_x$ formation significantly while the oxidized form (NAD^+) does not affect the oxidation rate. This indicates that either superoxide is not involved in Mn(II) oxidation or NADH oxidoreductase is not involved for extracellular superoxide production. The observed inhibition caused by NADH may be due to a redox reaction between NADH and the reactive intermediate Mn(III) or neo-formed $BioMnO_x$. A test can be performed to confirm the occurrence of the redox reaction in the future by incubating preformed $BioMnO_x$ and NADH and monitoring reductive dissolution of $BioMnO_x$ or formation of NAD^+ . Based on the discussions above, unlike *Roseobacter sp. AzwK-3b*, indirect oxidation by superoxide is not likely to be an important pathway in the *L. discophora SS-1* system.

Table 4.1 Evaluation the effects of superoxide on Mn(II) oxidation*

Test Reagent	Mn(II) oxidation activity
Superoxide Dismutase (SOD) (5 μ M)	100%
Cu^{2+} (20 μ M)	100%
Zn^{2+} (20 μ M)	71.3%
NAD^+ (200 μ M)	100%
NADH(200 μ M)	31.2%

*Concentration of each reagent was selected based on literature (22, 30).

Effects of Mn^{II} on oxidation kinetics. Initial Mn(II) concentration is an important process parameter in a bioreactor that uses Mn(II) oxidizing bacteria because of the strong inhibitory effects of residual Mn(II) on the reactivity of BioMnO_x and the potential toxicity on the microorganisms (24). The effect of initial Mn(II) concentration on oxidation kinetics was explored to find the optimal concentration range for MOF. The initial oxidation rate increased as the Mn(II) initial concentration increased up to 75 μM and reached a plateau from 75 to 125 μM (**Figure 4.2**). An inhibition of the oxidation was observed when the initial Mn(II) concentration was increased to 200 μM, and complete elimination was observed at [Mn(II)] = 800 μM. A similar trend was reported in the Adams' study although the optimal concentration range is much narrower here (30). For the following studies, Mn(II) was added at 100 μM where MOF is saturated with the substrate and has the maximum oxidation rate.

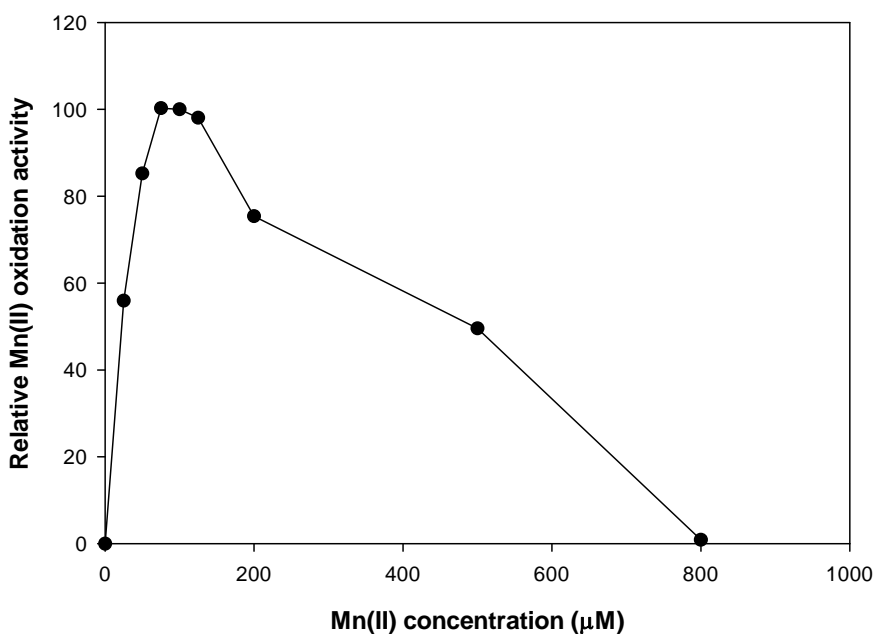


Figure 4.2 Effect of Mn(II) on MOF activity.

Effects of chemical inhibitors. MOF is generally believed to be an enzyme or enzyme complex sensitive to certain chemicals, such as cyanide and o-phenanthroline (23). Wastewater represents a complex water matrix with a variety of chemicals that can be potential inhibitors for MOF. Such adverse effects on Mn(II) oxidation can lead to retarded removal and reduced treatment efficiency in a Mn oxidizing bacteria-based bioreactor. A screening study for potential inhibitors gives valuable information for defining the treatment specification and limitations. The results of the screening study are listed in **Table 4.2**.

Table 4.2 Effect of chemical inhibitors on MOF activity

Compound and Concentration (μM)	MOF Activity/Control (%) *
Pyrophosphate (2 mM)	0%
Kanamycin (50 μM)	0.5%
Tetracycline (50 μM)	42.8%
Oxytetracycline (50 μM)	52.4%
Chlortetracycline (50 μM)	13.1%
Ampicillin (50 μM)	100%
Ciprofloxacin (20 μM)	100%

* The MOF activity is quantified by turbidity measurement.

Pyrophosphate is found to inhibit manganese oxide formation significantly. When pyrophosphate concentration is higher than 2mM, no precipitates formed. Bacterial Mn(II) oxidation is suggested to be a two step electron transfer process with Mn(III) as an intermediate (33). Know as a good chelator for Mn(III), pyrophosphate is hypothesized to stabilize Mn(III) in solution and prevents it from further oxidation by MOF.

Thus Mn(II) oxidation was studied in the presence of a range of pyrophosphate concentrations. Oxidized Mn was analyzed by the LBB assay in both whole BioMnO_x suspension and filtered

suspension. LBB is a reductive dye that can be oxidized by both Mn(III) and Mn(IV), giving a measurement of total reactive Mn. In the low pyrophosphate concentration range (0-500 μ M), no reactive Mn was observed in the filtered suspension, indicating the absence of chelated Mn(III) in solution (**Figure 4.3 A**). At the high pyrophosphate concentration range (>2 mM), the same reactive Mn amount was found in filtered and whole suspension, suggesting that all the oxidized Mn(II) is in the form of chelated Mn(III) (**Figure 4.3 C**). This result is consistent with the observation of negligible manganese oxide precipitation. Thus Mn(II) is still oxidized by MOF but trapped in the Mn(III) form. At an intermediate pyrophosphate concentration (1mM), an interesting Mn(II) oxidation pattern was observed (**Figure 4.3 B**). Mn(II) oxidation is delayed since no reactive Mn is formed until after 2 hours. The first reactive Mn species seems to appear in aqueous solution in the form of Mn(III), as indicated by the same amount of LBB-reactive Mn detected in filtered and whole suspension. As reaction progressed, precipitates started to form and accumulate. Meanwhile, reactive Mn in the aqueous form declined. Such observation indicates that MOF is capable of transforming Mn(III) to Mn(IV). Therefore inhibition of manganese oxide formation by pyrophosphate is mainly due to chelating effects that may work at two different steps: (1) limit the Mn(II) availability to the enzyme, as indicated by the lag phase; (2) competitively bind Mn(III) and prevent its further oxidation (**Figure 4.3 C**).

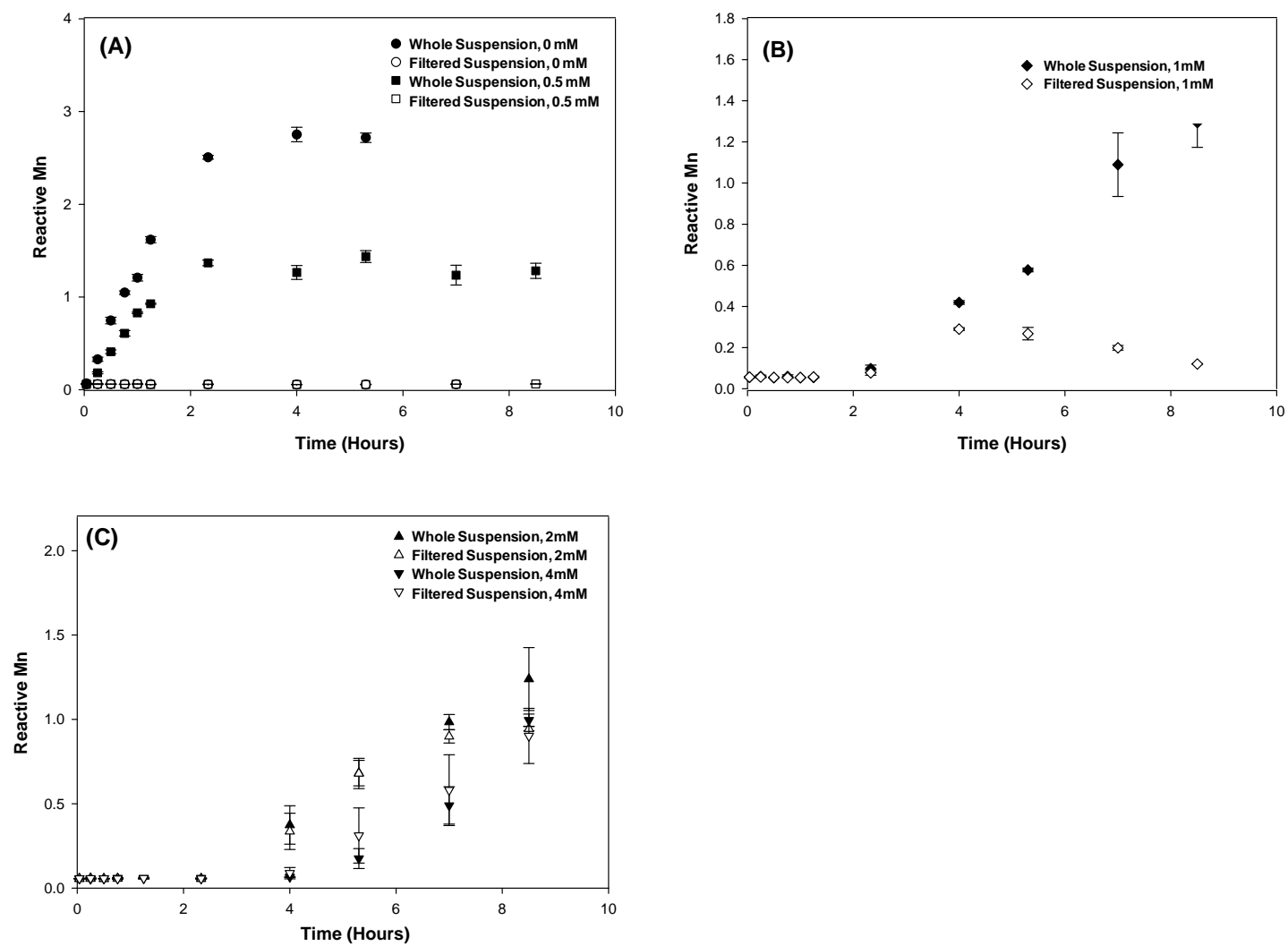


Figure 4.3 Effect of pyrophosphate on Mn(II) oxidation, measured by the LBB assay.

The presence of certain antibiotics also affects BioMnO_x formation. Since antibiotics are reductive at the acidic condition used in the LBB assay, only the turbidity measurement was suitable for manganese oxide quantification. Of the antibiotics screened, the tetracycline family and the aminoglycoside family were observed to cause significant inhibition of BioMnO_x formation (**Table 4.1**). For example, tetracycline caused 57.2 % reduction in the initial oxidation rate. The dose and response relationship was further studied using a sigmoidal mode, giving an IC₅₀ of 3.6 μM for kanamycin and 450.5 μM for tetracycline (**Figure 4.4, BioDataFit 1.02**).

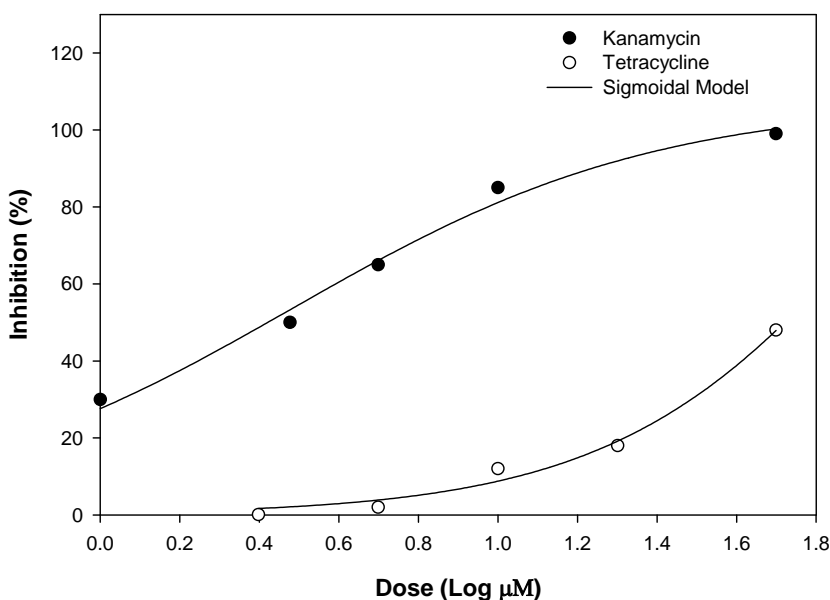


Figure 4.4 Effect of kanamycin and tetracycline on Mn(II) oxidation

The inhibition mechanisms remain unclear. Three hypotheses are proposed to explain the observation: (1) in situ reductive dissolution of neo-formed manganese oxides by the antibiotics, as shown in the equation below:



(2) chelating with Mn(II) or Mn(III), thus reducing their accessibility to MOF; (3) poisoning the enzyme, such as changing its conformation.

The first hypothesis was tested by monitoring the concentration of both BioMnO_x and antibiotics during incubation of preformed BioMnO_x and antibiotics. Reductive dissolution of BioMnO_x, determined by turbidity measurement, was negligible in the time range studied (2 - 4 hours) (data not shown). Using tetracycline as the probe, the change in antibiotic concentration was not obvious (**Figure 4.5**). Thus, reductive dissolution is unlikely to be the major reason for the inhibition.

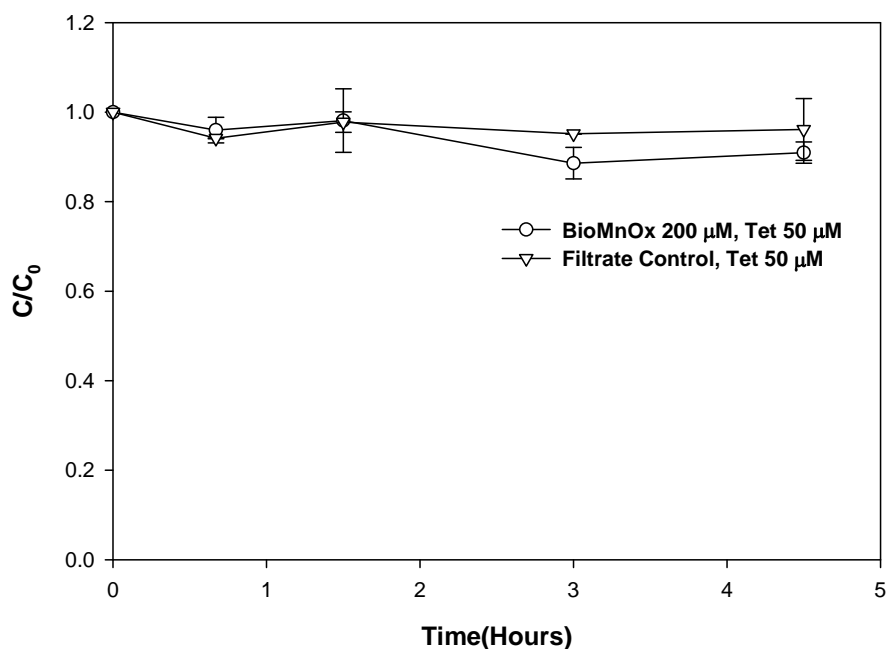


Figure 4.5 Transformation of tetracycline by BioMnO_x. [BioMnO_x] = 200μM, pH = 7.3, Tetracycline = 50 μM

The second hypothesis is difficult to test due to limited available data on binding constants of tetracycline and kanamycin with Mn(II) and Mn(III) and difficulty in analytical techniques to differentiate each speciation. However, the structures of the two antibiotic families have a

signature of multiple –OH functional groups which can be a potential chelating site for the metal ions. A pyrophosphate-like mechanism might take place. Interestingly, adding Mg^{2+} to the antibiotic solution to block the chelating sites and increase Mn availability did not eliminate the inhibition.

The third hypothesis is also difficult to test. Efforts have been made to compare the activity of exposed and unexposed MOF by ultrafiltration. However, the MOF lost a major portion of its activity during the process in a preliminary test. It is worth noting that even the antibiotic inhibitors changed the initial kinetics; given a long enough time (a few days), precipitates were observed to form. However, it is not clear if the oxidation is due to recovered enzyme activity or a combination of biological and abiotic processes, i.e, enzyme initiated oxidation followed by surface catalyzed oxidation.

Conclusion

Mn(II) oxidation is catalyzed by MOF excreted by *L. discophora* SS-1. An optimal initial Mn(II) concentration range is between 75-125 μ M. The abiotic oxidation of Mn(II) by superoxide does not seem to be an important pathway in this bacterium. Low concentration of ligand (pyrophosphate) does not affect manganese oxide formation significantly. In high concentration of pyrophosphate, Mn(II) is only oxidized to Mn(III) without any precipitate formation. The Mn(II) oxidation kinetic pattern changed in the presence of the tetracycline and aminoglycoside antibiotic family; yet the reason remains to be investigated. This study serves as a preliminary study for developing water treatment biotechnology that makes use of Mn(II) oxidizing bacteria. Precautions should be taken since co-solutes in the water matrix may cause a lag in Mn(II) oxidation or inhibition of Mn(II) oxidation and reoxidation, leading to a reduction in treatment efficiency. Moreover, this study is only conducted in a single-chemical exposure

mode. Multiple chemical exposures should be factored in due to possible additive or synergistic effects. The next chapter focuses on the chemical aspect of BioMnO_x using the optimal conditions discussed above to preform the oxides.

References

1. Stone, A.T. Reductive dissolution of manganese (III/IV) oxides by substituted phenols. *Environ. Sci. Technol.* 1987, *21*, 979-988.
2. Stone, A.T. and Morgan, J.J. Reduction and dissolution of manganese (III) and manganese (IV) oxides by organics: 2. Survey of the reactivity of organics. *Environ. Sci. Technol.* 1984, *18*, 617-624.
3. He, J.; Meng, Y.; Zheng, Y.; Zhang, L. Cr(III) oxidation coupled with Mn(II) bacterial oxidation in the environment. *Journal of Soils and Sediments* 2010, *10*, 767-773.
4. McBride, M. Adsorption and oxidation of phenolic compounds by iron and manganese oxides. *Soil Sci. Soc. Am. J.* 1987, *51*, 1466-1472.
5. Nelson, Y.M.; Lion, L.W.; Ghiorse, W.C.; Shuler, M.L. Production of biogenic Mn oxides by *Leptothrix discophora* SS-1 in a chemically defined growth medium and evaluation of their Pb adsorption characteristics. *Appl. Environ. Microbiol.* 1999, *65*, 175.
6. Stone, A.T. Microbial metabolites and the reductive dissolution of manganese oxides: oxalate and pyruvate. *Geochim. Cosmochim. Acta* 1987, *51*, 919-925.
7. Tebo, B.M.; Johnson, H.A.; McCarthy, J.K.; Templeton, A.S. Geomicrobiology of manganese (II) oxidation. *Trends Microbiol.* 2005, *13*, 421-428.
8. Tebo, B.M.; Bargar, J.R.; Clement, B.G.; Dick, G.J.; Murray, K.J.; Parker, D.; Verity, R.; Webb, S.M. Biogenic manganese oxides: properties and mechanisms of formation. *Annu. Rev. Earth Planet. Sci.* 2004, *32*, 287-328.

9. Emerson, S.; Kalthorn, S.; Jacobs, L.; Tebo, B.M.; Nealson, K.H.; Rosson, R.A. Environmental oxidation rate of manganese (II): bacterial catalysis. *Geochim. Cosmochim. Acta* 1982, 46, 1073-1079.
10. Anderson, C.; Davis, R.; Bandolin, N.; Baptista, A.; Tebo, B. Analysis of in situ manganese (II) oxidation in the Columbia River and offshore plume: linking *Aurantimonas* and the associated microbial community to an active biogeochemical cycle. *Environ. Microbiol.* 2011,
11. Clement, B.G.; Luther III, G.W.; Tebo, B.M. Rapid, oxygen-dependent microbial Mn (II) oxidation kinetics at sub-micromolar oxygen concentrations in the Black Sea suboxic zone. *Geochim. Cosmochim. Acta* 2009, 73, 1878-1889.
12. Diem, D. and Stumm, W. Is dissolved Mn^{2+} being oxidized by O_2 in absence of Mn-bacteria or surface catalysts? *Geochim. Cosmochim. Acta* 1984, 48, 1571-1573.
13. Hennebel, T.; De Gusseme, B.; Boon, N.; Verstraete, W. Biogenic metals in advanced water treatment. *Trends Biotechnol.* 2009, 27, 90-98.
14. Hu, B.; Chen, C.; Frueh, S.J.; Jin, L.; Joesten, R.; Suib, S.L. Removal of Aqueous Phenol by Adsorption and Oxidation with Doped Hydrophobic Cryptomelane-Type Manganese Oxide (K-OMS-2) Nanofibers. *The Journal of Physical Chemistry C* 2010, 114, 9835-9844.
15. Rudder, J.; Wiele, T.; Dhooge, W.; Comhaire, F.; Verstraete, W. Advanced water treatment with manganese oxide for the removal of 17 [alpha]-ethynylestradiol (EE2). *Water Res.* 2004, 38, 184-192.
16. Forrez, I.; Carballa, M.; Verbeken, K.; Vanhaecke, L.; , M.S.; Ternes, T.; Boon, N.; Verstraete, W. Diclofenac Oxidation by Biogenic Manganese Oxides. *Environ. Sci. Technol.* 2010, 44, 3449-3454.

17. Dick, G.J.; Torpey, J.W.; Beveridge, T.J.; Tebo, B.M. Direct identification of a bacterial manganese (II) oxidase, the multicopper oxidase MnxG, from spores of several different marine *Bacillus* species. *Appl. Environ. Microbiol.* 2008, *74*, 1527-1534.
18. Anderson, C.; Johnson, H.; Caputo, N.; Davis, R.; Torpey, J.; Tebo, B. Mn (II) oxidation is catalyzed by heme peroxidases in “*Aurantimonas manganoxydans*” strain SI85-9A1 and *Erythrobacter* sp. strain SD-21. *Appl. Environ. Microbiol.* 2009, *75*, 4130-4138.
19. Geszvain, K. and Tebo, B.M. Identification of a two-component regulatory pathway essential for Mn (II) oxidation in *Pseudomonas putida* GB-1. *Appl. Environ. Microbiol.* 2010, *76*, 1224-1231.
20. El Gheriany, I.A.; Bocioaga, D.; Hay, A.G.; Ghiorse, W.C.; Shuler, M.L.; Lion, L.W. An uncertain role for Cu (II) in stimulating Mn (II) oxidation by *Leptothrix discophora* SS-1. *Arch. Microbiol.* 2011, *193*, 89-93.
21. El Gheriany, I.A.. Mn(II) oxidation by *Leptothrix discophora* SS-1. Ph. D dissertation, Cornell University, 2010.
22. Learman, D.R.; Voelker, B.M.; Vazquez-Rodriguez, A.I.; Hansel, C.M. Formation of manganese oxides by bacterially generated superoxide. *Nature Geoscience* 2011, *4*, 95-98.
23. Adams, L. and Ghiorse, W.C. Characterization of extracellular Mn²⁺ oxidizing activity and isolation of an Mn²⁺ oxidizing protein from *Leptothrix discophora* SS-1. *J. Bacteriol.* 1987, *169*, 1279-1285.
24. Forrez, I.; Carballa, M.; Noppe, H.; De Brabander, H.; Boon, N.; Verstraete, W. Influence of manganese and ammonium oxidation on the removal of 17 [alpha]-ethinylestradiol (EE2). *Water Res.* 2009, *43*, 77-86.

25. Forrez, I.; Carballa, M.; Fink, G.; Wick, A.; Hennebel, T.; Vanhaecke, L.; Ternes, T.; Boon, N.; Verstraete, W. Biogenic metals for the oxidative and reductive removal of pharmaceuticals, biocides and iodinated contrast media in a polishing membrane bioreactor. *Water Res.* 2011, *45*, 1763-1773.
26. Kim, D.G.; Jiang, S.; Jeong, K.; Ko, S.O. Removal of 17 α -Ethinylestradiol by Biogenic Manganese Oxides Produced by the *Pseudomonas putida* strain MnB1. *Water, Air, & Soil Pollution* 2012, 1-10.
27. El Gheriany, I.A.; Bocioaga, D.; Hay, A.G.; Ghiorse, W.C.; Shuler, M.L.; Lion, L.W. Iron requirement for Mn (II) oxidation by *Leptothrix discophora* SS-1. *Appl. Environ. Microbiol.* 2009, *75*, 1229-1235.
28. Boogerd, F. and De Vrind, J. Manganese oxidation by *Leptothrix discophora*. *J. Bacteriol.* 1987, *169*, 489-494.
29. Zhang, J.; Lion, L.W.; Nelson, Y.M.; Shuler, M.L.; Ghiorse, W.C. Kinetics of Mn (II) oxidation by *Leptothrix discophora* SS1. *Geochim. Cosmochim. Acta* 2002, *66*, 773-781.
30. Adams, L.F. Physiology, cytology, and manganese oxidizing activity of *Leptothrix discophora* SS-1. Ph.D dissertation, Cornell University, 1986.
31. Korshunov, S. and Imlay, J.A. Detection and quantification of superoxide formed within the periplasm of *Escherichia coli*. *J. Bacteriol.* 2006, *188*, 6326-6334.
32. Lin, P.C.; Türk, K.; Häse, C.C.; Fritz, G.; Steuber, J. Quinone reduction by the Na⁺ - translocating NADH dehydrogenase promotes extracellular superoxide production in *Vibrio cholerae*. *J. Bacteriol.* 2007, *189*, 3902-3908.

33. Webb, S.M.; Dick, G.J.; Bargar, J.R.; Tebo, B.M. Evidence for the presence of Mn (III) intermediates in the bacterial oxidation of Mn (II). *Proc. Natl. Acad. Sci. U. S. A.* 2005, *102*, 5558.

CHAPTER 5

DEGRADATION OF CIPROFLOXACIN AND BISPHENOL A BY BIOGENIC MANGANESE OXIDES

Abstract

Natural Mn(III/IV) oxides are recognized as important strong oxidants in environment, affecting the environmental fate of many micropollutants. The biological Mn(II) oxidation process is believed to be the predominant pathway for natural Mn(III/IV) oxide formation. In this study, *Leptothrix discophora SS-1*, a Mn(II) oxidizing bacterium, was used to produce biogenic manganese oxides (BioMnO_x). The structure and oxidative reactivity of BioMnO_x were characterized and compared to that of its synthetic analog (a birnessite type MnO₂). XRD results indicated that BioMnO_x is poorly crystallized, similar to δ-MnO₂ (c-disordered birnessite). XPS and TGA results indicated a considerable amount of organic residual present in BioMnO_x. The oxidative reactivity of BioMnO_x was investigated by degradation of ciprofloxacin (CIP) and bisphenol A (BPA), and oxidation rates with BioMnO_x were much slower than with its synthetic analog. Smaller surface area, larger particle sizes, lower average oxidation states (AOS) and blocking of reactive sites by organic residual may explain the lower reactivity of BioMnO_x. Despite the slower reaction kinetics, successful removal of CIP and BPA was achieved in the BioMnO_x system. Solution conditions played a key role in determining degradation kinetics. Co-solutes (metal cations and humic acid) inhibited the oxidation by competitively binding with the reactive surface sites. The pH effect was more complicated since both oxidant and substrate can be affected, and a net effect resulted from a combination of several processes. Compared to the synthetic MnO₂ system, the BioMnO_x system yielded fewer degradation products. Degradation of CIP was mainly via N-dealkylation. BPA oxidation underwent a radical fragmentation and complicated radical couplings, yielding an olefin product and polymerized precipitate. Generally, lower biological activity of the degradation products is expected based on the proposed structures.

Introduction

Mn(III/IV) oxides are naturally occurring minerals that widely distributed in environment. They are known to play key roles in elemental biogeochemical cycles due to high sorptive and oxidative capacity (1-4). Recently, the influence of Mn(III/IV) oxides on the environmental fate of xenobiotics has gained considerable research interest (5-8). It is generally believed that the biological Mn(II) oxidation process is the predominant pathway for Mn(III/IV) oxide formation in the natural environment due to limited rates of abiotic oxidation of Mn(II) at circum-neutral conditions (9, 10). Field studies also confirmed the importance of biological Mn(II) oxidation (11, 12).

Structural studies suggest that biogenic Mn(III/IV) oxides (BioMnO_x) from different bacteria are layer type manganese oxides similar to δ -MnO₂ (c-disordered birnessite), a widely used model Mn(III/IV) oxide (10, 13-16). Despite the structural similarity, the reactivity of BioMnO_x may be quite different from that of its synthetic analog, and a higher adsorption capacity of BioMnO_x, generated by *L. discophora SS-1* and a fungus *KR 21-2*, has been reported (17, 18). However, little is known about the oxidative reactivity of BioMnO_x, especially with respect to the degradation of organics. Research on the properties of BioMnO_x on this aspect will provide further understanding on the environmental role of BioMnO_x.

Lepthorix discophora SS-1 is a well studied model Mn(II) oxidizing organism. During growth in batch culture, this sheathless bacterium releases a manganese oxidizing factor (MOF) into the medium. High affinity of MOF for Mn(II) has been reported (19). With prior knowledge of Mn(II) oxidation kinetics and optimal conditions, this organism is ideal for producing BioMnO_x.

The main objectives of this study were to: investigate the oxidizing capacity of BioMnO_x toward the emerging contaminants ciprofloxacin (CIP) and bisphenol-A (BPA); compare the

structure and reactivity of biologically and chemically produced Mn(III/IV) oxide; evaluate the effects of solution conditions such as pH and co-solutes on the reaction kinetics; analyze the major degradation products and propose pathways.

Materials and Methods

Chemicals. All chemicals used in this research were of analytical grade or above. Deionized water (18.3 M Ω -cm resistivity) was employed to prepare the reaction solutions. Ciprofloxacin (CIP) and Bisphenol A (BPA) were purchased from Sigma. All chemical reagents were used directly without further purification.

Preparation of biogenic manganese oxides and its synthetic analoge. *L. discophora SS-1*, the Mn(II) oxidizing model organism, was grown in 400ml of PYG medium in 1000-ml Erlenmeyer flasks at 21 °C under constant orbital shaking at 100 rpm (19). During growth, the manganese oxidizing factor (MOF) was found in the culture medium. The cell free filtrate was prepared as described in Chapter 4, with cell material removal by centrifugation followed by filtration using a 0.22 μ m membrane filter.

BioMnO_x was produced post culture upon addition of MnSO₄ (100 μ M) to the filtrate. The BioMnO_x solids were collected and washed twice with DI water. To remove the Mn(II) adsorbed on the surface, the oxides were further washed by diluted HCl (pH = 3) three times followed by washing three times by DI water. MOF and other organic molecules in the filtrate co-precipitate with BioMnO_x during the formation. To remove the organic debris, a bleach procedure was carried out. After removal of surface adsorbed Mn(II), the BioMnO_x was washed with 0.17% NaClO (pH = 10), giving BioBleMnO_x (20).

Synthetic MnO₂ was synthesized according to Murray et al. (21). Specifically, 16 mL of 0.1 M KMnO₄ was added to 328 mL of N₂-sparged deionized water, and the solution was made basic

by addition of 32 mL of 0.1 M NaOH. Precipitation of manganese oxides was initiated by adding 24 mL of 0.1 M MnCl₂ dropwise to the basic permanganate solution under constant stirring. The precipitate was collected by centrifugation and washed by deionized water several times. All three types of Mn(III/IV) oxide suspensions were stored at 4 °C and were diluted to appropriate concentration prior to use.

Characterization of BioMnO_x and its synthetic analog. Biogenic and synthetic Mn(III/IV) oxide were freeze dried and ground in an agate mortar. Powder X-ray powder diffraction (XRD) analysis was conducted on a Scintag Theta-Theta X-ray diffractometer with Cu K α radiation ($\lambda=1.5418$ Å).

The surface chemical composition was analyzed by x-ray photoelectron spectroscopy (XPS). The surface areas were determined by the Brunauer-Emmett-Teller method of N₂ adsorption on a Micromeritics ASAP 2010 system. Prior to the analysis, the samples were degassed at 110°C for 12h. The thermal gravimetric analysis was conducted using TA Q500. The temperature was equilibrated at 25 °C for five minutes and then increased at 10 °C per minute up to 800 °C.

For the morphology study, a drop of Mn(III/IV) oxide suspension was deposited on a silicon wafer. After water evaporation, the samples were studied using a field emission scanning electron microscope (LEO 1550 FESEM).

Batch Experiments. Degradation of CIP and BPA was carried out in aluminum covered 20ml screw-top glass bottles under constant shaking at room temperature (22±1°C). Reaction pH was maintained with 10mM acetic acid/ sodium acetate for pH 5, and 4-morpholinepropanesulfonic acid (MOPS) and its sodium salt for pH 6 and 7, respectively. NaCl (0.01M) was also added to the solution. Reaction was initiated by adding the appropriate amount of Mn(III/IV) oxide suspension to the buffered solution with or without co-solutes and spiked with probes. Aliquots

were periodically withdrawn and reactions were quenched by ascorbic acid (0.1 M) addition which dissolves Mn(III/IV) oxide. All samples were analyzed within 24h. Control experiments with probe chemicals alone were conducted simultaneously with each batch of reaction. All experiments were carried out with replicates.

Chemical Analysis. Decrease in the concentrations of probe chemicals over time were determined using a reverse-phase high performance liquid chromatography (HPLC) equipped with a Restek ultra C18 (5 μ m) reverse phase column (4.6 \times 150 mm). The mobile phase was a mixture of methanol and water in ratios of 80:20 for BPA. A gradient elution was used for CIP analysis with the mobile phase consisting of methanol (eluent A) and 0.1% Formic Acid solution (eluent B) at a flow rate of 1ml / min. The injection volume was 25 μ l and the elution program was as follows: linear gradient from 85% B to 0% B in 12 minutes, 2 minute isocratic at 0% B, linear gradient to 85% B in 4 minute, followed by 2 minute isocratic at 85%B.

BPA and CIP were monitored with a fluorescence detector (HP series 1100, Agilent Technology). The excitation wavelengths (λ_{ex}) and emission wavelength (λ_{em}) were 278 and 450 nm for CIP, and 220 and 310 nm for BPA.

Degradation products of CIP were separated under the same gradient elution as described above and analyzed by HPLC-UV/MS. The MS spectra were obtained using an Agilent G1978B Multimode source for the 6100 series single-quadrupole MS in the positive ES mode with a full scan from m/z 100 to m/z 400 and a fragmentor of 120. The specific parameters set up for the mass detector were as follows: drying gas flow, 12 L min⁻¹; nebulizer pressure, 40 Psig; drying gas temperature, 300 °C; vaporizer temperature, 250 °C; capillary voltage, 2000 V; corona current, 4.0 μ A; and charging voltage, 2000 V.

Degradation products of BPA were analyzed by both HPLC-UV/MS and GC/MS. The LC elution was performed at 30 °C and a flow rate of 1 ml/min with solvent A (100% methanol) and solvent B (MilliQ + 0.1% formic acid). The injection volume was 25 µl and the elution program was as follows: 3 min isocratic at 80% B, linear gradient to 55% B in 9 min, followed 3min isocratic at 55% B, linear to 0% B in 15 min, linear to 80% B in 5 min and isocratic at 80% for 3 min. The MS spectra were obtained in the APCI positive mode with a full scan from m/z 100-500. All the other parameters for MS detector were set the same as that in the CIP experiment. For GC/MS analysis, the products in solution were extracted and enriched by solid phase extraction (SPE) via a C18 cartridge (C18 Sep Pak, waters). The cartridge was pre-conditioned by 3ml hexane, 3ml dichloromethane, followed by 6 ml methanol and 6 ml DI water. Elution was performed with pure methanol. Aliquots (5 µL) of the extract were analyzed on an Agilent 6890 gas chromatograph (GC) coupled with an Agilent 5973 mass spectrometer (MS) (Agilent Technologies, Wilmington, DE) for chemical structural analysis. A DB-5 capillary column (30 m × 0.25 mm × 0.25 µm; Agilent Technologies) was employed for separation. The inlet temperature was 310 °C, and the detector temperature was 310 °C. The oven temperature was initiated at 50 °C and held for 1 min, then increased to 140 °C at 10 °C/min and held for 3 min, then increased to 310 °C at 10 °C/min and held for 5min. The MS detector was operated in the electron impact mode with 70 eV of ionization energy, and the mass spectra were acquired in the scan mode with m/z ranging from 40 to 600.

Data Analysis. All of the figures and statistical analyses were completed using SigmaPlot 9.0.

Results and discussion

Characterization of Biogenic MnO_x and synthetic MnO₂. XRD analysis indicates that all three types of Mn(III/IV) oxide are poorly crystallized. The two biogenic Mn(III/IV) oxides

displayed two broad signature δ -MnO₂ peaks, with 2θ around 37° and 65° (**Figure 5.1**) (22). δ -MnO₂ is a hexagonal birnessite with the most extreme c axis disordering (23). The synthetic MnO₂ has two additional peaks that can be assigned to birnessite, at $2\theta \sim 43^\circ$ and 56° , which may be due to the increase of stacking order along the c axis (24). Diffraction peaks of BioMnO_x have the weakest intensity and removal of organic material by bleaching improved the intensity and shapes of the diffraction peaks.

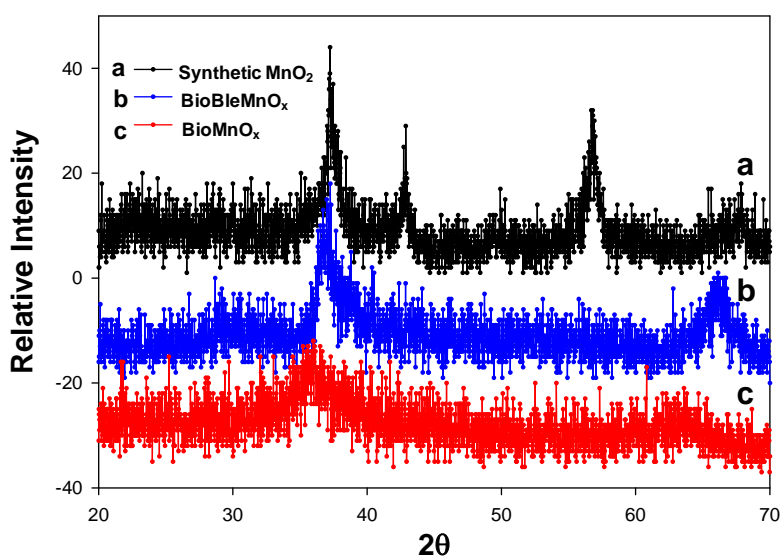


Figure 5.1 A XRD analysis of synthetic and biogenic Mn(III/IV) Oxides.

A morphological study by SEM showed that BioMnO_x is irregularly shaped with twisted sheets and a particle size of 2-3 μ M. Synthetic MnO₂ appears to be randomly stacked plates and has a much smaller particle size at ~ 200 nm (**Figure 5.2**). The bleaching process changed neither the morphology nor the particle size of BioMnO_x. N₂-BET surface area measurement demonstrated that synthetic MnO₂ has a much larger surface area than BioMnO_x, regular or bleach cleaned (**Table 5.1**). This measurement is consistent with the SEM observation on the particle size distribution.

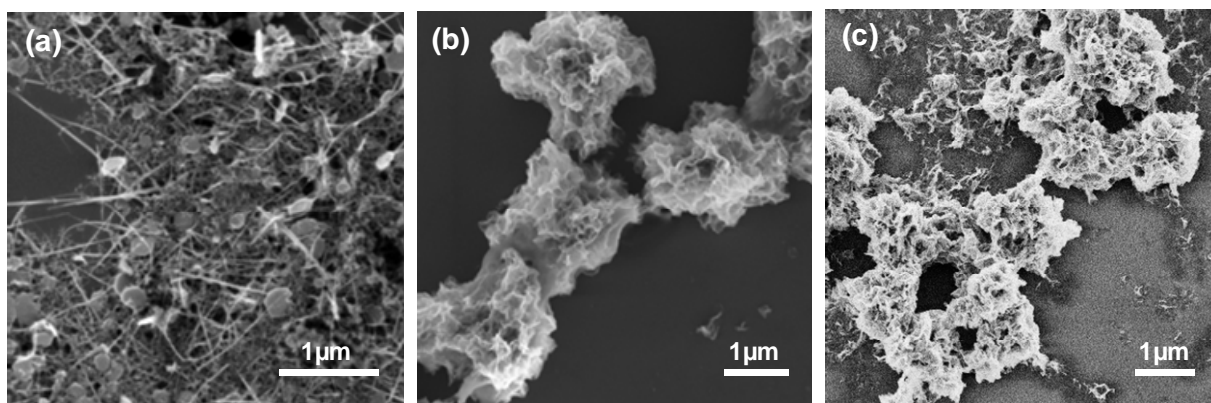


Figure 5.2 SEM micrographs of synthetic and biogenic Mn(III/IV) Oxides, (a) synthetic MnO₂; (b) BioMnO_x (c) BioBleMnO_x.

Table 5.1 Surface analysis of Mn(III/IV) oxides

Sample	Elemental composition					Surface Area (m ² /g)
	C(%)	N(%)	Mn(%)	O(%)	Na(%)	
BioMnO _x	46.65	7.14	9.25	37.17	-	57.37
BioBleMnO _x	22.75	--	21.39	51.73	4.13	54.74
Synthetic MnO ₂	29.15	--	19.45	51.39	-	155.35

The elemental composition of synthetic MnO₂, BioMnO_x and BioBleMnO_x was analyzed using XPS. The carbon content in BioMnO_x is much larger than that of the bleached oxide and the synthetic MnO₂. Another distinct difference is the presence of a significant fraction of N element in the BioMnO_x, which is expected to be from the MOF proteins and other organic metabolites. Bleaching of BioMnO_x leads to a total loss of the N element peak, indicating effective removal of organic debris in BioMnO_x.

The presence of a large fraction of organic materials is also confirmed by thermal gravimetric analysis (**Figure 5.3**). While synthetic MnO_2 and BioBle MnO_x had <15% weight loss, Bio MnO_x lost >40% of the weight during the heating process. This much larger total weight loss in Bio MnO_x is due to organic residue removal by heat. The weight loss curves also seem to have different patterns. BioBle MnO_x has a very similar curve to that of synthetic MnO_2 with two drops in weight. The first weight drop is probably due to loss of physical and chemically adsorbed water while the second drop is due to a mineral phase transition. For Bio MnO_x , the weight loss stages are less distinct and the phase transition weight drop is masked by the gradual organic decomposition.

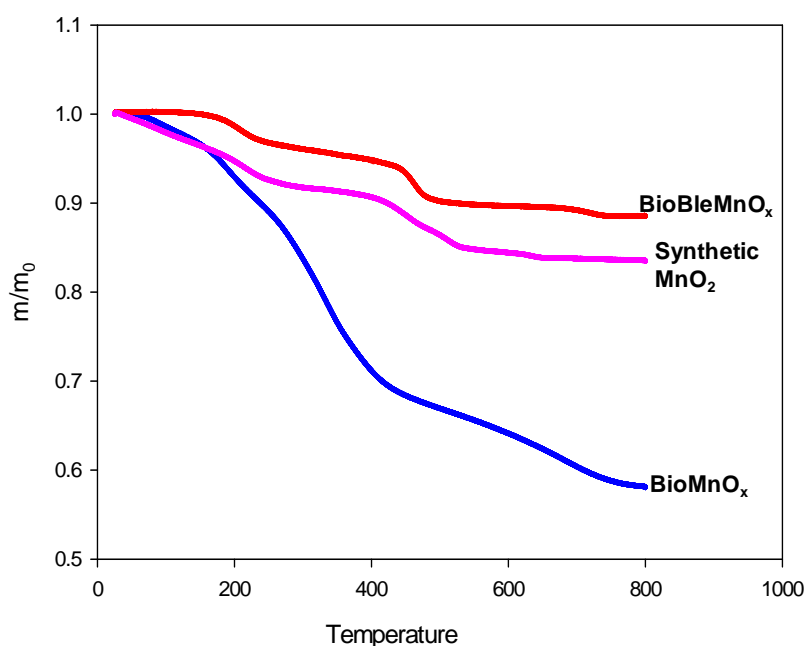


Figure 5.3 Thermal gravimetric analysis of biogenic and synthetic Mn(III/IV) oxides.

Efficacy of Contaminant removal by Biogenic MnO_x . In the absence of Bio MnO_x , both the contaminants, CIP and BPA, remained stable in water and no degradation was observed. When Bio MnO_x was added to the solution, contaminant removal was observed.

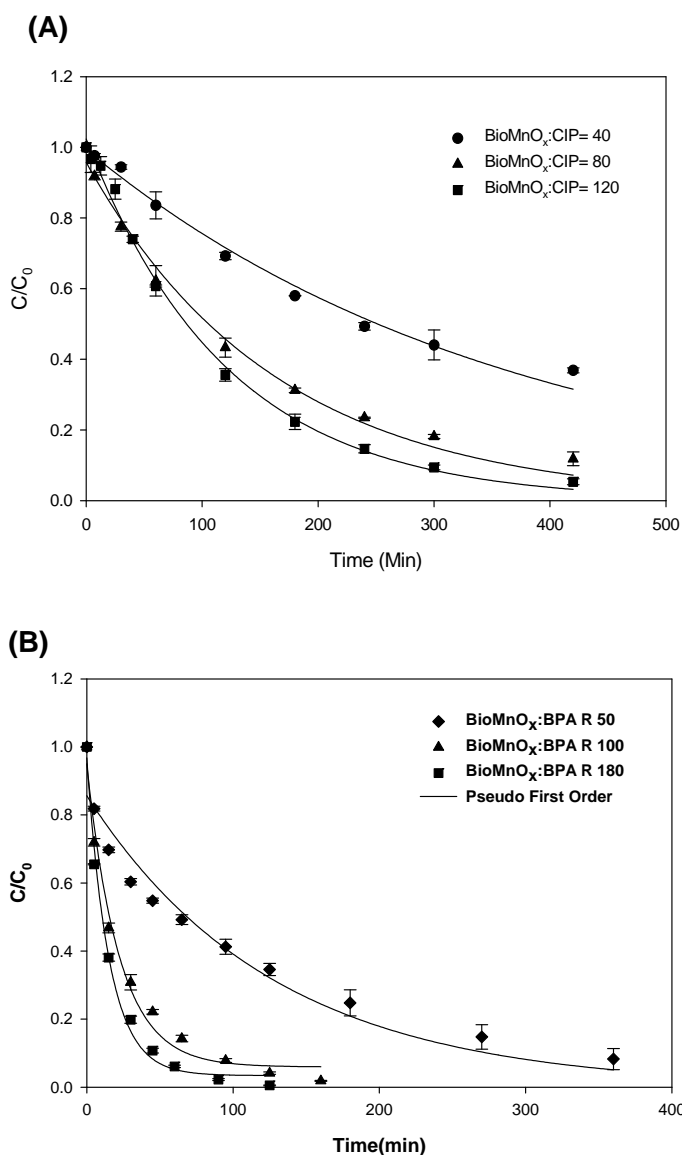


Figure 5.4 Degradation of CIP and BPA at pH 5 and different BioMnO_x dosages: **(A)** [CIP] = 5 μM, [BioMnO_x] = 200, 400, 600 μM; **(B)** [BPA] = 4.4 μM, [BioMnO_x] = 220, 440, 800 μM;

Typical time courses of CIP and BPA degradation at different BioMnO_x dosages are shown in **Figure 5.4**. For example, almost complete removal of CIP and BPA was achieved in hours. Increasing BioMnO_x dosage resulted in increased reaction rates and improved removal efficiency. Slow and limited removal rates were observed at lower BioMnO_x dosage which may be due to

the saturation of surface reactive sites on the oxidant. Generally, disappearance of CIP and BPA in presence of BioMnO_x indicates that biogenic manganese oxides can affect environmental fates of such xenobiotics and have a potential application for treating them in aqueous solution.

Kinetic comparison of BioMnO_x with synthetic MnO₂. The layer type synthetic MnO₂ is a justified structural model for BioMnO_x as suggested by X-ray absorption and X-ray diffraction studies (10, 14-17). Degradation kinetics of CIP and BPA by BioMnO_x were compared with that by synthetic MnO₂ (**Figure 5.5**). As shown in **Figure 5.5**, degradation rates are faster in the synthetic MnO₂ system over the pH range studied. For example, at the same oxidant to substrate ratio at pH 5, CIP was removed completely in 20 minutes by synthetic MnO₂ compared to 85% removal in 8 hours by BioMnO_x (**Figure 5.5**). The degradation data were fitted by pseudo first order kinetics and the rate constants were summarized in **Table 5.2**. Generally, discrepancy in reaction rates is more obvious toward the neutral pH condition, which was demonstrated in CIP degradation experiments. Acidifying the solution to pH 3, a condition that is favorable for oxidative reaction, did not eliminate the difference in reaction rates (data not shown).

However, different observations were reported in a diclofenac study with BioMnO_x produced by *P. putida* MnB6, another layer type BioMnO_x: comparing to the synthetic MnO₂, similar oxidation rates were found at pH 4.7 and a 10-fold faster oxidation rate by BioMnO_x was observed at neutral condition (5). The discrepancy between the results of the two studies may be explained by the difference in surface areas, average oxidation states (AOS) and the extent of microbial Mn(II) oxidizing activity. In the diclofenac study, the BioMnO_x has a surface area of 98 m²/g, close to that of synthetic MnO₂ (**Table 5.1**) (5). In contrast, the BioMnO_x produced by *L. Discophora* has a much smaller surface area at 57 m²/g (**Table 5.1**).

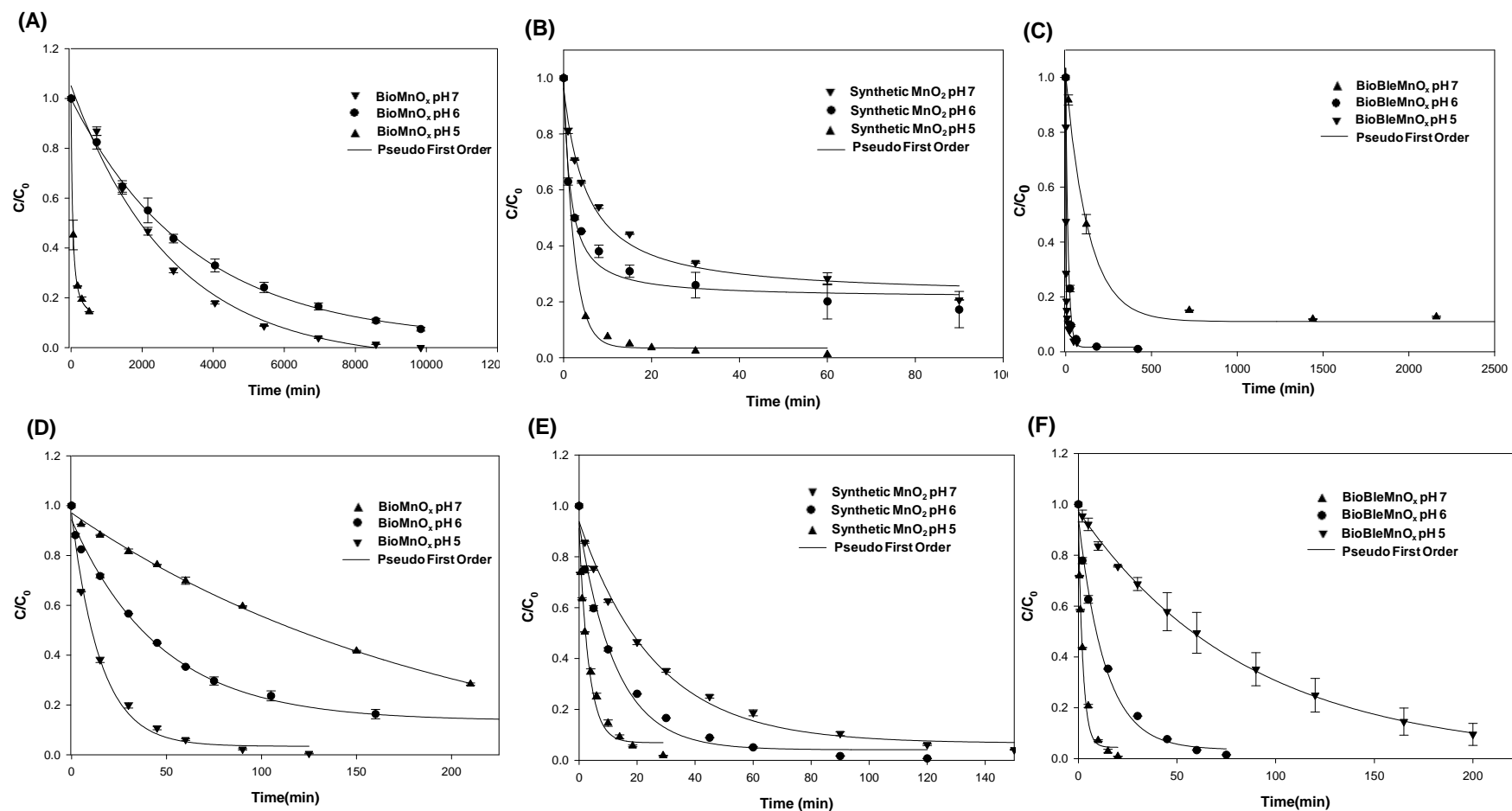


Figure 5.5 Degradation of CIP and BPA by Mn(III/IV) Oxides at pH 5-7, [HAc/NaAc]= [MOPS] = 10mM, A - C: CIP = 5 μ M, [BioMnO_x] = [synthetic MnO₂] = [BioBleMnO_x] = 0.24 mM; D – F: BPA = 4.4 μ M, [BioMnO_x] = [synthetic MnO₂] = [BioBleMnO_x] = 0.8 mM;

Table 5.2 Rate constants of CIP and BPA degradation by biogenic and synthetic Mn(III/IV) oxides at different pH conditions.

	k_{BioMnO_x}	$k_{\text{BioBleMnO}_x}$	$k_{\text{Synthetic MnO}_2}$	$\frac{k_{\text{BioMnO}_x}}{k_{\text{Synthetic MnO}_2}}$	$\frac{k_{\text{BioBleMnO}_x}}{k_{\text{Synthetic MnO}_2}}$
CIP					
pH = 5	7.60e-3	4.8e-1	4.17e-1	1.82%	115%
pH = 6	2.70e-4	3.6e-2	3.93e-1	0.0687%	9.16%
pH = 7	4.01e-4	6.4e-3	1.22e-1	0.329%	5.25%
BPA					
pH = 5	6.55e-2	3.74e-1	3.02e-1	21.7%	124%
pH = 6	2.15e-2	7.43e-2	7.87e-2	27.3%	94.4%
pH = 7	4.98e-3	1.18e-2	3.82e-2	13%	30.9%

*[CIP] = 5 μ M, [BioMnO_x] = [BioBleMnO_x] = 240 μ M; [BPA] = 4.4 μ M, [BioMnO_x] = [BioBleMnO_x] = 800 μ M; R² = 0.96-0.99, relative standard deviation (RSD) = 2.36 – 18.83% for CIP data and RSD = 6.1-11.4% for BPA data.

The average oxidation state (AOS) of manganese is a known important factor that affects the reactivity of manganese oxides (25). Generally, higher AOS is favorable for the oxidation process. It has been proposed that bacterial Mn(II) oxidation is a two step electron transfer process and Mn(III) is an intermediate (26). Considering the possibility of Mn(II) adsorption on the surface, the BioMnO_x is likely to be a mixture of Mn(II), Mn(III) and Mn(IV). A previous study indicated that newly formed BioMnO_x by *L. Discophora* has an AOS close to the oxidation state of Mn(III) (27). On the contrary, synthetic MnO₂ and BioMnO_x reported in the diclofenac study have an AOS close to 4 (13). Thus the lower activity of BioMnO_x observed in this study may be partially attributed to its lower AOS.

Lower microbial Mn(II) oxidizing activity in BioMnO_x in this study may also partially explain the lower oxidative reactivity. It is believed that microbial activity can remove inhibitory Mn(II) released during contaminant degradation and enhance the oxidative reaction (5). While microbial Mn(II) oxidizing activity is still present and highly active in the BioMnO_x pellets in the diclofenac study, it is likely to be negligible in this study due to either BioMnO_x coating on MOF, thus blocking the reactive enzyme center, or inactivation of MOF during the clean up step.

It is noted that surface adsorbed Mn(II) can also lead to an inhibition of oxidation due to its binding with the surface reactive sites (5, 8). Such inhibitory effect is reported to be partially the reason for instability of treatment efficiency observed in a Mn(II) oxidizing bioreactor (28). However, Mn(II) adsorption seems to be a very minor reason in the current BioMnO_x system because the percentage of adsorption on BioMnO_x is small (< 7%) and the cleaning step using diluted HCl further removes adsorbed Mn(II) by a cation exchange process (29).

Particle size is another important factor that determines oxidative reactivity of manganese oxide. Much faster Cr (III) oxidation was reported in the presence of colloidal MnO₂ compared to the bulkier counterpart (30). The colloidal fraction, defined as the suspension that passes through a 0.22µm membrane filter, was measured by an LBB assay for both BioMnO_x and synthetic MnO₂ (minimal quantification amount is 4 µM MnO₂). While a significant fraction of reactive Mn in synthetic MnO₂ exists in colloidal form (~30%) there is negligible colloidal reactive Mn in BioMnO_x (< 2%) either during formation or after cleaning. Therefore, the presence of an appreciable colloidal fraction in synthetic MnO₂ may be a major reason for the significantly faster reaction rate.

The mechanism of how organic residuals affect BioMnO_x reactivity is not clear. It may play a dual role in the reaction. It may bind with the oxide and limit the accessibility of the reactive

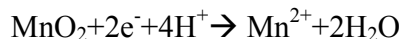
sites to the substrate, resulting in retarded reaction rates. Bleaching was used to remove the organic fraction in BioMnO_x , generating BioBleMnO_x . The BioMnBleO_x seems to be similar to synthetic MnO_2 , as indicated by XRD and TGA results. Degradation experiments were also carried out using BioBleMnO_x . A significant improvement in reaction rates was observed (**Figure 5.5, Table 5.2**). The still slower degradation rates compared to synthetic MnO_2 may be due to the smaller surface area of BioBleMnO_x (**Table 5.1**). It should be noted that bleaching may also have changed the AOS of BioMnO_x since both BioBleMnO_x and synthetic MnO_2 are expected to have an AOS close to 4 (13). Thus the improvement in initial oxidation rates by bleaching is likely to be a combination effect of AOS increase and organic debris removal.

The organic residual may also act as a ligand and chelate with the Mn(II) , preventing it from competing for the reactive sites. The ligand binding effect is suggested by the observation that CIP was slowly yet completely removed by BioMnO_x at pH 7 whereas the removal was halted at 85% by BioBleMnO_x despite the much faster initial reaction rate. The inhibition observed in the BioBleMnO_x system, as the reaction progressed, may be due to the accumulation of adsorbed Mn(II) . On the contrary, in BioMnO_x system, organic chelating may help to reduce the inhibition and leads to a more complete oxidation.

Based on the above observation and discussion, caution should be taken when making predictions of BioMnO_x oxidative reactivity based on the results from the synthetic MnO_2 model.

Effects of pH. Removal rates of CIP and BPA were examined at different environmentally relevant pH conditions, ranging from pH 5 to pH 7. Generally the degradation rate constants are always higher in the BioBleMnO_x system at each pH condition studied. Given the same substrate and oxidant, fastest rate constants were observed at pH 5. This is expected because a proton is a

constituent of the reaction and increase of proton concentration will increase the driving force for the reaction.



Unidirectional pH dependence of rate constants was observed in CIP degradation by BioBleMnO_x and in the BPA degradation in both the BioMnO_x and BioBleMnO_x systems, where the oxidizing potential of Mn(III/IV) oxides may be the dominant factor.

It is interesting to note that a different pH dependence pattern was observed in CIP degradation experiments by BioMnO_x at near neutral pH conditions, with $k_{\text{pH}=7, \text{BioMnO}_x} > k_{\text{pH}=6, \text{BioMnO}_x}$. Another two separate experiments with replicates also demonstrated similar pH dependence pattern with more removal of CIP at pH7. This indicates other factors other than manganese oxidizing potential may play a role in the degradation process. In contrast, rate constants of CIP degradation by both BioBleMnO_x and synthetic MnO₂ still follow the decreasing trend of *k* as pH increases: $k_{\text{pH}=7} < k_{\text{pH}=6}$ (**Table 5.2**) (31). Thus the change of *k* order at pH 6-7 by BioMnO_x treatment is likely due to the interaction between the biological component and Mn(II) although the mechanism remains unclear. Possible explanations include residual microbial activity which is more active at pH 7 than 6 or stronger chelating with Mn(II) at pH 7.

Effects of co-solutes. The degradation rate constants of both CIP and BPA in the presence of co-solutes are summarized in **Table 5.3**. Generally, degradation of CIP and BPA are inhibited by co-existing metal cations. At the pH range studied, the manganese oxide surface is expected to be negative (5, 32). Thus metal cations can bind to the surface by electrostatic interaction and compete for the reactive sites. The inhibitory extent correlates with the adsorption affinity of the cations reported in the literature with $[\text{Mg}^{2+}] > [\text{Ca}^{2+}] > [\text{Cu}^{2+}] > [\text{Mn}^{2+}]$ (33, 34). Similar inhibitory trends have also been reported in synthetic manganese oxide systems (35, 36).

Interestingly, it seems that oxidation rates by BioMnO_x were suppressed to a less extent, compared to those by BioBleMnO_x. This may be due to chelating of the added metal cations by organic residual in BioMnO_x.

Humic acid (HA) is naturally occurring organic matter in the aquatic environment that may affect oxidation reactivity of BioMnO_x. Humic acid can adsorb on the oxidant surface and block the reactive site, leading to a lower removal efficiency. However, enhancement of the oxidative reaction may also occur, which is demonstrated in the 17β-estradiol oxidation study (36). The facilitation of oxidative degradation is due to the chelating of the released Mn(II) ion during the reaction and subsequently reduced auto-inhibition. Therefore the net effects of HA on the degradation kinetics is a result of the combination of those two countering effects and no general trend can be concluded. As shown in **Table 5.3**, low concentration of HA (1mg/L) does not seem to cause a significant change in the rate constants except for that of CIP degradation by BioBleMnO_x. Further increasing HA concentration (10mg/L) resulted in more significant change in oxidation rate constants, and effects vary among each treatment group.

Table 5.3 Rate constants of CIP and BPA degradation in presence of co-solutes by BioMnO_x and BioBleMnO_x*

	BioMnO _x		BioBleMnO _x	
	k	k/k _{ctrl}	k	k/k _{ctrl}
CIP(Ctrl)	7.60e-3	100%	4.80e-1	100%
Ca ²⁺	2.93e-3	38.6%	3.36e-2	7%
Mg ²⁺	4.55e-3	59.9%	1.36e-1	28.3%
Mn ²⁺	1.74 e-4	2.29%	3.78e-4	0.0788%
Cu ²⁺	9.13e-4	12.0%	3.95e-4	0.0823%
1mg/L HA	7.15e-3	94.1%	8.79e-1	183%
10 mg/LHA	3.18e-3	41.8%	9.62e-1	200%
BPA(Ctrl)	7.05e-3	100%	4.84e-1	100%
Ca ²⁺	7.01e-3	99.4%	3.24e-1	66.9%
Mg ²⁺	6.87e-3	97.4%	2.95e-1	61%
Mn ²⁺	2.97e-3	42.1%	6.36e-2	13.1%
Cu ²⁺	6.4e-3	90.8%	1.48e-1	30.6%
1 mg/L HA	7.58e-3	108%	3.68e-1	76%
10mg/L HA	8.41e-3	119%	2.88e-1	59.5%

*[CIP] = 5μM, [BioMnO_x] = [BioBleMnO_x] = 240μM; [BPA] = 4.4μM, [BioMnO_x] = [BioBleMnO_x] = 800 μM; pH = 5; [Ca²⁺] = [Mg] = [Cu] = 10 mM, [Mn²⁺] = 1mM. R² = 0.83 - 0.99 except for data fitting of CIP degradation with addition of Cu²⁺ and Mn²⁺ (R² = 0.61-0.71). RSD = 4.23-33.4% for CIP data and RSD = 6.27 – 19.7% for BPA data.

Degradation products and mechanisms. Degradation products of CIP were analyzed by identifying the $[M+H^+]$ molecular ions in the positive mode using HPLC/MS. Compared to the synthetic MnO_2 system, fewer degradation products were observed, with two major peaks with $[M+H^+]$ ions of m/z 306 and 263 and two minor peaks with $[M+H^+]$ ions of m/z 364 and 362 (31). The retention time and spectrum of degradation products detected in this study were compared to those discussed and reported in the AFT and cryptomelane systems (37, 38). Proposed structures are shown in **Table 5.4**.

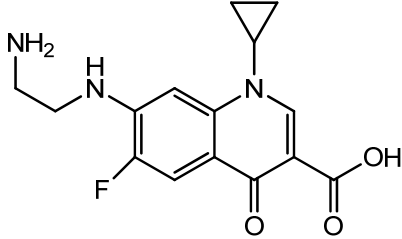
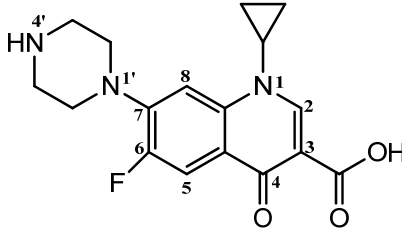
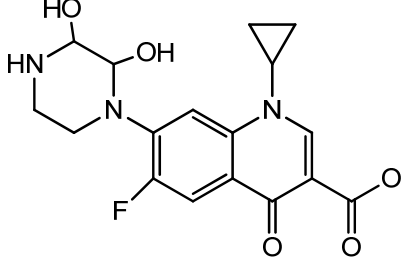
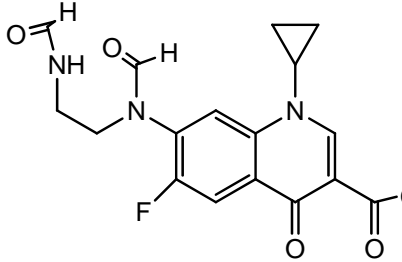
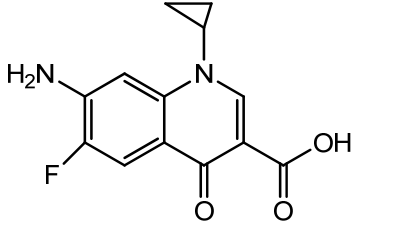
The piperazine ring of fluoroquinolone antibiotics is believed to be the site susceptible to oxidation (31, 39). A kinetic study in the synthetic MnO_2 system further points out that the two nitrogen atoms (N1' and N4') are reactive sites that control the reaction rates (31). The iminium ion species forms after the electron transfer from the N atom to the Mn(III/IV) reactive center. Hydrolysis of the iminium species leads to the opening of the piperazine ring and loss of alkyl groups on the N atoms (**Figure 5.6**). Thus, this pathway is known as the N-dealkylation pathway. The species m/z 306 is believed to be formed via this hydrolysis-dealkylation process by loss of the ethylene group. The same product m/z 306 also appears as the first product in the cryptomelane system (discussed in Chapter 3), indicating that the N-dealkylation process is favorable in the manganese oxide system. The two nitrogen atoms (N1' and N4') in desethylene CIP can undergo similar electron transfer, leading to the formation of another iminium species that is susceptible to hydrolysis. As a result, a complete dealkylated product will be formed, which is expected to be the species m/z 263.

In addition to the hydrolysis and piperazine ring opening of the iminium species, hydroxylation on the carbon atom of the C=N bond can also take place, yielding the species m/z 364 (**Figure 5.6**). This pathway is known as C-hydroxylation. The species m/z 362 is likely to be

a downstream product of the species m/z 364 via further oxidation. It appeared later than the species m/z 364 in the system and seemed to exist in even smaller amounts as indicated by both UV and MS intensity (data now shown). The two other degradation products reported in δ - MnO_2 and cryptomelane systems, the species m/z 334, were not observed in this study, although the possibility of presence in trace amount cannot be ruled out (31).

Generally, all the transformation takes place in the piperazine ring of CIP by $BioMnO_x$ oxidation while the quinolone core structure remains. While destruction of the piperazine ring is expected to reduce the potency of the antibiotic activity, residual biological activity may still exist (40). Bioassays using sensitive organisms are suggested to further evaluate this treatment method.

Table 5.4 Proposed structures of degradation products of CIP

Retention Time	Molecular Ion(M+H ⁺)	Proposed Molecule Structure
9.81	306	 <chem>NCNc1cc(F)c2c(=O)c(C(=O)O)c(C3CC3)n12</chem>
10.1	CIP 332	 <chem>C1CCN1c2cc(F)c3c(=O)c(C(=O)O)c(C4CC4)n23</chem>
11.41	364	 <chem>OCC(O)Nc1cc(F)c2c(=O)c(C(=O)O)c(C3CC3)n12</chem>
12.62	362	 <chem>NC(=O)CNc1cc(F)c2c(=O)c(C(=O)O)c(C3CC3)n12</chem>
14.3	263	 <chem>Nc1cc(F)c2c(=O)c(C(=O)O)c(C3CC3)n12</chem>

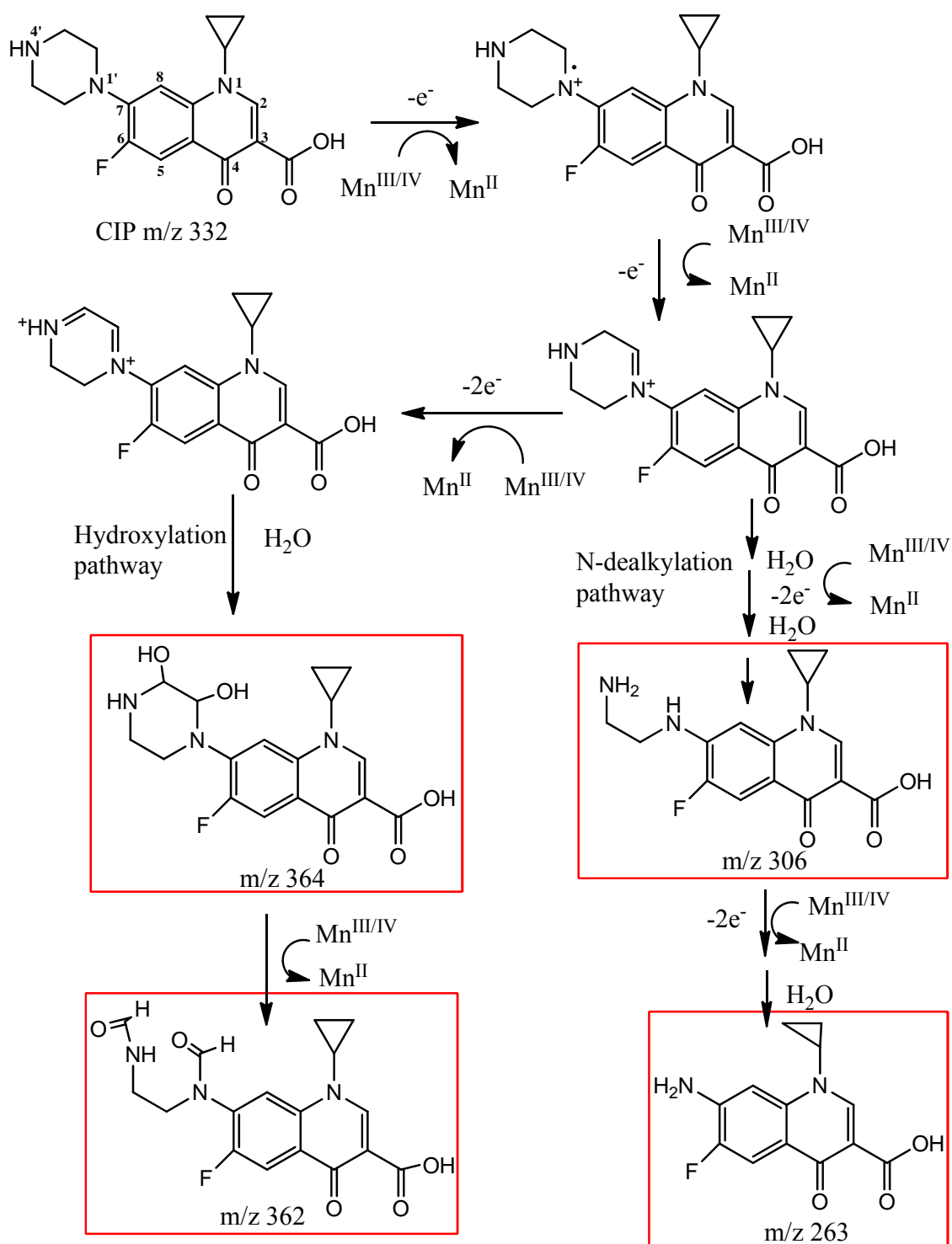


Figure 5.6 Degradation pathways of CIP by BioMnO_x

Degradation products of BPA were analyzed by both LC/MS and GC/MS. To obtain the maximum amount of products, BioMnO_x was totally dissolved by ascorbic acid and any products adsorbed were released into the solution. Silylation was also performed with the solid phase extract to improve the detection. Despite all these efforts, only one product, with an apparent molecular weight of 134, was found by both LC/MS and GC/MS. Silylation derivative of this product was not observed, indicating absence of reactive H in this species. The mass spectrum and proposed structure is given in **Figure 5.7**. The same degradation product was also reported in a δ -MnO₂ system (41).

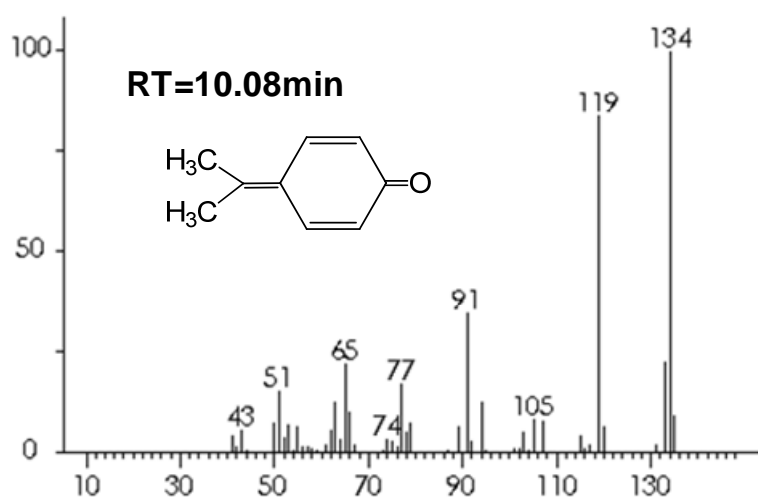


Figure 5.7 Mass spectrum of BPA degradation product analyzed by GC/MS

As proposed in **Figure 5.8**, BPA oxidation is initiated by transferring an electron to the oxide, forming a BPA radical. The unpaired electron can be delocalized by resonance, forming BPA radical 2. Further radical fragmentation via beta scission yields product m/z 134 (41). This product is likely to be less estrogenic due to loss of the phenolic group, a key structural feature for mimicking estrogen, and increase of polarity (42).

It is interesting to note that a yellow precipitate was observed to form as the oxidation progressed. The precipitate was probably formed via polymerization by radical coupling. Yet the nature and structure of such products remains unclear.

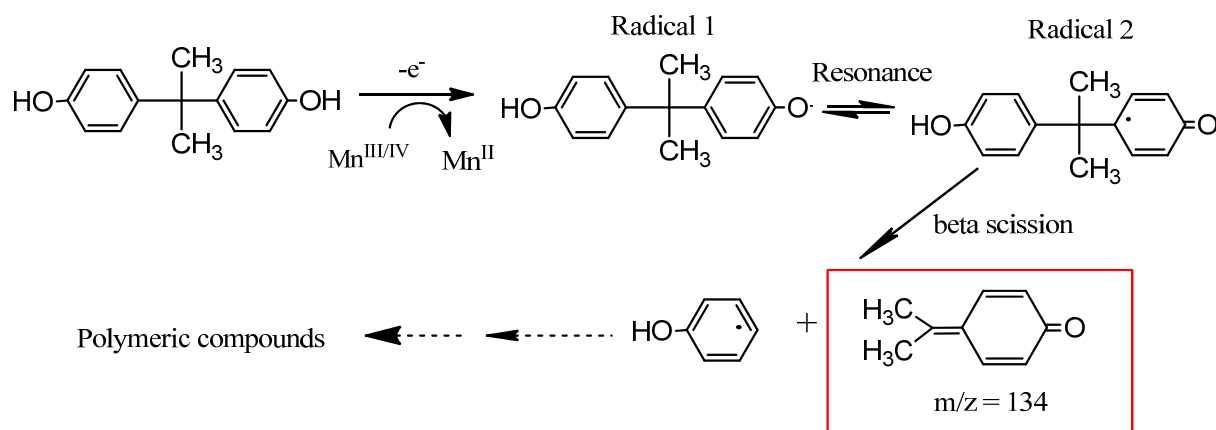


Figure 5.8 Proposed degradation pathway of BPA by BioMnO_x

This is the first study that compares degradation products in biogenic and synthetic manganese oxide systems. Generally, fewer degradation products were observed in the BioMnO_x system. Future research is needed to explain the preference of degradation pathways and different product distribution in the BioMnO_x system.

Conclusion

Successful removal of CIP and BPA can be achieved in the BioMnO_x system although degradation kinetics is generally slower than in synthetic MnO₂ system. The lower oxidative reactivity may be attributed to a smaller surface area, larger particle size, lower AOS and blocking of reactive sites by organic residual. The pH condition was found to affect the oxidation kinetics significantly. Generally lower pH is favorable for the oxidative degradation. Metal cations inhibited the oxidation by competitively binding with the reactive surface sites. Humic acid can affect oxidative degradation via two countering effects: blocking of surface reactive

sites which reduces reactivity and binding inhibitory MnII ion released during the reaction which accelerates the reaction. Oxidative degradation of CIP by BioMnO_x was mainly via N-dealkylation. BPA underwent a radical fragmentation and further complicated radical couplings, yielding an olefin product and polymerized precipitate. Generally, based on the proposed structure of degradation products, lower biological activity of the solution is expected after the treatment.

References

1. He, J.; Meng, Y.; Zheng, Y.; Zhang, L. Cr(III) oxidation coupled with Mn(II) bacterial oxidation in the environment. *Journal of Soils and Sediments* 2010, 10, 767-773.
2. Lafferty, B.J.; Ginder-Vogel, M.; Zhu, M.; Livi, K.J.T.; Sparks, D.L. Arsenite Oxidation by a Poorly Crystalline Manganese-Oxide. 2. Results from X-ray Absorption Spectroscopy and X-ray Diffraction. *Environ. Sci. Technol.* 2010, 44, 8467-8472.
3. McBride, M. Adsorption and oxidation of phenolic compounds by iron and manganese oxides. *Soil Sci. Soc. Am. J.* 1987, 51, 1466-1472.
4. Ouvrard, S.; Simonnot, M.O.; Sardin, M. Reactive behavior of natural manganese oxides toward the adsorption of phosphate and arsenate. *Ind Eng Chem Res* 2002, 41, 2785-2791.
5. Forrez, I.; Carballa, M.; Verbeken, K.; Vanhaecke, L.; M.S.; Ternes, T.; Boon, N.; Verstraete, W. Diclofenac Oxidation by Biogenic Manganese Oxides. *Environ. Sci. Technol.* 2010, 44, 3449-3454.
6. Chen, W.; Ding, Y.; Johnston, C.T.; Teppen, B.J.; Boyd, S.A.; Li, H. Reaction of Lincosamide Antibiotics with Manganese Oxide in Aqueous Solution. *Environ. Sci. Technol.* 2010, 44, 4486-4492.
7. Shin, J.Y. and Cheney, M.A. Abiotic transformation of atrazine in aqueous suspension of four synthetic manganese oxides. *Colloids Surf. Physicochem. Eng. Aspects* 2004, 242, 85-92.

8. Zhang, H. and Huang, C.H. Oxidative transformation of triclosan and chlorophene by manganese oxides. *Environ. Sci. Technol.* 2003, 37, 2421-2430.
9. Diem, D. and Stumm, W. Is dissolved Mn^{2+} being oxidized by O_2 in absence of Mn-bacteria or surface catalysts? *Geochim. Cosmochim. Acta* 1984, 48, 1571-1573.
10. Tebo, B.M.; Bargar, J.R.; Clement, B.G.; Dick, G.J.; Murray, K.J.; Parker, D.; Verity, R.; Webb, S.M. Biogenic manganese oxides: properties and mechanisms of formation. *Annu. Rev. Earth Planet. Sci.* 2004, 32, 287-328.
11. Fuller, C.C. and Harvey, J.W. Reactive uptake of trace metals in the hyporheic zone of a mining-contaminated stream, Pinal Creek, Arizona. *Environ. Sci. Technol.* 2000, 34, 1150-1155.
12. Kay, J.T.; Conklin, M.H.; Fuller, C.C.; O'Day, P.A. Processes of nickel and cobalt uptake by a manganese oxide forming sediment in Pinal Creek, Globe Mining District, Arizona. *Environ. Sci. Technol.* 2001, 35, 4719-4725.
13. Villalobos, M.; Toner, B.; Bargar, J.; Sposito, G. Characterization of the manganese oxide produced by pseudomonas putida strain MnB1. *Geochim. Cosmochim. Acta* 2003, 67, 2649-2662.
14. Villalobos, M.; Bargar, J.; Sposito, G. Mechanisms of Pb (II) sorption on a biogenic manganese oxide. *Environ. Sci. Technol.* 2005, 39, 569-576.
15. Saratovsky, I.; Wightman, P.G.; Pasten, P.A.; Gaillard, J.; Poeppelmeier, K.R. Manganese oxides: Parallels between abiotic and biotic structures. *J. Am. Chem. Soc.* 2006, 128, 11188-11198.
16. Jurgensen, A.; Widmeyer, J.R.; Gordon, R.A.; Bendell-Young, L.I.; Moore, M.M.; Crozier, E.D. The structure of the manganese oxide on the sheath of the bacterium *Leptothrix discophora*: An XAFS study. *Am. Mineral.* 2004, 89, 1110.

17. Nelson, Y.M.; Lion, L.W.; Ghiorse, W.C.; Shuler, M.L. Production of biogenic Mn oxides by *Leptothrix discophora* SS-1 in a chemically defined growth medium and evaluation of their Pb adsorption characteristics. *Appl. Environ. Microbiol.* 1999, *65*, 175.
18. Tani, Y.; Ohashi, M.; Miyata, N.; Seyama, H.; Iwahori, K.; Soma, M. Sorption of Co (II), Ni (II), and Zn (II) on biogenic manganese oxides produced by a Mn-oxidizing fungus, strain KR21-2. *Journal of Environmental Science and Health, Part A* 2005, *39*, 2641-2660.
19. Adams, L. and Ghiorse, W.C. Characterization of extracellular Mn²⁺-oxidizing activity and isolation of an Mn²⁺-oxidizing protein from *Leptothrix discophora* SS-1. *J. Bacteriol.* 1987, *169*, 1279-1285.
20. Villalobos, M.; Toner, B.; Bargar, J.; Sposito, G. Characterization of the manganese oxide produced by *Pseudomonas putida* strain MnB1. *Geochim. Cosmochim. Acta* 2003, *67*, 2649-2662.
21. Murray, J.W. The surface chemistry of hydrous manganese dioxide. *J. Colloid Interface Sci.* 1974, *46*, 357-371.
22. Grangeon, S.; Manceau, A.; Guilhermet, J.; Gaillot, A.C.; Lanson, M.; Lanson, B. Zn sorption modifies dynamically the layer and interlayer structure of vernadite. *Geochim. Cosmochim. Acta* 2012,
23. Saratovsky, I.; Wightman, P.G.; Pastén, P.A.; Gaillard, J.F.; Poepelmeier, K.R. Manganese oxides: Parallels between abiotic and biotic structures. *J. Am. Chem. Soc.* 2006, *128*, 11188-11198.
24. Ching, S.; Petrovay, D.J.; Jorgensen, M.L.; Suib, S.L. Sol-gel synthesis of layered birnessite-type manganese oxides. *Inorg. Chem.* 1997, *36*, 883-890.

25. Liu, C.; Zhang, L.; Li, F.; Wang, Y.; Gao, Y.; Li, X.; Cao, W.; Feng, C.; Dong, J.; Sun, L. Dependence of Sulfadiazine Oxidative Degradation on Physicochemical Properties of Manganese Dioxides. *Ind Eng Chem Res* 2009, *48*, 10408-10413.
26. Webb, S.M.; Dick, G.J.; Bargar, J.R.; Tebo, B.M. Evidence for the presence of Mn (III) intermediates in the bacterial oxidation of Mn (II). *Proc. Natl. Acad. Sci. U. S. A.* 2005, *102*, 5558.
27. Adams, L.F. and Ghiorse, W.C. Oxidation state of Mn in the Mn oxide produced by *Leptothrix discophora* SS-1. *Geochim. Cosmochim. Acta* 1988, *52*, 2073-2076.
28. Forrez, I.; Carballa, M.; Noppe, H.; De Brabander, H.; Boon, N.; Verstraete, W. Influence of manganese and ammonium oxidation on the removal of 17 [α]-ethinylestradiol (EE2). *Water Res.* 2009, *43*, 77-86.
29. Gheriany, I.A.E. Mn(II) OXIDATION BY LEPTOTHRIX DISCOPHORA SS-1. *Ph. D thesis* 2010,
30. Murray, K.J. and Tebo, B.M. Cr(III) is indirectly oxidized by the Mn(II)-Oxidizing bacterium *Bacillus* sp strain SG-1. *Environ. Sci. Technol.* 2007, *41*, 528-533.
31. Zhang, H. and Huang, C.H. Oxidative transformation of fluoroquinolone antibacterial agents and structurally related amines by manganese oxide. *Environ. Sci. Technol.* 2005, *39*, 4474-4483.
32. Kosmulski, M. The pH-Dependent Surface Charging and the Points of Zero Charge. *J. Colloid Interface Sci.* 2002, *253*, 77-87.
33. Tonkin, J.W.; Balistrieri, L.S.; Murray, J.W. Modeling sorption of divalent metal cations on hydrous manganese oxide using the diffuse double layer model. *Appl. Geochem.* 2004, *19*, 29-53.
34. Posselt, H.S.; Anderson, F.J.; Weber, W.J. Cation sorption on colloidal hydrous manganese dioxide. *Environ. Sci. Technol.* 1968, *2*, 1087-1093.

35. Lin, K.; Liu, W.; Gan, J. Oxidative removal of bisphenol A by manganese dioxide: efficacy, products, and pathways. *Environ. Sci. Technol.* 2009, *43*, 3860-3864.
36. Xu, L.; Xu, C.; Zhao, M.; Qiu, Y.; Sheng, G.D. Oxidative removal of aqueous steroid estrogens by manganese oxides. *Water Res.* 2008, *42*, 5038-5044.
37. Xiao, X.; Zeng, X.; Lemley, A.T. Species-dependent degradation of ciprofloxacin in a membrane anodic Fenton system. *J. Agric. Food Chem.* 2010,
38. Xiao, X.; Sun, S.P.; McBride, M.B.; Lemley, A.T. Degradation of ciprofloxacin by cryptomelane-type manganese (III/IV) oxides. *Environmental Science and Pollution Research* 2012, 1-12.
39. Wang, P.; He, Y.L.; Huang, C.H. Oxidation of fluoroquinolone antibiotics and structurally related amines by chlorine dioxide: Reaction kinetics, product and pathway evaluation. *Water Res.* 2010, *44*, 5989-5998.
40. Domagala, J.M. Structure-activity and structure-side-effect relationships for the quinolone antibacterials. *J. Antimicrob. Chemother.* 1994, *33*, 685.
41. Lin, K.; Liu, W.; Gan, J. Reaction of tetrabromobisphenol A (TBBPA) with manganese dioxide: kinetics, products, and pathways. *Environ. Sci. Technol.* 2009, *43*, 4480-4486.
42. Fang, H.; Tong, W.; Shi, L.M.; Blair, R.; Perkins, R.; Branham, W.; Hass, B.S.; Xie, Q.; Stacy, L.; Moland, C.L. Structure-activity relationships for a large diverse set of natural, synthetic, and environmental estrogens. *Chem. Res. Toxicol.* 2001, *14*, 280-294.

CHAPTER 6

CONCLUSIONS AND RECOMMENDATIONS FOR FURTHER RESEARCH

This thesis aimed to explore effective oxidation treatment methods for removing emerging contaminants from aqueous solution. Ciprofloxacin, a widely used fluoroquinolone antibiotic and bisphenol A, a known endocrine disrupter, were selected as the probe chemicals. Three types of oxidation treatment, anodic Fenton treatment (AFT), cryptomelane and its doped derivatives, and biogenic manganese oxides produced by *L. discophora SS-1*, were investigated.

Degradation kinetics were discussed and modeled in each oxidation system. In the AFT system, removal of CIP was generally fast, with complete removal in minutes. However, previous well established kinetic models in AFT systems were found to be deficient in characterizing the kinetics. Since a fitted kinetic model is important for predicting the treatment efficiency and determining the treatment time, efforts were made to understand the kinetic deviation and develop a new model for improved fitting. It was found that the speciation distribution of CIP changed over the AFT process, since pH is self-optimized to an acidic condition, leading to a change in apparent reaction affinity toward the OH radicals. Reduced reaction affinity due to protonation has also been observed by others in ozonation and manganese oxide studies (1, 2). The AFT process was optimized at pH 3.2, a favorable condition for the Fenton reaction, and an optimal $[\text{H}_2\text{O}_2]: [\text{Fe}^{2+}]$ ratio was found between 10 and 15. In the cryptomelane and biogenic manganese oxide systems, it was found that the kinetics can be approximated by a pseudo-first order at the initial reaction stage. As the reaction progresses, due to the shift in the Mn reactive site distribution, the oxidation slows down and deviates from first order. Optimization studies indicated that lower pH is favorable for the oxidation. This is because the proton is participating in the oxidation and the oxidizing potential of the oxide surface increases at lower pH. It is

noteworthy that the pH effects on degradation kinetics may not be linear in manganese oxide systems at circum-neutral conditions. This result could be due to reaction affinity changes due to some complicating factors in the system, such as the chelating of organic residual in the BioMnO_x.

Degradation products were analyzed, and the mechanisms involved in each system were discussed. In the AFT system, CIP was attacked by OH radicals and both the quinolone ring core structure and the piperazine ring were susceptible to oxidation. Various degradation products were observed and the degradation pathways are summarized as: <1> hydroxylation and defluorination on the aromatic ring; <2> oxidative decarboxylation; and <3> oxidation on the piperazine ring and N-dealkylation. The OH radical is such a strong non-selective oxidant that by the end of AFT treatment, CIP and its degradation products were removed to below detection level. Therefore, it is expected that antibacterial activity of the solution was successfully treated. Selective oxidation takes place in the cryptomelane and BioMnO_x systems. Only the piperazine ring of CIP, more specifically, the two N atoms on the ring, are the susceptible sites. Electron transfer from the N atom to reactive Mn(III/IV) center leads to formation of the iminium species which can undergo either hydroxylation or hydrolysis and dealkylation. The quinolone ring was found to be retained in the structure of the degradation products. Similar products were found in the BioMnO_x system except for the difference in product distribution. The N-dealkylation pathway seems to be favored in the BioMnO_x system. Degradation of BPA in the BioMnO_x system also yields fewer products than in the synthetic manganese oxide system. Meanwhile, yellow precipitates were observed, which is likely due to polymerization.

It should be noted that since manganese oxide is a selective oxidant, the treatment may leave the biologically functional groups unattacked, as seen in CIP degradation experiments, resulting

in a possible reduction of treatment efficiency. In addition, for biologically active contaminants, such as pharmaceuticals and EDCs, structure analysis is not sufficient to evaluate the treatment efficiency. Bioassays that target for the sensitive endpoints should be used for more thorough evaluation.

Attention should also be paid to avoiding potential secondary pollution when designing a water treatment process. For example, the classic Fenton system generates ferric sludge that requires further treatment while the AFT system efficiently reduces waste generation by its self-developed acidic condition. Precautions should be taken when using manganese oxides for treatment due to the potential release of Mn(II) during the redox reaction. Mn(II) oxidizing bacteria seem to open a prospective window for this application where Mn(II) oxidation and reoxidation can be coupled with the contaminant degradation. However, it is still very challenging to build a reliable bioreactor for water treatment based on current knowledge.

The Mn(II) oxidation mechanism is still under active research and not well understood. Efforts were made in this study to provide some perspectives on Mn(II) oxidation in the *L. discophora* SS-1 system using biochemical approaches. Peak MOF activity was found to be in the early stationary phase and optimal Mn(II) concentration for MOF activity was between 75 and 125 μM . The indirect enzymatic oxidation pathway via superoxide found in a marine bacterium does not seem to be involved here. The Mn(II) oxidation by MOF is sensitive to various chemical inhibitors that are likely to be present in the complicated wastewater matrix. A screening study revealed that MOF is sensitive to the presence of pyrophosphate, tetracycline and aminoglycoside antibiotics. While pyrophosphate may inhibit BioMnO_x formation via trapping Mn(III) and limiting the accessibility of Mn(II) and Mn(III) to the enzyme site, the inhibition mechanisms of the antibiotics remains unclear. A redox reaction between antibiotics and

BioMnO_x does not seem to be the major reason for the inhibition observed. Further research that utilizes a reliable genetic system of *L. discophora* SS-1 will assist in understanding MOF properties and its mechanisms.

Another challenge for making use of the Mn(II) oxidizing bacteria for water treatment is the lower reactivity of BioMnO_x compared to its synthetic counterparts as observed in this and other studies (3). In addition, aging of BioMnO_x may lead to changes in oxidative reactivity as well, raising another question regarding the reliability of the BioMnO_x-bacteria system (4). Long-term real wastewater tests instead of batch experiments on Mn oxidizing bacteria and BioMnO_x may advance our understanding of the potential application of this technology.

References

1. Huber, M.M.; Göbel, A.; Joss, A.; Hermann, N.; Löffler, D.; McArdell, C.S.; Ried, A.; Siegrist, H.; Ternes, T.A.; von Gunten, U. Oxidation of pharmaceuticals during ozonation of municipal wastewater effluents: a pilot study. *Environ. Sci. Technol.* 2005, *39*, 4290-4299.
2. Lin, K.; Liu, W.; Gan, J. Reaction of tetrabromobisphenol A (TBBPA) with manganese dioxide: kinetics, products, and pathways. *Environ. Sci. Technol.* 2009, *43*, 4480-4486.
3. Villalobos, M.; Bargar, J.; Sposito, G. Mechanisms of Pb (II) sorption on a biogenic manganese oxide. *Environ. Sci. Technol.* 2005, *39*, 569-576.
4. Forrez, I.; Carballa, M.; Verbeken, K.; Vanhaecke, L.; , M.S.; Ternes, T.; Boon, N.; Verstraete, W. Diclofenac Oxidation by Biogenic Manganese Oxides. *Environ. Sci. Technol.* 2010, *44*, 3449-3454.

Appendix A

Representative chromatograms of CIP degradation products

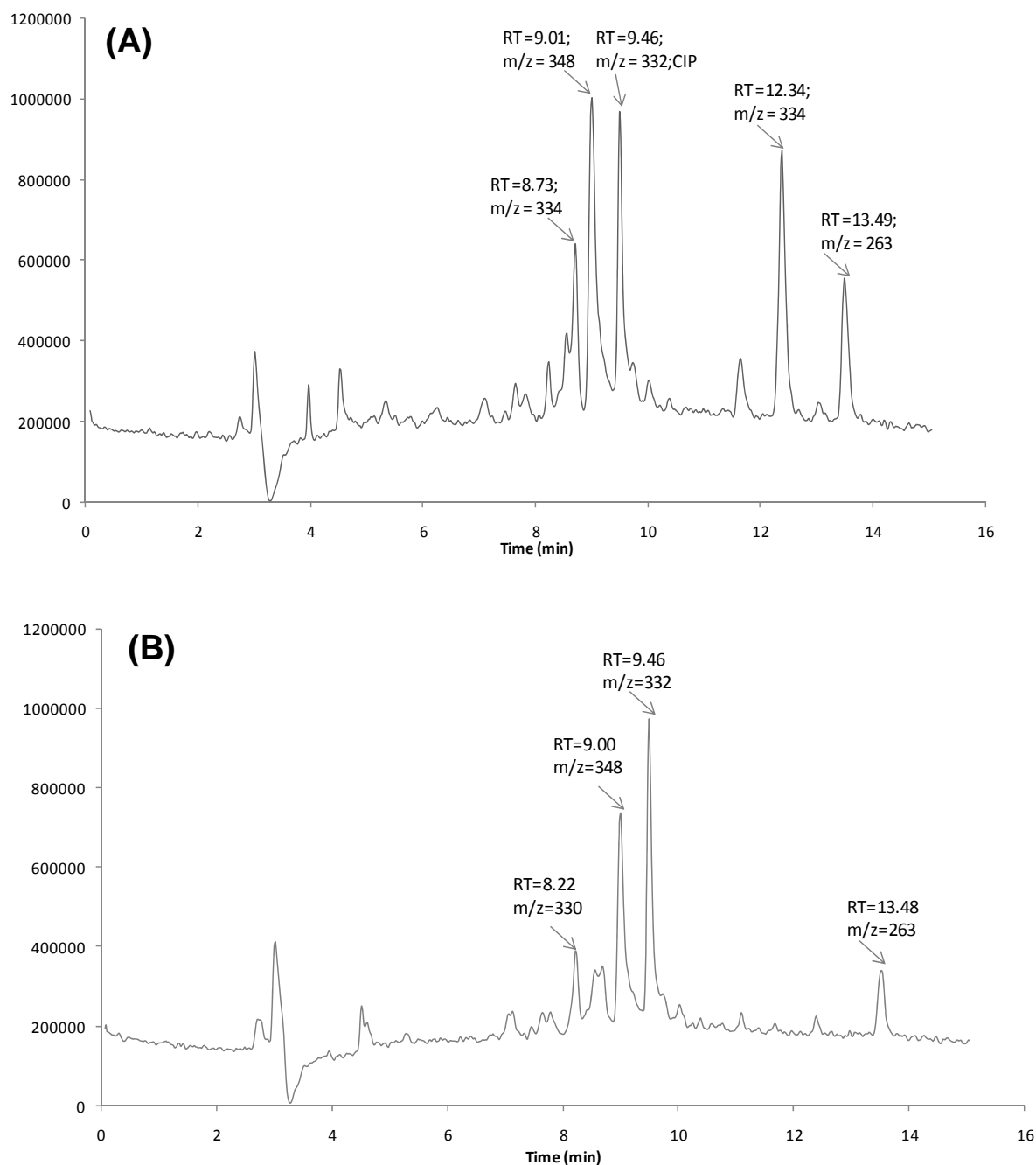


Figure A.1. Total Ion chromatogram of CIP degradation products. Current delivery = 0.04 A; [H₂O₂]:[Fe²⁺] = 10:1; [CIP]₀ = 55 μM; pH₀ = 3.2; t = 2.5 min. **(A)** pH₀ = 3.2 **(B)** pH₀ = 6.2

Appendix B

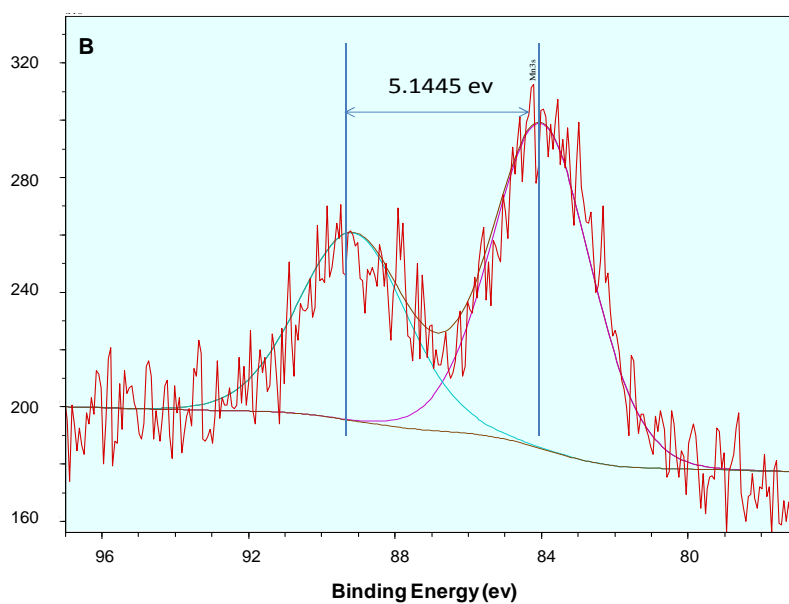
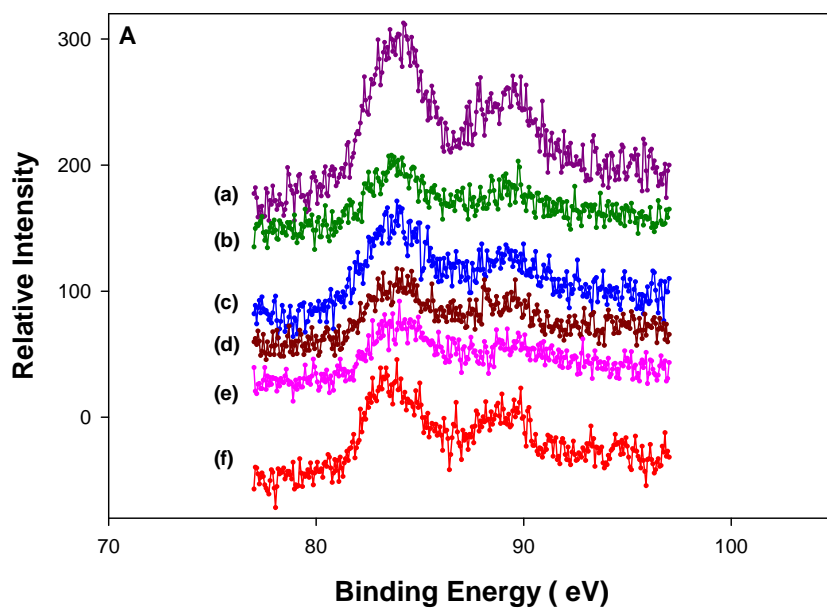


Figure B.1 A. Mn 3s spectra of OMS-2: (a) OMS-2; (b) 3% V/OMS-2; (c) 6% V/OMS-2; (d) 3% Mo/OMS-2; (e) 6% Mo/OMS-2; (f) 9% Mo/OMS-2; **B.** Representative fitting of Mn 3s spectrum (K-OMS-2) by Casa XPS

Appendix C

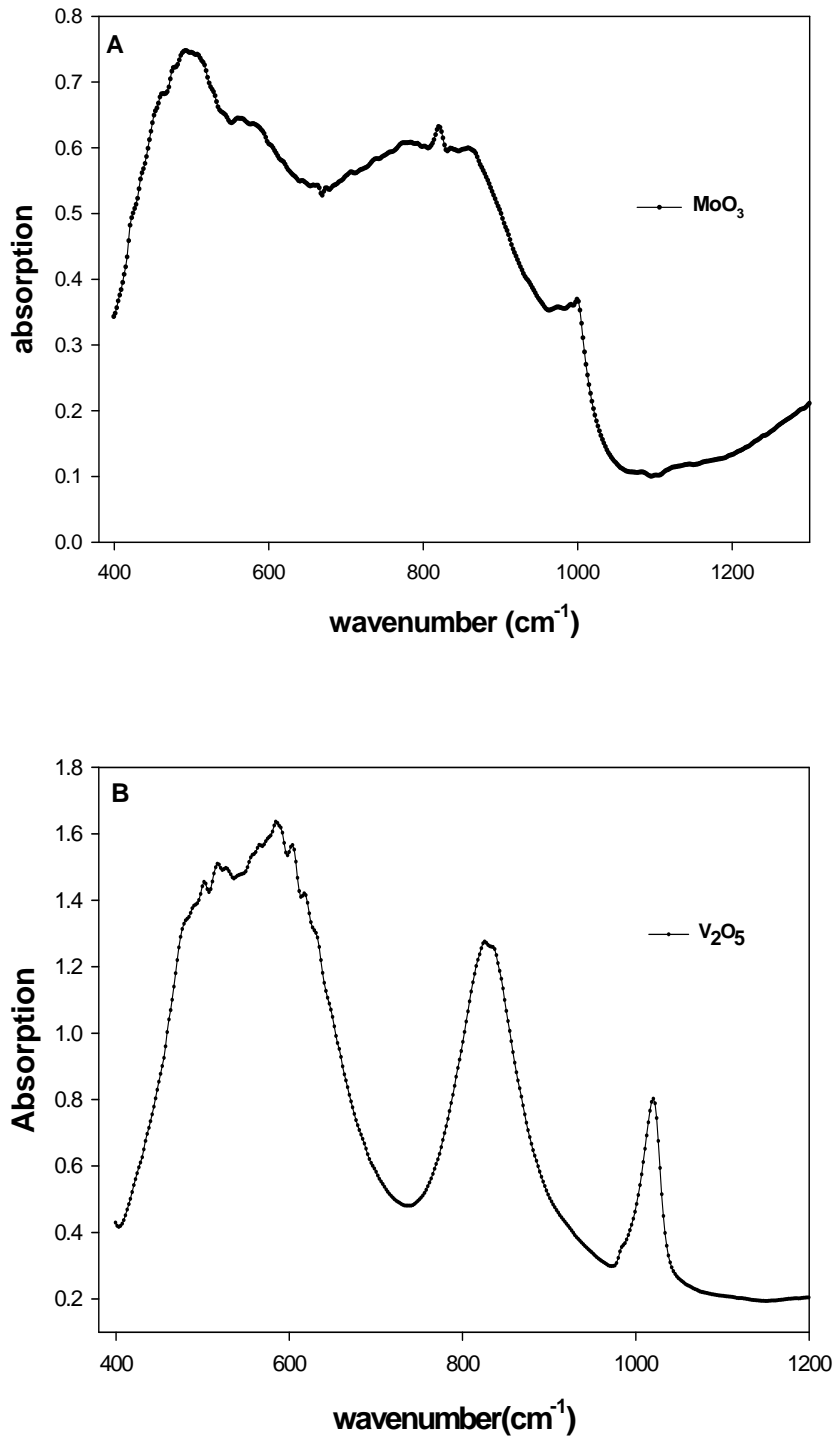


Figure C.1 IR spectra of A. MoO₃ and B. V₂O₅.

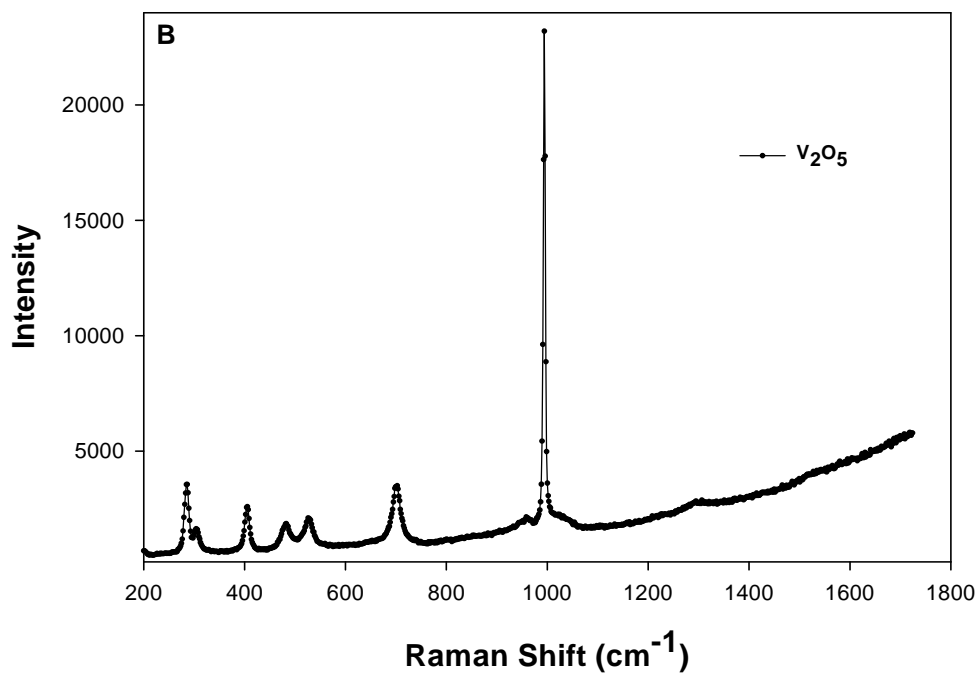
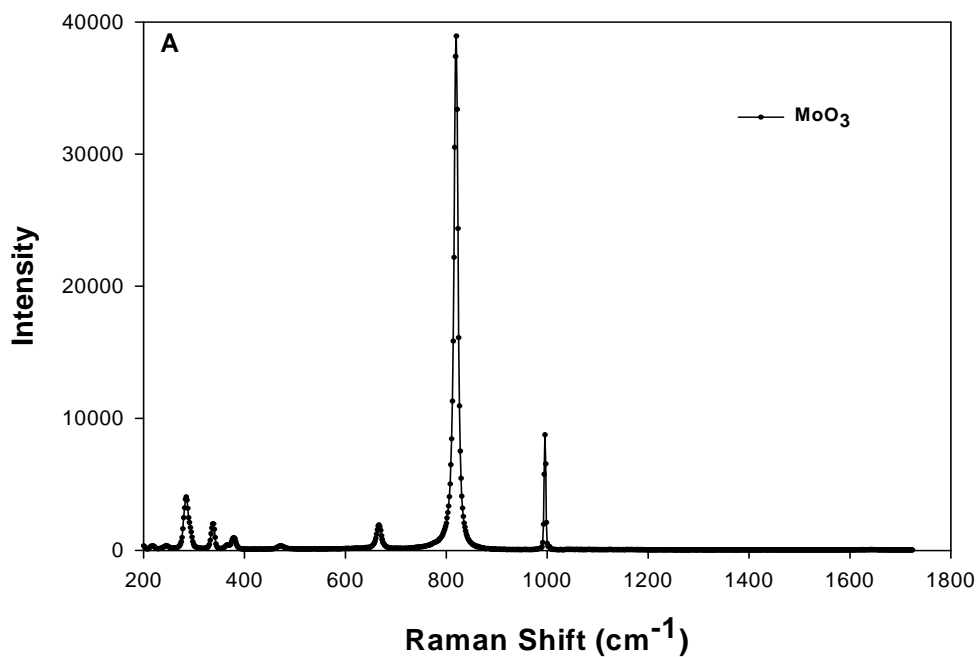


Figure C.2 Raman spectra of **A.** MoO₃ and **B.** V₂O₅.

Appendix D

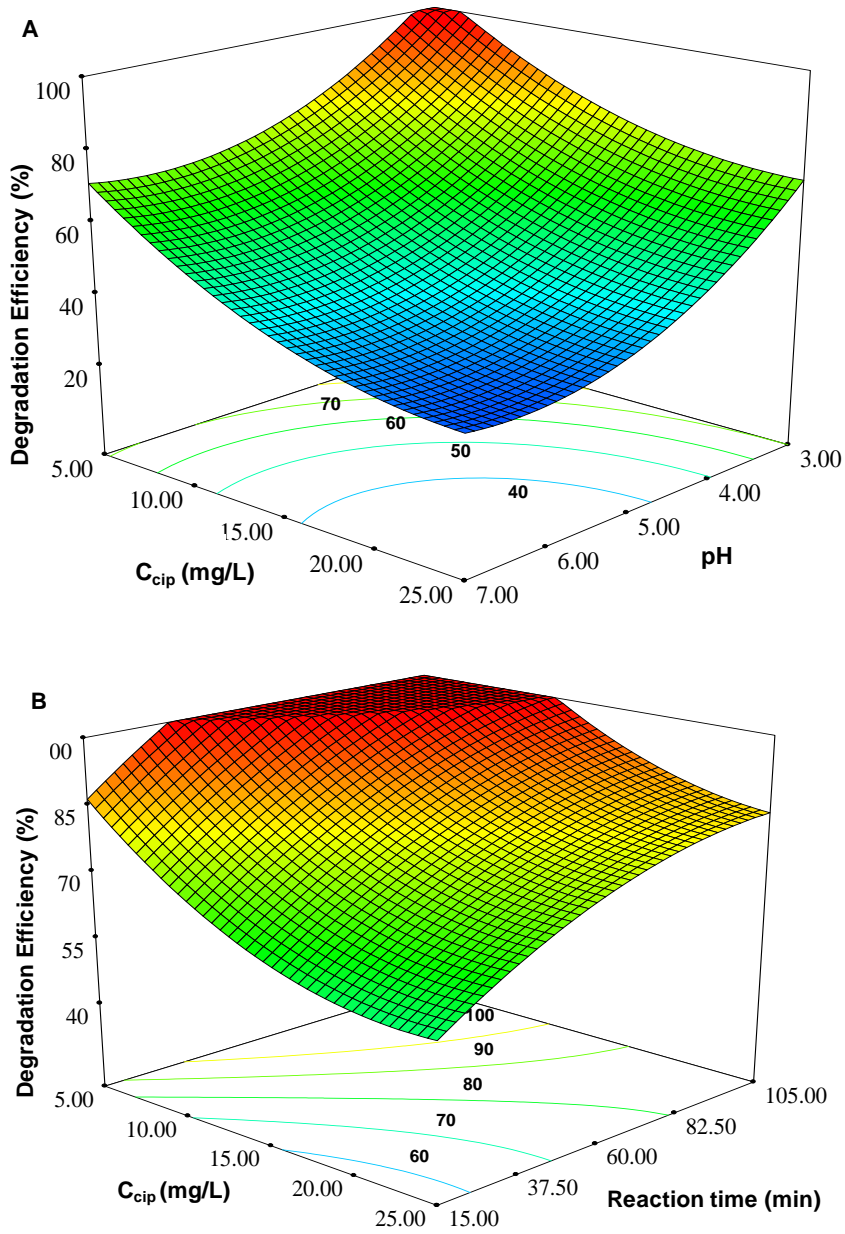


Figure D.1 A. Response surface of degradation efficiency as a function of C_{cip} and pH, reaction time = 45min, [9% Mo/OMS-2] = 150mg/L; **B.** Response surface of degradation efficiency as a function of C_{cip} and reaction time, pH = 3, [9% Mo/OMS-2] = 150mg/L.

Appendix E

Comparison of turbidity and LBB measurement

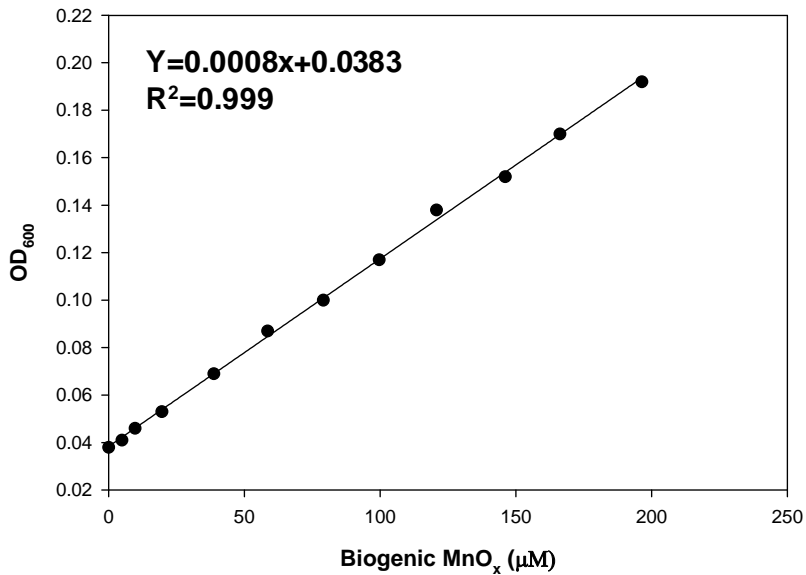


Figure E.1 BioMnO_x standard curve by turbidity measurement (OD₆₀₀)

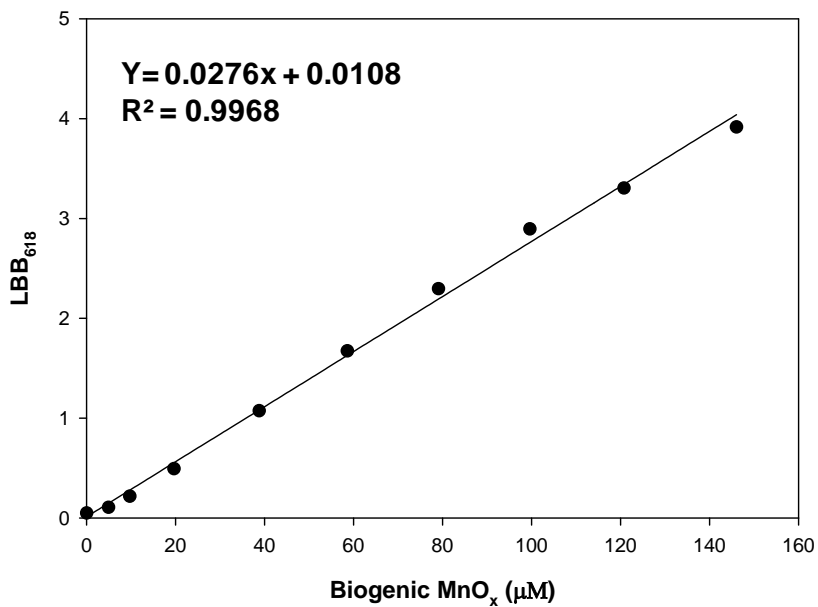


Figure E.2 BioMnO_x standard curve by LBB assay (ABS₆₁₈)

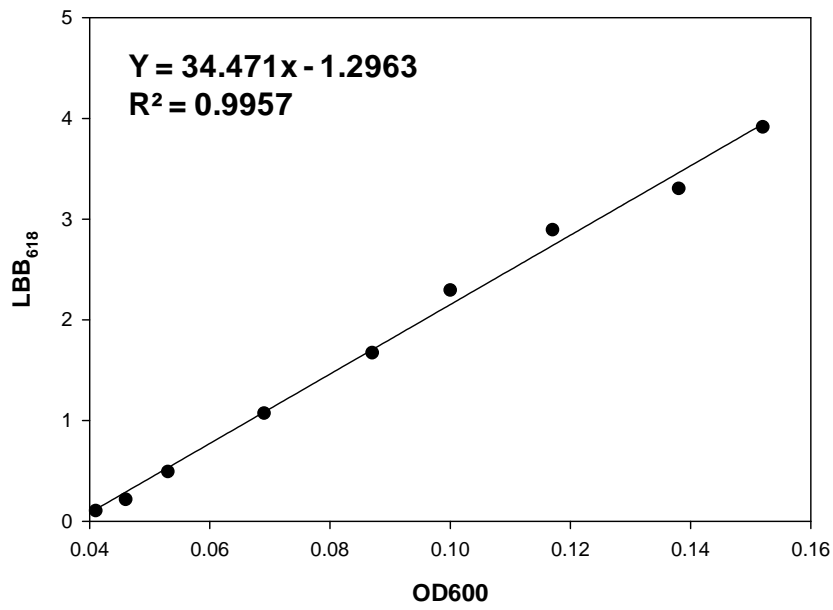


Figure E.3 Correlation of turbidity and LBB assay measurement